

**DISCLAIMER:**

This document does not meet the  
current format guidelines of  
the Graduate School at  
The University of Texas at Austin.

It has been published for  
informational use only.

Copyright  
by  
Vivek Singhal  
2018

**The Dissertation Committee for Vivek Singhal Certifies that this is the  
approved version of the following Dissertation:**

**Design and Development of an X-ray Sensor to Measure the Density  
and Flow Rate of Drilling Fluids in High Pressure Lines**

**Committee:**

Eric van Oort, Supervisor

Dongmei Chen

Alan C. Bovik

David DiCarlo

Ronald E. Barr

**Design and Development of an X-ray Sensor to Measure the Density  
and Flow Rate of Drilling Fluids in High Pressure Lines**

**by  
Vivek Singhal**

**Dissertation**

Presented to the Faculty of the Graduate School of

The University of Texas at Austin

in Partial Fulfillment

of the Requirements

for the Degree of

**Doctor of Philosophy**

**The University of Texas at Austin**

**December 2018**

Dedicated to my parents, for all their sacrifices and support, my most dear brother, and  
my loving wife.

## **Acknowledgements**

My advisor, Dr. Eric van Oort, for providing me with the opportunity to embark on this life changing journey. The freedom, independence and trust provided by him was crucial in shaping my work and overall experience. Dr. Pradeepkumar Ashok, for his support and guidance through many difficult moments. He has been a great mentor and a very important person in shaping my Ph.D. experience. Darry Nygaard at the PGE machine shop for his help in building my experiments and helping me through many critical deadlines. Tesse Smitherman, for her friendship and for making sure that I never had to worry about any paperwork or formalities that would otherwise distract me from my research. Matthew Colbert at the UTCT for spending many hours to help me collect data for my experiments. Dr. Nicolas Espinoza, for providing a conducive environment to conduct my X-ray experiments. A special thanks to Dr. Alan C. Bovik, for always making himself available whenever I was in need of his guidance and experience. Gary and Glenn, the facilities coordinators, for their friendly and helpful nature. I also acknowledge all my past professors and mentors who have selflessly shared with me, their vast knowledge, and the invaluable lessons learned from their own life experiences. Finally, I want to thank Weatherford International for funding my research. Without their financial support none of this would be possible.

## **Abstract**

### **Design and Development of an X-ray Sensor to Measure the Density and Flow Rate of Drilling Fluids in High Pressure Lines**

Vivek Singhal, Ph.D.

The University of Texas at Austin, 2018

Supervisor: Eric van Oort

There is a need for advanced technology that can accurately measure the density and mass flow rate of drilling fluids at the high pressure well inlet in real-time. Current reliance on antiquated metering technologies such as the pressurized mud balance and the pump stroke counter to make these measurements greatly impedes our ability to accurately predict the near well bore pressure profile and measure the delta flow rate, which is one of the primary indicators for trouble events such as kicks or lost circulation. In order to address this gap in technology an X-ray sensor was developed to make real-time measurements at greater than 99% percent accuracy and 1 Hz measurement frequency. The X-ray sensor can measure the density of drilling fluids in the 8 ppg to 20 ppg range and with flow rates of up to 1200 gpm. These measurements are made using 320 kV/1500W polychromatic X-ray source, which is well within the range of readily available industrial X-ray tubes. In the past such measurements would require X-ray voltages that could only be achieved with linear accelerators thereby making the cost and size of equipment non-conducive to the

drilling environment. However, recent advances in pipe manufacturing, particularly using a class of low density and high pressure materials known as carbon fiber reinforced polymers (CRPs) and, are now making it viable to re-visit relatively low cost X-rays systems for density and mass flowrate measurements. Windows constructed from CRPs allow us to bypass the high density carbon steel standpipe and make measurements at voltages that do not require a linear accelerator. In this paper we discuss the design and implementation of a CRP based X-ray sensor that is used to measure drilling mud density and mass flowrate at the high pressure well inlet.

## Table of Contents

List of Tables .....	xii
List of Figures .....	xiii
<b>INTRODUCTION.....</b>	<b>1</b>
Objective.....	3
Proposed Solution .....	4
Dissertation Outline .....	5
<b>1 LITERATURE REVIEW .....</b>	<b>8</b>
1.1 Introduction.....	8
1.2 Volumetric Flow Measurement Meters .....	9
1.2.1 Pump Stroke Counter.....	9
1.2.2 Pump Rotary Speed Counter/Shaft Encoder.....	13
1.2.3 Transit Time Ultrasonic Flowmeter (TTUF).....	14
1.2.4 Pulsed Ultrasound Doppler Meter .....	19
1.2.5 Magnetic Flow Meter.....	21
1.2.6 Flow Paddle Meter.....	24
1.2.7 Rolling Float Meter (RFM).....	25
1.2.8 Pit Volume Totalizer (PVT) .....	26
1.2.9 Trip Tanks.....	28
1.2.10 Differential Pressure Flow Meters.....	29
1.3 Density Measurement Meters .....	31
1.3.1 Mud Balance - Unpressurized.....	31
1.3.2 Mud Balance - Pressurized .....	31

1.3.3	Gamma Ray Densitometer.....	32
1.4	Mass Flow Rate Measurement Meters.....	37
1.4.1	U-Tube Coriolis Meter.....	37
1.5	Tabulated Summary .....	44
1.6	Discussion on Meters Reviewed.....	46
1.6.1	Outlet Mass Flow Rate Measurement.....	47
1.6.2	VFR Measurement while Tripping .....	48
1.6.3	Inlet Density Measurement.....	48
1.6.4	Inlet VFR Measurement of Non-Aerated Drilling Fluids.....	49
1.6.5	Inlet VFR Measurement of Aerated Drilling Fluids.....	50
1.7	Conclusion .....	51
<b>2</b>	<b>DENSITY MEASUREMENT USING X-RAYS .....</b>	<b>52</b>
2.1	Introduction.....	52
2.2	Principles of X-ray Attenuation for Density Measurement .....	54
2.3	Experimental Test Setup.....	57
2.4	X-ray System Calibration .....	59
2.5	Experimental Verification that X-ray Attenuation is Unaffected by Flow-Rate for Incompressible Fluids .....	63
2.6	Density Estimation Methods.....	65
2.6.1	Empirical Method .....	66
2.6.1.1	Fluctuating HGS Concentrations .....	66
2.6.1.2	Fluctuating Contaminant Concentrations .....	69
2.6.2	Model Based Method #1.....	71
2.6.2.1	Fluctuating HGS Concentrations .....	73

2.6.2.2	Fluctuating Contaminants Concentrations .....	75
2.6.2.3	Determining $I_0$ .....	76
2.6.2.4	Determining ' $\mu_m$ ' of the Original Mud, HGS and Contaminants ..	78
2.6.2.5	Calculating ' $\mu_m$ ' of the Original Mud.....	78
2.6.2.6	Calculating ' $\mu_m$ ' of the HGS.....	79
2.6.2.7	Calculating ' $\mu_m$ ' of the Contaminants.....	80
2.6.3	Model Based Method #2.....	82
2.6.4	Accounting for Effects of Temperature, Pressure and Aeration.....	85
2.6.4.1	Effect of Temperature and Pressure on $\mu_m$ .....	85
2.6.4.2	Accounting for Temperature and Pressure Variations.....	86
2.6.4.3	Accounting for Mud Aeration.....	87

2.7 Conclusion .....	88
<b>3 VFR MEASUREMENT USING X-RAYS.....</b>	<b>89</b>
3.1 Introduction.....	89
3.2 Measuring VFR using High Speed X-ray Imaging Equipment and Tracer Particles ..	90
3.3 Measuring VFR using a Flat Panel Detector and Tracer Particles .....	97
3.4 Measuring Volumetric Flow Rate using the Piston Mechanism .....	99
3.5 Conclusion .....	103
<b>4 SENSOR DESIGN.....</b>	<b>105</b>
4.1 Introduction.....	105
4.2 Sensor Mechanical Design.....	107
4.3 X-ray Source Power Requirements.....	115
4.4 X-ray Equipment Selection.....	119
4.4.1 X-ray Tube.....	119
4.4.2 X-ray Generator, Controller & Cooler.....	122
4.4.3 Integrated Blocks .....	123
4.5 Conclusion .....	124
<b>5 CONCLUSIONS.....</b>	<b>126</b>
5.1 Contributions.....	127
5.2 Recommendations and Future Work .....	130
<b>GLOSSARY .....</b>	<b>131</b>
<b>BIBLIOGRAPHY .....</b>	<b>133</b>

## List of Tables

Table 1- Tabulated summary of reviewed meters.....	45
Table 2- Density meters not reviewed in this paper. ....	45
Table 3- Volumetric flow meters not reviewed in this paper. ....	46
Table 4: Drilling mud density and composition used for experimental evaluation of the density estimation methods.....	69
Table 5- Density estimation errors using Method #2.....	85
Table 6: Summary of sensor component dimensions and materials of construction.....	114
Table 7- Intermittent duty medical grade vs continuous duty industrial grade X-ray tubes. ....	120

## List of Figures

Figure 1- Clamp on transit time ultrasonic flowmeter conceptual schematic. ....	15
Figure 2- (a) Transducers in V-mode. (b) Waveform conversion diagram. ....	16
Figure 3- Schematic of a Pulsed Ultrasound Doppler Meter. ....	20
Figure 4- Detailed schematic of a single beam gamma ray densitometer. ....	33
Figure 5- (a) U tube Coriolis meter (b) Internal components (c) Coriolis meter working principle at no flow (d) Coriolis meter working principle at flow .....	38
Figure 6: X-ray densitometer location on the rig. ....	55
Figure 7- Experimental setup. ....	58
Figure 8- Sample radiograph. ....	59
Figure 9- Variation in GL with time. ....	60
Figure 10- Implementing two-point calibration. ....	61
Figure 11- Errors after two-point calibration for muds of density in the 9–10 ppg range. ....	62
Figure 12- Schematic of flow loop that was used for testing X-ray attenuation dependence on flow rate. ....	64
Figure 13- Descriptive statistical values for the sampling distribution. ....	64
Figure 14- Effect of HGS on mud density and GLV. ....	67
Figure 15- Error distribution for low density muds. ....	67
Figure 16- Error distribution for medium density muds. ....	68
Figure 17- Error distribution at 2 ppg interpolation intervals. ....	68
Figure 18- Effect of contaminants on mud density and GLV. ....	70
Figure 19- Error distribution for mud with contaminants. ....	71

Figure 20- Error distribution for low density muds.....	74
Figure 21- Error distribution for medium density muds.....	74
Figure 22: Error distribution for mud with contaminants.....	75
Figure 23- $I_0$ values calculated using Equation 11 for water samples. ....	77
Figure 24- $\mu_m$ distribution at different $I_{0\_true}$ values.....	78
Figure 25- $\mu^*$ vs $t-t^*$ curve for acrylic and aluminum combination.....	84
Figure 26- $\mu^*$ vs $t-t^*$ curve for aluminum and titanium combination.....	84
Figure 27- $\mu^*$ vs $t-t^*$ curve for acrylic and titanium combination.....	84
Figure 28- Schematic representation of the block matching technique (Note: Figure is used for explanation purposes only and is not to scale).....	91
Figure 29- Image of fluid-flow used for preliminary testing.....	92
Figure 30- Example of calculated motion vectors for an image section (Note: not for the same image as used in Figure 29). ....	93
Figure 31- Convolution of an image with a LoG filter.....	94
Figure 32- Surface plot of an image convolved with a LoG filter (Note: not for the same image as used in Figure 31). ....	94
Figure 33- Artifacts detected by the LoG filter. ....	95
Figure 39: Schematic of piston mechanism.....	100
Figure 41- (a) API rated steel casing. (b) Source, detector and polymer pipe assembled onto casing.....	107
Figure 42- (a) Endcap design. (b) Complete sensor assembly.....	108
Figure 43: (a) X-ray calibration mechanism isometric view (b) X-ray calibration mechanism cross-sectional view.....	109
Figure 44: Flow rate mechanism isometric view.....	110
Figure 45- Sensor cross-sectional view from detector side (front view).....	111

Figure 46- Side cross-sectional view. ....	112
Figure 47- Measurement classification of radiographed region (front view). ....	113
Figure 48- Measurement classification of radiographed region (side view). ....	113
Figure 49: Prototype sensor. ....	115
Figure 50- X-ray power required to penetrate a 22 ppg drilling mud in a 5-inch plastic pipe.....	117
Figure 51- X-ray power required to penetrate a 11.5 ppg drilling mud in a 8-inch plastic pipe. ....	117

## INTRODUCTION

As the oil and gas landscape has become more cost conscious in recent years, operators, service providers and rig contractors are actively looking for ways to reduce drilling and completions costs through process optimization. Furthermore, after the Macondo well blowout in 2010, an even greater emphasis is now placed on improving safety. Significant improvements in early kick detection and managed pressure drilling (MPD) technologies, over the last five years in particular, are enabling operators to realize their cost and safety. A crucial component of these technologies is the ability to accurately determine density and mass flow rate in and out of the well. Mud density characterization is important during well construction operations, primarily because the mud hydrostatic pressure, which is a function of mud density, serves as the primary barrier to restrict the influx of formation fluids and gas. Measuring mud density therefore enables better control of the drilling fluid (mud) pressure profile in the annulus. Moreover, in MPD, where the objective is to maintain a constant bottom hole pressure (known as the constant bottom-hole pressure method - CBHP), it is critical to monitor the delta flow rate, i.e. the difference between mass flow out and mass flow into the well. This is one of the primary indicators for trouble events such as kicks or lost circulation occurrences. The parameters that determine mass flow rate are volumetric flow rate (VFR) and density. Note that both the density and VFR are subject to constant change during well construction operations.

The density and mass flow rate measurements can be made on the low pressure side before the mud pump suction or on the high pressure after the mud pump discharge. Sensor

redundancy can be avoided if the measurements can be made at the high pressure standpipe, as some rigs have multiple mud pumps whose flow is routed through the common rig standpipe. Furthermore, density measurements are generally preferred on the high pressure side, since the density of the mud (which can be heavily aerated) under pressure is more representative of the downhole mud density than density measured at atmospheric pressures.

In spite of the need for real time mud density measurement at the high pressure inlet of the well, advancement in technology has been slow. Currently no good sensors exist to measure these parameters in real-time at the high pressure inlet of an oil or gas well under construction. The most commonly used sensor for measuring density is the API pressurized mud balance. Even though it is quite accurate, it uses manual labor to make measurements and fails to account for the variability in the mud composition across the mud pits (Nickles, 1972). Furthermore, when using the mud balance, the density measurements are typically made only infrequently, leading to mud density uncertainty in the intervals between measurements. Another meter that is sometimes used for density measurements on the high pressure standpipe is the gamma ray densitometer. It has high accuracy and can measure density in real-time. Typical flow conditions encountered at the inlet, such as a fully filled pipe and a homogeneously mixed mud, are very conducive to its use. However, in spite of the various advantages offered by this meter, it has seen limited adoption in field. This is because the meter has a radioactive source, which raises safety concerns. Additionally, the meter creates undesirable logistical burdens on operators due to special procedural requirements in handling, transportation, storage and disposal of this source (Tjugum et al.,

2002). To measure VFR in the high pressure standpipe, rig operators most often rely on the pump stroke counter, which uses the number of pump strokes to estimate the flow. When used with a new pump the sensor exhibits reasonable accuracy. However, with wearing of pump components its accuracy deteriorates significantly over time (Bryant, 2016). Another drawback to the meter is that it does not account for mud compressibility. Thus, any aeration present in the mud lines or the mud itself can lead to a considerable inaccuracy in recorded mud volume when the mud is pumped under pressure into a well (Caldwell et al., 2010).

An improvement in measurement accuracy and measurement frequency of density and mass flow rate on the high pressure inlet would allow for early kick detection and better management of the annular pressure profile, which will improve safety and reduce the non-productive time encountered during well construction operations. A sensor that can meet these requirements would enable a major improvement in the safe drilling of complex wells with narrow drilling windows.

## **Objective**

The objective of this research was to develop a real-time density and mass flow rate measurement sensor for drilling and completions fluids, that was compatible with the high pressures at the well inlet. The following design parameters needed to be satisfied in developing the sensor:

- Measure fluid density and mass flow rate in pipes with 4-inch internal diameter.
- Provide a measurement accuracy of greater than 99%.

- Make measurements at a measurement frequency of 1 Hz.
- Measure drilling fluid densities between 8 lb/gal and 20 lb/gal. This density range is typical for most drilling and completions fluids.
- Measure flow rates between 0 gpm and 1200 gpm, which are representative of flow rates encountered in intermediate and smaller hole sections. These flow rates equate to pipe velocities of 0 ft/s and 30 ft/s respectively.
- Work with pumping pressures up to 7500 psi.
- Work with drilling fluid viscosities between 1 cp and 100 cp.
- Works with all types of drilling fluids, i.e. water/oil/synthetic based.

### **Proposed Solution**

This solution presented in this dissertation uses polychromatic X-rays to make density and mass flow rate measurements. X-ray technology works on the same proven principles as gamma ray densitometry, and can provide similar levels of accuracy. The major difference between X-rays and gamma rays is that X-rays do not require a radioactive source and are produced by firing electrons at a metal target. Therefore, X-ray sources do not yield the safety and logistic concerns that are typically associated with gamma ray sources. Furthermore, it is expected that end users would be more receptive to a sensor technology which is a safer derivative of existing and field established science.

Sensor design using X-rays are now possible due to recent advances in low density ( $\sim 1.3 \text{ g/cm}^3$ ) and high pressure ( $>20 \text{ ksi}$ ) carbon reinforced polymers (CRPs). These CRPs offer a lower thickness-to-pressure ratio than the high density steel ( $\sim 8 \text{ g/cm}^3$ ) currently

used in standpipe construction. A sensor constructed from CRP material would allow for significantly greater X-ray transmission than steel, and thereby greatly reduce the voltage and power demand on the X-ray source. These lower voltage and power demands drastically reduce the cost, size, weight and complexity of the X-ray source, making it practical and safe for use in well construction applications.

Density measurements are made by monitoring the amount of X-ray transmission through different drilling fluids. To measure flow-rate two techniques were explored. The first technique estimates flow rate by monitoring changes in X-ray transmission across a spring loaded piston which deflects upon fluid flow. The second technique estimates flow rate by measuring the speed of tracer particles, that are intentionally introduced into the drilling mud, from X-ray radiographs.

This work provides a completely new method for accurate (>99%), high frequency (1 Hz), and real-time density and mass flow rate measurements of drilling and completions fluids at the high pressure inlet (7500 psi). Preliminary findings indicate that no existing sensors used for similar applications can match the measurement accuracy and frequency that may be offered by this technology. It is expected that the development of this sensor or similar ones like it using X-ray technology will improve the safe drilling of complex wells with narrow drilling windows.

## **Dissertation Outline**

In Chapter 2 a comparative evaluation of mud density and flow rate measurement technologies is provided. Flow meters are discussed first, followed by density meters and

finally by the Coriolis meter which can measure both flow and density. The review of each meter is, where possible, divided into three sections: overview and principle of operation, limitations and sources of error, and ongoing research to overcome the limitations. The gaps and shortcomings identified for the various metering techniques and instruments have been used to help guide R&D into development of the X-ray sensor.

In Chapter 3, the procedure used to make density measurements using X-rays is described along with the test setup used to conduct the density experiments. An implementation of a calibration system, necessary to make repeatable density and flow rate measurements by accounting for time variability in the output of the X-ray system, is discussed. Since all density experiments were conducted under static conditions, it is also shown that density measurements for incompressible fluids are unaffected by flow-rate. Finally, the experimental results from three density estimation methods, an empirical method, and two different model-based methods, are presented and discussed.

In Chapter 4, three different methods to measure VFR are discussed. The first method uses high speed X-ray imaging equipment to capture motion of artificially induced tracer particles. An image processing algorithm is then used to extract the motion information and calculate the VFR. The second method uses standard X-ray equipment to capture the path of tracer particles on a single radiograph. A procedure that could be used to measure VFR from the radiograph is then described. In the third method VFR is calculated by using X-rays to measure the change in displacement of spring loaded pistons, which deflect due to the force exerted by the moving fluid. The piston deflection which is directly proportional to the fluid mass flow rate is then used to infer fluid velocity.

In Chapter 5, the mechanical design of the sensor is presented along with details and guidelines on sizing and sourcing of the sensor components.

# 1 LITERATURE REVIEW

## 1.1 Introduction

The choice of metering technology is of vital importance to meeting expectations. Conventional and emerging drilling and completion applications demand high frequency and high accuracy density and flow rate data. Meeting both these requirements is a challenge for most measurement technologies currently available in the marketplace. Even though, gradual advancements using improved designs and machine learning algorithms are now being made to address both of these challenges, they are not adequate to meet the needs of current drilling operations which are reaching greater levels of automation and a reduced reliance on the driller for making decisions. A step-change in meeting sensor performance and reliability expectations can only be accomplished with a completely new and disruptive technology, such as X-rays, to make the density and mass flow rate measurements.

A literature review shows that there is an abundance of metering choices available for oil and gas drilling operations, with each meter offering unique benefits and limitations. Meter choices are influenced by risk tolerance, specific application type and available capital budget. At the inlet, the biggest challenge faced by measurement technologies is the high pressure requirement, whereas fluid aeration causes the most problems at the outlet. The meters and sensors reviewed here are some of the most frequently used in the drilling industry today. They can be categorized broadly into two classes: those designed to monitor flow and density at the well inlet, and those designed to monitor flow and density at the

well outlet. There are several technologies which can measure both flow and density at the well outlet where pressure remains relatively low. However, there is no single meter for the inlet that can make both measurements, primarily due to the high pressures and the associated (and warranted) reluctance to break the integrity of the standpipe.

In the following sections, flow meters are discussed first, followed by density meters and finally by the Coriolis meter which can measure both flow and density. The review of each meter is, where possible, divided into three sections: overview and principle of operation, limitations and sources of error, and ongoing research to overcome the limitations. A tabulated summary of some of the important meter features and a discussion on the current state of drilling fluid density and flow rate measurement technology is provided at the end of the review.

## **1.2 Volumetric Flow Measurement Meters**

### **1.2.1 PUMP STROKE COUNTER**

#### **Overview and Principle of Operation**

Mud circulation is accomplished using reciprocating plunger pumps. Such pumps maintain a constant output flow by adjusting the discharge pressure, which can reach up to 51.71 MPa (7.5 ksi). Single-acting pumps discharge fluid only during their forward stroke, whereas double acting pumps discharge fluid during both the forward and the return stroke. Triplex (3 pistons) single acting pumps are preferred over duplex (two pistons) double acting pumps because they are lighter, have a smoother discharge and lower maintenance costs. The VFR (Q) in gallons per minute (gpm) of a single acting triplex pump is:

$$Q = \left( \frac{3AL * rpm}{231} \right) * VE \quad 1$$

$$VE = (1 - (P\beta r) - S) \quad 2$$

where:

A = Piston cross sectional area (m<sup>2</sup> or in<sup>2</sup>)

L = Stroke length (m or in)

rpm = Pump motor speed in revolutions per minute (rpm)

VE = Volumetric efficiency

P = Differential pressure between pump suction and discharge (Pa or psi)

β = Liquid's compressibility factor at pumping temperature. It is inverse of fluid bulk modulus (m<sup>2</sup>/kg or in<sup>2</sup>/lb)

r = Unit less ratio of the total volume between the suction and discharge valves inside the pumping chamber when the piston is at full forward stroke, divided by the piston displacement volume (A \* L). This is also known as C/D ratio (pumping chamber clearance (C) to displacement ratio (D)).

S = Slip accounts for the leakage of fluid back through the discharge or suction valve as it is closing (or seated). It is a unit less quantity. Slip is also affected by the fluid viscosity. It will vary between 1 to 5 percent based upon pump speed and valve design. In general, most pump designs will typically have a 3 percent volumetric loss.

VE critically affects a reciprocating pump's capacity. It is expressed as a percentage and is proportional to the ratio of the total discharge volume to the plunger displacement.

The VE for a new pump can be determined within a one percent accuracy. It is independent of pump speed (Tackett et al., 2008) and is affected by progressive wear in pump components over its lifespan. Pump wear can largely be attributed to the abrasive nature of drilling fluid and the high pressure of the pumping operation (Zoellner et al., 2011).

A pump stroke counter is a limit switch which gets triggered with each piston stroke (Schafer et al., 1992). It is the most commonly used meter in the drilling industry to characterize the VFR at the inlet. The VFR using the stroke counter is determined as follows:

$$Q = \text{Strokes per Minute} * \text{Volume per Stroke} * VE \quad 3$$

### **Limitations and Sources of Error**

The primary shortcoming of the pump stroke counter is that it fails to account for the uncertainty in VE, which can lead to errors from single digit to double digit percentages over the pump's lifetime. The error in most cases is partially compensated for by making an estimate of VE, which can be anywhere between 85-98% (Bryant, 2016). The meter also fails to account for variation in pump field performance and factory performance. Factory performance tests prior to pump delivery are conducted at Standard Temperature and Pressure (STP) conditions with water (Newtonian rheology) as the pumping fluid. Fluids used in the field typically exhibit non-Newtonian rheological behavior and are used under non-standard conditions. Pump performance measured at the factory and in the field may therefore differ significantly. Furthermore, the meter does not account for mud compressibility. Thus, any aeration present in the mud lines or the mud itself can lead to a

considerable loss in recorded mud volume when the mud is pumped into the well under pressure (Caldwell et al., 2010). The counter does not track piston position and is therefore characterized by a slow response time (especially problematic at low flow rates) since flow is typically only determined at the end of each stroke. This is typically illustrated by the pump pressure starting to increase even before any pump-rate is reported (Daireaux et al., 2013, Cayeux et al., 2013). Finally, stroke counters cannot be used to predict rate of change of pump rate, due to the long time needed to notice pump acceleration or deceleration (Cayeux et al., 2013).

### **Overcoming Limitations**

The slow response time of the pump stroke counter can be improved by using two sensors per piston, one at each end, in order to count half strokes. Note that for low pump speeds and low sampling rates even this may not be sufficient in many instances (Cayeux et al., 2013). Using a pump rotary speed transducer (discussed in next section) instead of the pump stroke counter is another option to obtain higher frequency measurements where circumstances permit. Alternatively, where applicable, frequency output from a scalar variable frequency drive (VFD), can be used to calculate a reasonable good high frequency estimate of actual motor speed (Cayeux et al., 2013). VE estimations can be improved by using theoretical models of pump efficiency deterioration. These models can be difficult to develop and implement in real time and cannot fully correct for errors, thereby still leaving discrepancies in the actual VE estimate and in turn the overall flow calculation. Finally, calculations can be made to adjust factory performance data for field settings, i.e.

modifying factory performance test data for mud instead of water, and accounting for temperature and pressure differences in the field.

## **1.2.2 PUMP ROTARY SPEED COUNTER/SHAFT ENCODER**

### **Overview and Principle of Operation**

A shaft encoder is used as a substitute for the pump stroke counter when VFR from the mud pumps is required at a higher frequency (Hossain et al., 2015). A shaft encoder is also a good choice when the driving motor is DC and frequency output from a VFD cannot be used to estimate pump motor shaft speed (Cayeux et al., 2013). The VFR is calculated using the shaft speed information provided by the shaft encoder. The shaft encoder provides a pulse output, specified as pulses per revolution, with a frequency several times the pump stroke counter frequency. The number of pulses per turn also defines the resolution of the device (Schafer et al., 1992). Thus, the shaft encoder not only provides data at a higher frequency than the stroke counter but is also capable of detecting changes in pump speed much faster (Schafer et al., 1992). The encoder is an electro-mechanical device that converts the angular position or motion of the shaft to an analog signal or digital code. It can be of absolute or incremental type. An absolute encoder assigns a fixed origin on the shaft and provides a position value relative to that origin. Even when the encoder is switched off it remembers the origin, thereby providing the instantaneous position of the shaft. An incremental encoder on the other hand assigns a new origin to the shaft each time it is switched on and provides information on relative movement. Furthermore, a rotary encoder is typically of optical or magnetic type. Compared to an optical encoder, the

magnetic encoder is rugged and well suited for environments with high temperature, vibration and shock. An incremental magnetic rotary encoder is best suited for mud pumps because it is available for various shaft configurations such as solid shaft, blind shaft, integrated coupling and through shaft.

### **Limitations and Sources of Error**

Like the stroke counter, the accuracy of VFR measurements made using the shaft encoder is also limited by the pump VE estimate. Even though it is considered to be the most practical flow meter for inflow measurements on the rig, its use can sometimes be limited by space constraints. In case of the magnetic encoder, performance is negatively affected by ingress of magnetic dust or strong electromagnetic fields, if present.

### **1.2.3 TRANSIT TIME ULTRASONIC FLOWMETER (TTUF)**

#### **Overview and Principle of Operation**

Amongst the various types of non-invasive ultrasonic meters that are available to measure flow rate, the transit time ultrasonic flowmeter (TTUF) is the preferred meter in the drilling industry (Sanderson et al., 2002) given its wide range of applications and high accuracies. It is used in waste water, chemical and paper industries, and for measurement of flow rate of fly ash slurries in power stations and multi-phase slurries in mining applications (Eren, 1998). It has an average lifetime of about six years and is available as a spool-piece meter or as a non-invasive clamp-on meter. Even though the spool-piece meter has a higher accuracy in comparison to the transit-time clamp-on, it is not as widely used because it is more invasive.

The clamp-on meter is particularly suited for applications that require continuity in production. It has experienced widespread adoption in industries such as nuclear energy and oil & gas production (Luca et al., 2016) as a result. It has also seen major interest in recent years due to the noninvasive nature and lower installation costs. The measurement is performed using two piezoelectric transducers, both of which act as an ultrasound transmitter and a receiver. The flow velocity is proportional to the difference between the propagation time of ultrasound in upstream and downstream direction of flow. The volumetric flowrate is determined by multiplying the calculated velocity by the pipe cross-sectional area. The travel time can be measured accurately to a resolution of about 50 picoseconds (Hauptmann et al., 2002). The meter's conceptual schematic is shown in Figure 1.

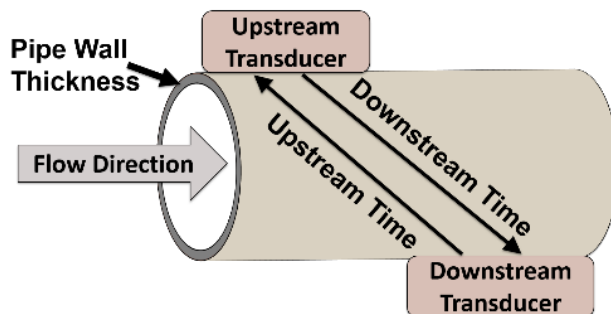


Figure 1- Clamp on transit time ultrasonic flowmeter conceptual schematic.

With regards to accuracy, the following applies:

- For fluid velocities greater than 1 m/s (3.28 ft/sec), these meters have typical errors of less than 5%, repeatability and reproducibility (under unclamping and re-clamping conditions) of greater than 99% and 98% respectively. The meter

accuracy deteriorates towards the lower end of its specified flow range (Sanderson et al., 2002).

- Experimental results carried out under controlled conditions on a 304.8 mm (12 inch) meter showed that the meter almost always over predicted the flow rates for Reynolds numbers between 10,000 and 1,000,000. For velocities and Reynolds numbers greater than 0.43 m/s (1.42 ft./s) and 100,000 respectively, an accuracy of 98.73% was achieved (Prettyman et al., 2014).

The ultrasonic transducer is the most important component of this meter. The transducer must be selected carefully as its characteristics affect the stability and capability of the entire detecting system. It is recommended that both transducers be on the same side of the pipe (V-mode configuration) which also simplifies the calculation of the optimal separation distance between the transducers (Han et al., 2014). One methodology to calculate optimal transducer distance in V-mode is proposed by Mahadeva et al., (2009). Transducers in the V-mode configuration are shown in Figure 2a.

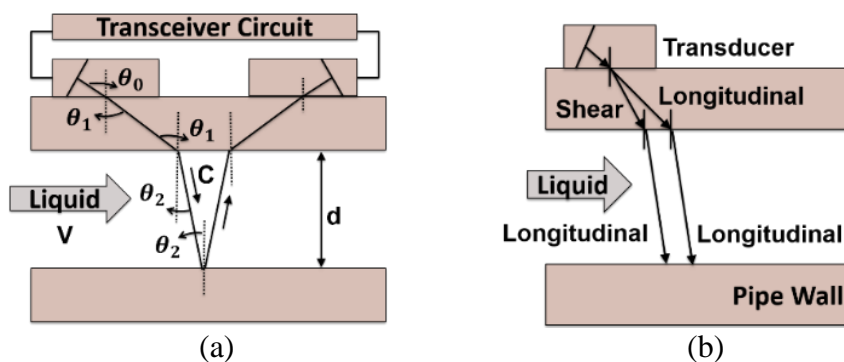


Figure 2- (a) Transducers in V-mode. (b) Waveform conversion diagram.

where 'd' is the propagation distance and ' $\theta_0$ ' is the angle of incidence. One of the factors affecting transducer selection is the angle of incidence ' $\theta_0$ ' (Han et al., 2014). As shown in Figure 2b, the incident beam (angle ' $\theta_0$ ') is split into a shear (angle ' $\theta_1$ ') and longitudinal wave at the pipe surface. These shear and longitudinal waves continue to propagate as two separate longitudinal waves at the pipe liquid interface. To accurately measure fluid velocity, it is desirable that only one longitudinal wave be transmitted through the pipe wall and to the receiving transducer. This can be achieved by adjusting ' $\theta_0$ '. The critical values that limit ' $\theta_0$ ' can be calculated using Snell's law (Han et al., 2014). Other factors affecting transducer selection are fluid temperature, viscosity, and the required ultrasound frequency (a function of 'd', Han et al., 2014).

### **Limitations and Sources of Error**

A variety of parameters affect meter performance. These include: pipe size, material and wall thickness, pipe lining material type and thickness, meter location and mounting, surrounding mechanical and electrical noise, other operational conditions, and fluid density (Sanderson et al., 2002, Eren, 1998). Additionally, various coefficients if not properly accounted for can result in errors. They include: electromechanical coupling coefficients, transmission coefficients, reception coefficients, various mechanical coefficients, acoustic impedances and dielectric constants (Eren, 1998). Errors can also be generated by local variations in temperature, pressure and density.

The meter is not well suited for conditions with solid diameters greater than 1/8th of ultrasound wavelength, high solids content, or presence of air bubbles. Air bubbles affect the speed of sound in the liquid and scatter the ultrasound signal, leading to attenuation and

degradation of the signal to noise ratio (SNR). Air entrainment over 10% can cause much degradation in measurement accuracy (Sanderson et al., 2002). Particles larger than one wavelength of the ultrasound cause scattering errors, known as the scattering effect. A clustering of particles much smaller than one wavelength may also cause scattering errors, due to local changes in fluid viscosity, known as the viscous effect. Large Reynolds number values and drag created by the particles result in errors due to the inertial effect. The weakening of the ultrasonic wave front and the breakup of the ultrasonic signals due to these three effects are major sources of error (Eren, 1998). The resonant and thermal characteristics of some particles can also lead to significant attenuation.

To minimize errors that result from changes in fluid viscosity, meter re-calibration is recommended. An increase in viscosity results in increase in ultrasound attenuation (Chen et al., 2013). Water, for example, has a kinematic viscosity of  $1.003 \times 10^{-6} \text{ m}^2/\text{s}$  ( $10.76 \times 10^{-6} \text{ ft}^2/\text{s}$ ) at  $20^\circ\text{C}$  ( $68^\circ\text{F}$ ) and an ultrasound attenuation of 0.22 dB/m (0.067 dB/ft) at 1 MHz. Castor oil in comparison has a kinematic viscosity of  $1.1 \times 10^{-2} \text{ m}^2/\text{s}$  ( $11.84 \text{ ft}^2/\text{s}$ ) at  $20^\circ\text{C}$  ( $68^\circ\text{F}$ ) and an attenuation of 95 dB/m (28.96 dB/ft) at 1MHz. Since attenuation is proportional to the square of the ultrasound frequency, it is recommended that a lower frequency be used for Castor oil (Sanderson et al., 2002). Also, the current transmitter and receivers use pulsed excitation. Pulsed signals have a fundamental wave mode that is composed of various wave modes, each with their distinct phase velocity. It is very easy for this fundamental wave mode to get distorted when transmitted through a viscous fluid. The distortion makes it difficult for the fundamental wave mode to be detected by the receiver. Also, in pulse mode the resonance frequencies of the transmitter and receiver are

not identical, and vary with temperature independently, resulting in significant measurement errors (Chen et al., 2013).

### **Overcoming Limitations**

Chen et al., (2013) proposed continuous excitation of the transducers instead of the pulsed excitation. The transmitter and receiver under continuous excitation are forced into excitation by the same signal, and are therefore guaranteed to be at a constant known frequency. Moreover, using continuous excitation, excitation energy can be increased by extending the excitation duration without increasing the instantaneous power (which is the case with pulsed excitation), leading to an improvement in the SNR of the receiving waveform. Santhosh et al., (2012) showed that by using an artificial neural network (ANN) in series with an ‘ultrasound frequency to voltage converter’, calibrations are no longer necessary with changes in pipe diameter, liquid density, and liquid temperature. They successfully tested the ANN for flow ranges between 0.0 m<sup>3</sup>/s (0 gpm) and 0.0025 m<sup>3</sup>/s (39.6 gpm), pipe diameters between 100 mm (3.94 inch) and 300 mm (11.81 inch), densities between 500 kg/m<sup>3</sup> (4.17 lb/gal) and 1500 kg/m<sup>3</sup> (12.52 lb/gal), and liquid temperatures between 25 °C (77 °F) and 75 °C (167 °F). Since measured flow velocity is also influenced by the flow profile, research efforts are underway to increase the number of sound paths and therefore increase accuracy by eliminating the dependence of flow profile and flow disturbance (Hauptmann et al., 2002).

## **1.2.4 PULSED ULTRASOUND DOPPLER METER**

### **Overview and Principle of Operation**

A Doppler flow meter works on the principle of reflection of transmitted sound waves by the moving particles (solids/bubbles) in the liquid. The reflected waves have a different frequency than the transmitted sound waves (Figure 3). The difference in frequency between the transmitted and reflected sound waves is proportional to the velocity of the fluid. The Doppler meter can be used to measure an instantaneous one-dimensional velocity profile in opaque fluids along a fixed measurement axis (Kotze et al., 2013). Its low accuracy and low reliability make it generally unsuitable for drilling applications (Schafer et al., 1992).

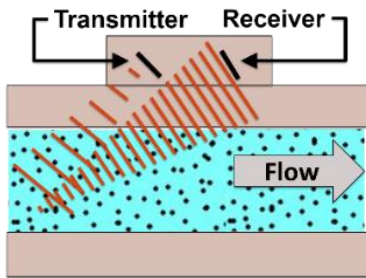


Figure 3- Schematic of a Pulsed Ultrasound Doppler Meter.

It is a non-invasive meter which is highly sensitive to temperature variations, but is generally not affected by other fluid properties. If temperature corrections are not incorporated accuracies better than 2-8% are not achievable, especially at outflow from hot wells with partially filled pipe (Schafer et al., 1992). Another limitation of the Doppler technology is its inability to account for changes in sound speed due to changes in particle concentration in the fluid, resulting in measurement errors (Armanini et al., 2003). For correct implementation of the Doppler meter, it is required that the transducer probe size and sound frequency be selected based on the application (Armanini et al, 2003).

The velocity profile using a Doppler meter is typically estimated through a weighted mean of the Doppler power spectra from each depth (Wiklund et al., 2014). Reliable velocities can only be obtained after averaging over a number of pulses (in some instances greater than a thousand) (Armanini et al., 2003). The time between two emissions determines the resolution of the velocity profile. If the time between two emissions is long, fast particles will have moved too much to yield echoes that correlate (Armanini et al., 2003). The Doppler flow meter has poor SNR in the regions close to the conduit walls. Turbulence measurements near the pipe wall, where velocity gradients are high, are very difficult to obtain even for pipes with diameters as large as 46mm (1.81 inch, Vural et al., (2014)). These turbulence measurements are possible if invasive techniques are used (Kotze et al., (2013)). Kotze et al., (2015) are working on testing and developing advanced methods to make turbulence measurements in 25.54 mm (1 inch) and 50.8 mm (2 inch) pipes using non-invasive methods and high grade stainless steel pipes.

### **1.2.5 MAGNETIC FLOW METER**

#### **Overview and Principle of Operation**

The conventional magnetic flow meter has two sensing electrodes and operates on the principle of Faradays law of electromagnetic induction. Voltage induced across the conductors of the magnetic meter as the fluid moves at right angles through a magnetic field is proportional to the velocity of that fluid. The velocity can then be multiplied by the pipe area to get VFR. Magnetic flow meters have been around since the 1950's and are field-proven devices. These meters can handle up to 41.37 MPa (6000 psi) of pressure.

Typical lifetime for the fluid passageway through the meter is ten years and five years for the transmitter. It requires less energy to operate compared to an ultrasonic or Venturi meter.

The meter is highly accurate and the output signal is only marginally affected by changes in fluid properties provided the fluid is conductive (Schafer et al., 1992). It is not a good choice for oil-based and synthetic-based muds as these muds are non-conductive (Reitsma, 2010). It can be used to monitor the flow of a dirty, cuttings-laden and variable viscosity fluids such as water based drilling muds (Speers et al., 1987, Wang et al., 2007). Single phase volumetric axisymmetric flow rate can be measured with an error as low as +/- 0.05% (Leeungculsatien et al., 2013). For axisymmetric flow a straight pipe of at least five to ten pipe diameters is required before flow enters the meter. This can add to cost and may not always be feasible if space is limited (Xu et al., 2001). Experiments with a 304.8 mm (12 inch) meter showed an accuracy of greater than 99% for velocities greater than 0.076 m/s (0.25 ft/s) and for Reynolds number values greater than 19000. The accuracy drops considerably for Reynolds number less than 19000, with values as low as 97% for Reynolds number around 10,000 (Prettyman et al., 2014).

### **Limitations and Sources of Error**

The meter accuracy deteriorates with time due to wear of both the tube and the electronics. The meter is unable to distinguish between air and liquids and is therefore not recommended for aerated fluids. When the velocity profile is highly non uniform, for example downstream of partially open valves (in single phase flows), the meter's accuracy can be seriously affected. Lack of axial symmetry can lead to errors of 10% or more

(Horner et al., 1998) and is typically observed in multiphase and cuttings-laden fluid flows in both horizontal and inclined pipes. These variations are weight driven and occur principally in the direction of gravity resulting in a minimum axial velocity at the lower side of the pipe cross section and a maximum velocity at the upper side of the pipe cross section (Leeungculsatien et al., 2013).

### **Overcoming Limitations**

For single phase non-axisymmetric flows, smoothening the magnetic field by increasing the number of electrodes from two to six and making the magnetic field more homogenous (by changing pole geometry), can significantly reduce errors (almost by an order of magnitude in some cases). For verification purposes a standard two electrode flowmeter, compatible with a 50 mm (1.97 inch) pipe diameter, was modified to a six electrode version (Horner et al., 1998). The pole geometry was also modified to produce a more homogeneous magnetic field. A non-axisymmetric flow downstream of an orifice resulted in errors of 60% or greater for the two electrode version and less than 5% for the six electrode version. The error reduction for an axisymmetric flow was not as dramatic, since the errors in both the two and six electrode version resulted from inhomogeneous magnetic fields. Under more realistic flow conditions, such as using a 90-degree bend or a combination of two 90-degree bends with perpendicular planes and a ball tap immediately upstream of the inlet flange, resulted in errors between 0.5% and 1.0% using a two electrode meter and 0.2% for a the six-electrode meter (Horner et al., 1998).

Wang et al., (2007), showed that minor variations of fluid conductivity encountered in the cross section of multiphase flows only have a minimal effect on the operation of

electromagnetic flow meters, especially if the volume fraction of the non-conducting dispersed phase is less than about 0.4. Leeungulsatien et al., (2013) used a multi-electrode design to extract axial velocity profiles of multiphase non-axisymmetric flows in which the conductivity of the dispersed phase is much lower than that of the continuous phase. Xu et al., (2001) presented a technique to reduce the random error encountered by the multi-electrode meters in addition to the systematic error that is inherent to the meter.

### **1.2.6 FLOW PADDLE METER**

#### **Overview and Principle of Operation**

The flow paddle (sometimes referred to as the flapper) is a relatively cheap and light weight meter that is used to measure flow rate in a non-pressurized return line. It is the most widely used meter for out-flow detection, given the relatively higher cost of a Coriolis meter (Ritchie et al., 2008). It consists of a spring mounted paddle that extends down into the fluid flow. The paddle is deflected by the force of the moving fluid. The fluid force is a function of fluid height and velocity and thus the flow rate. Despite its widespread adoption in the drilling industry, the readings from this meter are neither very accurate nor repeatable (Schafer et al., 1992).

#### **Limitations and Sources of Error**

Deflection of the flow paddle is affected by fluid viscosity. It is therefore not recommended to be used in settings where mud density and viscosity are constantly changing (Schafer et al., 1992). The readings require skilled personnel for interpretation. Furthermore, frequent flow checks and constant calibration are required (Vieira et al.,

2009, Chopty et al., 2011). The maintenance requirements for the meter are high, especially for water based muds, due to collections of cuttings, “gumbo” (i.e. reactive clays adhering to the paddle), etc., especially during pipe tripping operations in and out of the well (Ritchie et al., 2008, Chopty et al., 2011). Software techniques can partially correct for this and other non-flow related problems (Ritchie et al., 2008). Transient waves in the return flow line can result in scatter as high as 35% of average readings, which in turn complicates meter calibration (Schafer et al., 1992). Errors as large as +/- 15% have also been recorded even when data was averaged over 1-5 minutes (Schafer et al., 1992, Vieira et al., 2009). The use of these meters is best suited for non-accurate flow rate estimates in normal drilling operations (Wagner et al., 1993, Johnson et al., 2014).

### **1.2.7 ROLLING FLOAT METER (RFM)**

#### **Overview and Principle of Operation**

The RFM was developed by Sandia National Laboratories to measure the flow rate of drilling fluids in the return line. The meter is also suitable for kick detection when used in the return line (Whitlow et al., 1996). It works by measuring the fluid height in an inclined gravity fed partially filled pipe. These measurements can be used to monitor drilling fluid flow rates, from less than 11.36 m<sup>3</sup>/h (50 gpm) to 227.12 m<sup>3</sup>/h (1000 gpm) or more. Fluid height is measured at the location where the force due to gravity is balanced by the force due to friction at the pipe walls. At this location the velocity and the height of the liquid become steady; therefore, an increase in flow rate directly corresponds to a

change in fluid height. Readings from this meter are independent of temperature or mud property changes.

The RFM was tested on a relief well which was drilled to contain a wildcat natural gas well drilled near Bakersfield, CA. It detected several kicks that were not observable with a paddle meter or the pit volume totalizers (Mansure et al., 1999). Experimental field data showed a typical accuracy of 98% with an upper range of 99.5%. In many instances, at a flow rate of approximately 204.41 m<sup>3</sup>/h (900 gpm), the RFM reading matched the magnetic flowmeter reading within +/- 1.14 m<sup>3</sup>/h (5 gpm, Schafer et al., 1992). It also detected very small delta flow rates (inlet – outlet) and performed better than the Doppler and paddle flow meter in the tests. An algorithm, called the Intelligent Drilling Monitor (IDM), is used with the RFM and pump stroke counter. The IDM allows for detection of delta flow as low as 4.54 m<sup>3</sup>/h (20 gpm) at the rig site (Corser et al., 2000).

The meter is prone to damage by high pressure pulses in the pipe, which can occur while drilling geothermal wells due to outflow liquids flashing to steam (Staller et al., 1998). Furthermore, if steel is present in the outflow, then constant cleaning of the meter is required to minimize reading errors from the electromagnetic Hall Effect sensor used in the RFM. In spite of its good performance as documented above, no data could be found to validate the very limited use of this meter in the drilling industry.

### **1.2.8 PIT VOLUME TOTALIZER (PVT)**

#### **Overview and Principle of Operation**

PVT is a system of sensors and alarms used for detecting kicks and lost circulation by monitoring changes in pit mud volumes and flow rates. Abnormal changes in pit volume are a prime indicator of mud loss or fluid influx, and PVT is one of the most common methods for determining this delta flow in drilling systems (Cayeux et al., 2013). PVT is more suitable for determination of total pit volume gained or lost over a period of time, and is less suitable for rapid and accurate response to gas kicks or lost circulation events (Schafer et al., 1992, Johnson et al., 2014).

### **Limitations and Sources of Error**

The data quality of the PVT sensor package is limited by the large surface area of the tanks (Hannegan et al., 2015). A one-inch change in a 37.16 m<sup>2</sup> (400 ft<sup>2</sup>) tank translates roughly to 0.95 m<sup>3</sup> (6 bbl, Fraser et al., 2014). On floating rigs, such small changes to pit volume can be masked by wave heave, and a flow check is often required to determine the exact cause of pit level change (Schafer et al., 1992, Thiago et al., 2016). Another issue when using PVT is that one must wait until the mud flows all the way down the return line from the riser to the pits, while most rigs require an increase in the pits of at least 1.59 m<sup>3</sup> (10 bbl) for reliable detection and the triggering of an alarm. During this time and volume lag there may actually be a much larger total influx in the wellbore (Fraser et al., 2014, Johnson et al., 2014). Changes in pit volume are also affected by several transient effects, unrelated to kick or loss circulation. For example, the compressible nature of the mud requires a larger volume of mud to fill a well that is flowing versus a static well. Similarly, mud volume is affected by temperature changes, mud loss at shale shakers, sand traps, degassers, etc. (Cayeux et al., 2013, Johnson et al., 2014). Lack of proper communication

when weighing up the mud or transferring out of tanks could also result in measurement errors and false positive alarms.

### **Overcoming Limitations**

Pitch and roll effects on floating rigs can partially be mitigated by increasing the number of level detection sensors to four, combined in sensor pairs and mounted in opposite corners diagonally from each other (Brakel et al., 2015). Errors due to transient effects discussed above can be mitigated using a process called fingerprinting. Fingerprinting is done with data from wells under similar drilling conditions as well as using the well's flow behavior from previously observed mud pump stops and starts. However, fingerprinting can pose its own challenges when sufficient comparison data is either not available or is dissimilar to the flow behavior being observed, and different flow rates or durations between start and stop times of the mud pump are used. Furthermore, the fingerprinting process can be difficult to automate, as it relies on the data-interpreter to subjectively select the appropriate reference pattern (Cayeux et al., 2013).

## **1.2.9 TRIP TANKS**

### **Overview and Principle of Operation**

A trip tank is a small metal tank with a capacity of about 3.18–7.95 m<sup>3</sup> (20-50 bbls). It is typically used for flow checks during tripping, when there is no circulation through the well bore. It has a volume and shape such that the small changes in fluid volume may register and has divisions at 0.16 m<sup>3</sup> (1 bbl) intervals to measure flow into or out of the

tanks (Johnson et al., 2014). It is designed for accurate volume readings with a resolution of approximately 0.04 m<sup>3</sup> (0.25 bbls, Cayeux et al., 2013).

### **Limitations and Sources of Error**

In offshore applications the accuracy of the trip tank is affected by wave heave (Mammadov et al., 2015, Fraser et al., 2014). Another downside of trip tank is that it can only be used when the well is not circulating (Fraser et al., 2014, Hannegan et al., 2015). The trip tank may need to be filled several times if pulling a long section of drill pipe out of hole and frequent fill-ups to the hole need to be made. This makes it difficult to monitor the trip tank for kick and lost circulation events while pulling the pipe and simultaneously filling the trip tank (to ensure adequate drilling fluid). To overcome this, the driller often stops pulling pipe when filling the trip tank. This, however, adds to the overall tripping time, which translates in additional costs for high unit cost operations such as deep-water well construction. (Cockburn, 1987).

#### **1.2.10 DIFFERENTIAL PRESSURE FLOW METERS**

The major types of differential pressure flow meters used in drilling applications are the Classical Venturi, Halmi Venturi, HBX, Wedge and V-cone meters. These meters work by measuring the pressure drop across a constriction in the meter and correlate the pressure drop to the flow rate using Bernoulli's theorem. The constriction is introduced by reducing the pipe diameter in a conical shape for the Classical and Halmi meters, and as a step change for the HBX meters. For the Wedge meter the constriction is in the shape of a wedge and V-cone meters use a cone shaped obstruction inserted in the meter body. The

working life of these meters is usually several decades. After years of use, the meters may show an accuracy drop of about 2% against specification. The accuracy in some cases can be restored by replacing liners and other wear components.

Prettyman et al., (2014) conducted tests on all five of the above meters to compare their performance. They used 304.8 mm (12 inch) instruments with water as the test fluid, and determined their accuracy both experimentally and theoretically for Reynolds number values less than 1,000,000. The ratio of the diameter of the constriction to the actual pipe diameter was fixed at 0.6. Both experimental and theoretical results showed accuracy below 82% for the Wedge, V cone and HBX Venturi meters. The low accuracy of these meters makes them unsuitable for upstream drilling applications where significantly higher accuracies are required. For Reynolds number values greater than 100,000 the Classical and Halmi meters showed an average experimental accuracy of approximately 99.4% and 98.6% respectively. For Reynolds number values less than 100,000 their accuracies begin to deteriorate significantly dropping below 95% at Reynolds number values of approximately 10,000. A Reynolds number value of 100,000 or greater amounts to a water flow rate of 34 m<sup>3</sup>/h (150 gpm) in a 101.6 mm (4 inch) pipe. For a 1437.92 kg/m<sup>3</sup> (12 lb/gal) mud at 5 mPa.s (5 cp) the flowrate required would be 102.26 m<sup>3</sup>/h (450 gpm) in the same size pipe. Therefore, the high Reynolds number value limitation renders even the Classical Venturi and Halmi venture type meters unsuitable for most drilling mud applications where flow rates in a 101.6 mm (4-inch) pipe are between 0 m<sup>3</sup>/h (0 gpm) and 272.54 m<sup>3</sup>/h (1200 gpm). Furthermore, it is unclear how viscosity or slurries would affect meter performance.

## **1.3 Density Measurement Meters**

### **1.3.1 MUD BALANCE - UNPRESSURIZED**

The mud balance is used to manually measure density of non-aerated fluids. The mud cup is filled with fluid, and the density is measured by sliding a rider along a graduated arm until it is balanced. The position of the rider indicates the density of the mud sample. It is not recommended for use with compressible aerated fluids, because air in heavy and viscous muds can range from 0% to 14%, resulting in errors up to 10% of true density. Furthermore, as mud density can vary across the mud pits, the mud sample used to estimate density, is never a true representative sample (Nickles, 1972).

### **1.3.2 MUD BALANCE - PRESSURIZED**

The pressurized mud balance is different from the unpressurized mud balance in that the mud cup that can be pressurized (typically using a 222.4 N (50 lbf)) using a modified cup/lid assembly and a plunger (Baker et al., 1998). By applying a force to the plunger and thereby degassing the sample manually, density readings within 1.3% of absolute density (when pressurized to 1723 kPa (250 psig)) can be measured (Nickles, 1972). To use this meter, the cup is filled and the lid is secured in place by keeping the check valve open, so that excess mud may flow out. The plunger is filled with the sample mud and attached to the check valve. The check valve is kept open and the plunger is pushed down. The plunger is then slowly released until the check valve has risen to about

6.35 mm (0.25 inches) and then removed. This locks the pressure into the cup and measurements can now be made (Baker et al., 1998).

### **1.3.3 GAMMA RAY DENSITOMETER**

A gamma-ray densitometer (Figure 4) is a very accurate instrument used in the oil and gas industry for fluid bulk density measurement, Gas Volume Fraction (GVF) characterization, and liquid interface identification (Khorsandi et al., 2011). It is the most reliable non-invasive (external to process piping) method for measuring the void fraction inside a thick stainless steel pipe (Park et al., 2007). The density of a flowing oil-field slurry, independent of its composition, can be measured within  $29.96 \text{ kg/m}^3$  (0.25 lb/gal) of true density. Density of normal drilling muds through the rig's standpipe can be measured at accuracies of  $11.98 \text{ kg/m}^3$  (0.1 lb/gal) of true density (Guest et al., 1973). The gamma ray densitometer is ideally suited for high accuracy density measurements downstream of the mud pumps, where flow conditions include a full pipe and homogeneously mixed mud. Several commercial multiphase flow meters (MPFMs) use gamma-densitometry as part of their measurement systems (Arubi et al., 2011). The drawbacks of this meter are the logistical challenges it creates for the operator due to the fact that it requires a radioactive source, and the additional costs that go along with it. In addition to the extra paper work, the source has to be tracked throughout its life and then disposed of in a safe way. It also has to be properly handled during storage, transportation and installation (Tjugum et al., 2002).

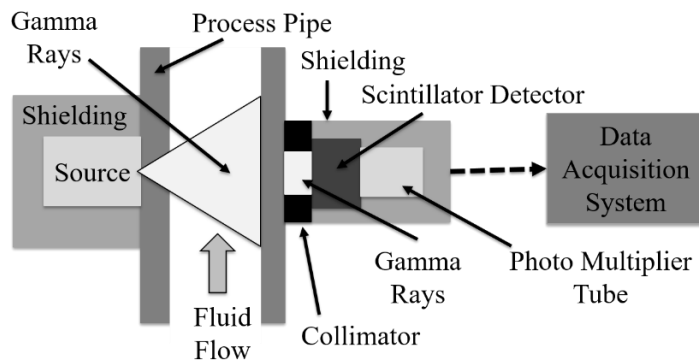


Figure 4- Detailed schematic of a single beam gamma ray densitometer.

Gamma ray densitometry works by comparing the incident gamma rays to the attenuated gamma rays after they have passed through the object whose density is being measured. The densitometer is composed of a gamma ray source, a collimator, a scintillation detector (operated in count mode), and a data acquisition system that includes an amplifier, a single or multi-channel analyzer and a counter (Figure 4 (b)) (Park et al., 2007). While a single energy source gamma ray meter is sufficient for two-phase void fraction measurements, a dual energy source meter is required for three-phase void fraction measurements. It is important that a meter be selected such that the detectors are operating in count mode (counting the total number of photons) vs the current mode (measuring the total energy deposited by the photons), to avoid drift in the output signal (Babelli, 1997).

The gamma ray densitometer has two major methods of operation: transmission mode and scattering mode. In the transmission mode, the detector is placed along the centerline of the source, whereas in scattering mode, multiple detectors are placed at different angles from the source centerline. The transmission-based technique is preferred, as it is more sensitive to density changes and results in greater counting statistics

(Khorsandi et al., 2011, Khabaz et al., 2015). The attenuation of gamma rays at low energies is dominated by the photoelectric effect (a function of material atomic number and incident ray energy). At high energies, as typically used in gamma ray densitometry, attenuation is dominated by Compton scattering (a function of the material density and incident ray energy, Heismann et al., 2003, Roshani et al., 2014, Arubi et al., 2011). Therefore, high energy gamma ray densitometry is very suitable for determining density of unknown materials (Roshani et al., 2014). Density lookup charts for a given source and detector combination can be built using empirical attenuation data from different materials of known density. The density of an unknown material in the field can then be interpolated using these look up charts and the amount by which it attenuates gamma rays (Khorsandi et al., 2013).

Homogenous mixing of multiphase or aerated liquids is essential for accurate density predictions. The accuracy depends on parameters such as source-to-detector distance, pipe wall thickness, fluid density, source energy, radiation intensity, and duration over which measurement data is averaged. Kumara et al., (2010) tested a flowing multiphase fluid comprised of oil and water using an Am-241 source. The flow velocities ranged from 0.25 m/s (0.82 ft/s) to 1 m/s (2.28 ft/s) in a 56 mm (2.2 inch) stainless steel pipe. An accuracy of 99.03% was achieved when data was averaged over 50 seconds of exposure time. The accuracy increases as exposure times are increased.

The most widely used gamma ray source is Cs-137, which has radiation energy of 661.6 keV. Another popular source is Am-241 which has radiation energy of 59.5 keV (Kumara et al., 2010). Am-241 has higher sensitivity than Cs-137 when trying to

distinguish between low density phases such as oil and water, or water and air. This is because energies  $<100\text{KeV}$  offer a better contrast between the mass absorption coefficients of oil and water. The mass absorption coefficient is low for low-density fluids like water, oil and air for energies greater than  $100\text{keV}$ . Therefore, gamma rays pass through these fluids without much attenuation, making it hard to distinguish between the two due to reduced contrast (Kumara et al., 2010).

Thallium activated sodium iodide, NaI (TL) scintillators are the most commonly used detectors due to their high light output yields, which result in high efficiency and energy resolution (Khabaz et al., 2015). Detectors are rated on their robustness, stopping efficiency, count rate and sensitivity to vibrations and temperature. Another common detector used is the semiconductor based CdZnTe type. These detectors are superior but significantly more expensive than the NaI(TL) (Tjugum et al., 2002). A data acquisition system and a data processing system are also needed to interpret the data collected by the detectors.

### **Gas Volume Fraction (GVF) Determination using the Gamma Ray Densitometer**

Gamma ray technology can be used to determine air content in the mud. The mud air content be as high as 20% and, if not accounted for, can result in significant errors in estimating the well bore bottom hole pressure. Dual energy gamma ray detection results in higher accuracy compared to single energy gamma ray detection for GVF determination of two-phase fluids. Furthermore, accuracy is improved by incorporating the scattering measurements along with the transmission measurements (Åbro et al., 1999, Tjugum et al., 2002). Another advantage of dual mode operation is that it can provide flow-regime

information and information on the salinity of the water fraction (Tjugum et al., 2002). Salinity has a very significant impact on gas volume fraction measurement when using low energy radiation (Tjugum et al., 2002). If GVF begins to exceed 70%, discrepancies in the gas phase fraction measurement between the hard (high energy) and soft (low energy) gamma counts, caused by phase slip, can be observed (Arubi et al., 2011).

Åbro et al., (1999) conducted a study with the aid of polypropylene phantoms using dual energy gamma rays. The phantoms were used to simulate the fluid in the pipe, with different GVF's, under stratified, annular and homogeneous flow conditions. Of the three detectors used, one detector was used in scattering mode and the remaining two detectors were used in transmission mode. Machine learning algorithms and Monte Carlo simulations were used for data correction. The models were tested on homogeneous, annular and stratified liquid flows. The exposure time was set to 600 seconds. It was observed that the average error in the determination of GVF is about 15% if only one detector at 180 degrees from the source is used. However, the average error is 3% using all three detectors.

Another study conducted by Tjugum et al., (2002) used dual energy gamma rays and three detectors. The inner diameter of the pipe used was 50.8 mm (2 inch). An exposure time of 100 seconds was used. The transmission detectors used were semiconductor-based CdZnTe type. The scattering detector used was a scintillation detector. Geiger-Muller counters were not used due to their slow response rate. Tests included simulation, flow loop tests and static tests on a 50.8 mm (2 inch) pipe for annular flows. It was found that the dependency of GVF on the flow regime is reduced by using two transmission detectors.

Furthermore, the scattered radiation in combination with the transmitted radiation was used to calculate water salinity and thereby salinity-independent GVF. The study found that an optimal detector and source configuration exists, depending upon the flow regime.

## **1.4 Mass Flow Rate Measurement Meters**

### **1.4.1 U-TUBE CORIOLIS METER**

#### **Overview and Principle of Operation**

The U-tube Coriolis meter (Figure 5 a), also referred to as the Coriolis meter, works by measuring the phase difference of oscillating flow tubes between the inlet and outlet of the instrument. Under no flow condition, the two tubes oscillate in phase (Figure 5 c) and during flow they oscillate out of phase (Figure 5 d), typically in a sinusoidal fashion. The phase difference is proportional to the mass flow rate through the tube. Most commercial Coriolis meters use two identical tubes to make the phase shift measurements more sensitive. The two tubes are typically driven at their first natural frequency (Svete et al., 2015). The phase difference is registered by two pick-off sensors located at the inlet and the outlet of the meter as shown in Figure 5 b and forms the basis of the final derived reading. The electromagnetic drive coil and magnet shown in Figure 5 (b) ensure the tubes are always oscillating at constant amplitude and at their first natural frequency. The driving force/gain changes as the mass of the flow tube (function of fluid density) changes.

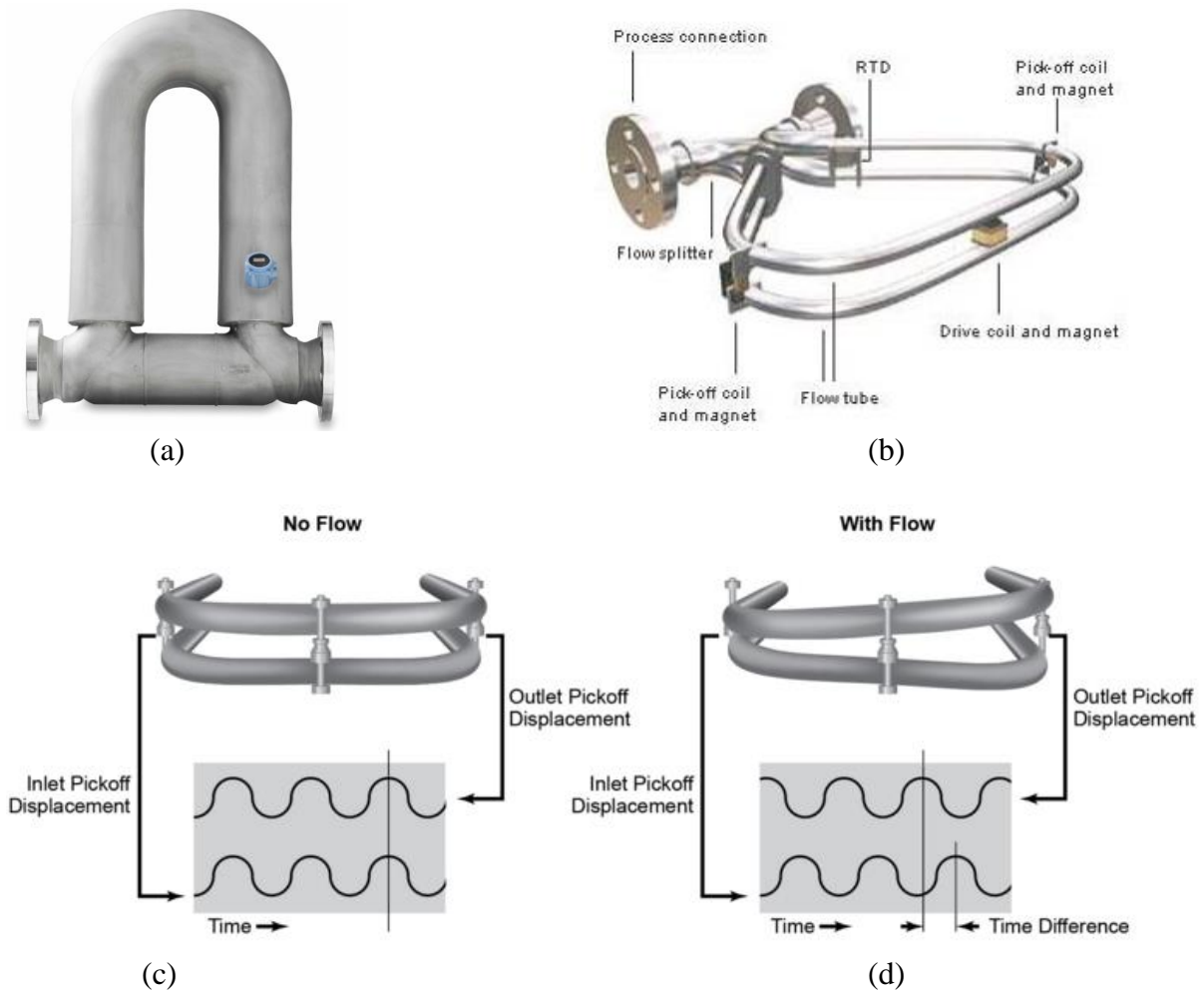


Figure 5- (a) U tube Coriolis meter (b) Internal components (c) Coriolis meter working principle at no flow (d) Coriolis meter working principle at flow  
 (Image courtesy Emerson, reproduced with approval).

A Coriolis meter is very accurate for single phase fluid flow (both gas and liquid). However, it underperforms with aerated liquids and batch flow which are fairly common while drilling (Reizner et al., 2004, O'Banion et al., 2013, Pushnov et al., 2013, Henry et al., 2004, Seeger et al., 2005, Liu et al., 2001). The Coriolis meter, in spite of its shortcoming in dealing with aerated fluids is considered as the meter of choice for MPD.

It is valued for its high accuracy and quick measurement times during drilling operations (Bruton et al., 2016, Driedger et al., 2013, Piccolo et al., 2015). It is a relatively expensive and large meter, only suited for pressures below 7.2 MPa (2.5 ksi). It is typically used to measure mass flow rate in the wellbore return line due to its pressure limitations and poor response to handling pulsations from triplex pumps.

### **Limitations and Sources of Error**

A Coriolis meter is not recommended for fluids with entrained air or slug flow/batching applications, where air and fluid follow in rapid successions (Reizner, 2004, Henry et al., 2004). Even after batching has stopped and single phase flow has resumed, it can take the meter more than 10 seconds to resume normal operation (Henry et al., 2004). The meter lacks the fast response time (defined by how quickly a device can respond to periodically changing flow rates) and low latency (defined as the time it takes for the flow meter output to respond to a change in flow) required for batching operations (Reizner, 2004). Even the best Coriolis meters in the industry struggle with batch times of less than 0.5 seconds and some perform badly even at 20 seconds batch times (Reizner, 2004).

A study conducted using nitrogen and oil with GVF between 6% and 9% resulted in errors from -15% to 5% (Wang et al., 2014). Reizner et al., (2004) tested eight different manufacturer models and showed errors of up to 58% when aeration ranged from 2% to 4%. Aeration further reduces accuracy with increasing fluid viscosities and surface tension. It is observed that at 10 mm<sup>2</sup>/s (10 cSt) and with 3% to 15% GVF, accuracy could be as low as ±40%. The meter overestimates at larger GVF's and underestimates at lower GVF's (Reizner et al., 2004). Slurries can also affect the accuracy of the Coriolis meter. Depending

on the slurry, a 10% error can result if the Coriolis meter is operated below 40% of full range (Reizner, 2004). At low flowrates and aerated flow, the meter sometimes can provide high accuracy provided complete separation of the phases occurs between the two tubes (Reizner, 2004). One must also be careful in selecting designs from different manufacturers. Designs from each manufacturer are different and have their own advantages and shortcomings. For example, a meter from one manufacturer may work at high GVF while on the other hand a meter from another may stall even at low GVF's. However, at similar tube oscillating frequencies the meter characteristics are quite similar (Seeger et al., 2005).

### **Overcoming Limitations**

The bubble theory, the resonator theory and the damping theory (Pushnov et al., 2013) describe three types of phenomenon that arise in a Coriolis meter due to aeration. There is ongoing research to develop rigorous models that can correct for the errors caused by the bubble, resonator and damping effects (Pushnov et al., 2013).

The bubble theory aims to resolve issues that arise due to the amplitude of bubble oscillations inside the tube being greater than the tube oscillations. Wang et al., (2014) describe some of the limitations of the bubble model. These include errors not accounted for during high flow and low density changes and error variations that arise due to changes in damping, flow rate, and temperature. They propose a moving resonator model (MRM) and viscosity correction factors (which requires knowledge of liquid viscosity and GVF and is a complex function of bubble diameter, liquid viscosity and oscillation frequency) to account for some of these errors. Using the MRM technique, at 6% GVF, they showed

improvement on mass flow and density measurement errors from an uncorrected -9% to within  $\pm 1\%$  when water was used.

The resonator theory aims to resolve issues that arise from entrained volume of liquid inside the bubbles themselves. The errors from the resonator effect are a function of resonant frequency, the excitation frequency of the tubes, the air content and the process pressure.

The damping theory aims to resolve issues that arise due to the friction between the liquid, the bubbles and the pipe wall due to non-uniform distribution of bubbles (Pushnov et al., 2013). The damping effect causes significant flow tube damping to occur due to loss of mechanical energy from frictional interactions between the compressible air, fluid and tube wall (Pushnov et al., 2013). Aeration can result in damping of flow tube that is two orders of magnitude greater than damping that results from single phase fluid flow (Henry et al., 2004). Aerated liquids therefore require greater power from the drive system to maintain the natural frequency and amplitude of the tubes. In theory, the drive coils can be designed to meet the increased energy demands. In practice, however, this extra power is not available as the drive system power is limited for intrinsic safety reasons. Furthermore, the drive system tracking and response time is not fast enough. It struggles to keep pace with the changes in the damping force due to the chaotic nature of the bubbles in the fluid. Another problem when dealing with aerated liquids is the drive gain saturation, which often results in stalling of the meter (Reizner, 2004, Henry et al., 2004, Henry et al., 2005, Seeger et al., 2005). Drive gain saturation occurs when the controller's allowable current limit has been exceeded and the gain is therefore not sufficient to compensate for

damping. As a result, the tube dampens even more, leading to even a higher gain requirement. This eventually results in meter stalling.

To correct for the damping effect, a straight or slightly curved tube design has been proposed (Henry et al., 2005). This tube design allows for more uniform bubble distribution. In a vertical installation (meter inlet and outlet are perpendicular to the ground) using a straight tube, the bubbles get distributed uniformly enough to drive the error due to the damping effect to zero. Furthermore, the design is more compact and causes less pressure drop than the U-tube geometry. However, caution needs to be exercised, as the straight tube has a high excitation frequency, which can lead to the resonator effect dominating over the bubble effect. However, as long as there is a likelihood that the resonator effect will work to compensate the error caused by the bubble effect, the straight tube design is ideal. Also, the straight tube design has low tube oscillation amplitude, and therefore low-phase difference range and poorer signal-to-noise ratio. (Henry et al., 2005).

Another solution for dealing with aerated flows is to use Artificial Neural Networks (ANNs) and empirical models that can be customized to provide measurement corrections. ANNs or machine learning tools have been applied successfully to correct for errors for aerated fluids within a known range of operating conditions, after much data collection and laboratory experimentation. ANN's are able to capture patterns and trends from the complex set of data that is captured during experiments. If the operating conditions are changed, data will have to be recollected and the ANN reconfigured. The accuracy of the Coriolis meter measurements can be significantly increased using ANN's. Liu et al., (2001) customized and tested an ANN on a 25.4 mm (1 inch) Coriolis meter in a horizontal

alignment. An aerated fluid under low flow conditions was used. The ANN was able to reduce errors of 20% to within 2% for a fixed range of flow, temperature and void fractions. Gregory et al., (2008) customized and tested an ANN on a 203.2 mm (8 inch) Coriolis meter for a bunkering application. The meter was tested for GVF between 1% and 30% where errors can easily exceed 15%. The observed errors were between +3% and -6%, with a measurement repeatability between 97% to 99.8%. Wang et al., (2016) used ANNs to test meters at flow rates ranging from 700 kg/h (1543 lb/h) to 14500 kg/h (31967 lb/h) with GVF of 0% to 30% for both vertical and horizontal installations. Errors in corrected mass flow rate were between  $\pm 1.5\%$  and  $\pm 2.5\%$  respectively for both types of installations.

Research is also ongoing to improve the slow dynamic response and the poor performance of the Coriolis meter when handling flow from large, slower positive displacement pumps, especially in short batches. Slow dynamic response is not an issue when dealing with smaller or faster pumps as the flow pulsations tend to get averaged (Reizner, 2004). Efforts are also being devoted (Henry et al., (2004)) to address driver power limitations by using a two driver design model instead of a single driver design. Henry et al., 2004 also looked at reducing mass flow rate into the Coriolis meter by splitting the flow. Results, however, were not satisfactory due to the uneven distribution of air when the flow is split.

To improve meter performance for batching and slug flow applications where errors can easily exceed 15%, Henry et al., (2004) performed a study with a 76.2 mm (3 inch) Coriolis meter with a mass flow rate of 0.4 kg/s (6.64 gpm). For consistent batch sizes and when batching from full, the repeatability varied from 99.9% for a 10 s batch down to as

low as 90% for a 62 ms batch at nominal flow rate. When batching from empty they showed a repeatability of 99% for a 2 seconds or longer batch at nominal flow rate. Henry et al., (2006) tested a 76.2 mm (3 inch) Coriolis meter under slug flow conditions. A high viscosity oil with a flow range between 1 kg/s (15.85 gpm) and 10 kg/s (158.5 gpm) was used. For GVFs of less than 60%, 95% of the readings showed errors less than 5% for nominal density and less than 6% for nominal mass flow.

## **1.5 Tabulated Summary**

Table 1 provides a list of the meters reviewed in this paper, along with a brief overview of their capabilities. Table 2 and Table 3 provides a list of other density and flow meters respectively, that may be encountered while drilling and completing oil and gas wells; note that these have not been reviewed in detail in this paper.

Table 1- Tabulated summary of reviewed meters.

Meter Type	Inlet Volumetric Flow							Inlet Density			Outlet Volumetric Flow				Outlet Mass Flow
	Stroke Counter	Rotary Speed / VFD	Magnetic	Venturi Classical / Hallmi	HBX / Wedge / V-Cone	TTUF	Pulsed Doppler	Mud Balance Pressurized	Mud Balance Unpressurized	Gamma ray	Rolling Float Meter	Pit Volume Totalizer	Trip Tank (For Tripping only)	Flow Paddle	Coriolis
Volumetric Flow	✓	✓	✓	✓	✓	✓	✓	N/A	N/A	N/A	✓	✓	✓	N/A	✓
Mass Flow	N/A	N/A	N/A	N/A	N/A	N/A	N/A	N/A	N/A	N/A	N/A	N/A	N/A	✓	✓
Density	N/A	N/A	N/A	N/A	N/A	N/A	N/A	✓	✓	✓	N/A	N/A	N/A	N/A	✓
Invasive	No	No	Yes	Yes	Yes	No	No	N/A	N/A	No	Yes	Yes	Yes	Yes	Yes
7.5 KSI Pressure Rating	Yes	Yes	No	Yes	Yes	✓	✓	N/A	N/A	✓	N/A	N/A	N/A	N/A	No
Aeration (Homogeneous)	N/A	N/A	✓	UN	UN	✓	✓	✓	✓	✓	✓	✓	✓	✓	✓
Aeration (Non-Homogeneous)	N/A	N/A	✓	UN	UN	✓	✓	✓	✓	✓	✓	✓	✓	✓	✓
Overall Performance	✓	✓	✓	✓	✓	✓	✓	✓	✓	✓	✓	✓	✓	✓	✓
Inlet fluid : pressurized, aerated, homogenous slurry															
Outlet fluid : un-pressurized, partially filled pipe with cuttings laden, non-homogeneous, aerated and multiphase slurry															
<b>Legend</b>															
✓	Good performance														
✓	Average performance														
✓	Poor performance														
N/A	Not applicable														
UN	Unknown														

Table 2- Density meters not reviewed in this paper.

<b>Other not as Commonly used Density Measurement Techniques</b>
1. Pycnometer
2. Electrically weigh a fixed volume of fluid flow stream continuously
3. Pneumatically weigh a fixed volume of fluid flow stream continuously
4. Weigh a fixed volume of fluid flow stream continuously using vibrational effects

5. Continuously monitor fluid stream radioactive absorption
6. Meters using buoyant force measurement
7. Meters using hydrostatic head measuring techniques

Table 3- Volumetric flow meters not reviewed in this paper.

<b>Other not as Commonly used Flow Measurement Techniques</b>	
1. In-pipe vibrating tuning fork	10. Turbine meter
2. Doppler shift: insertion-type	11. Mechanical vane type
3. Cross-correlation Doppler	12. Radar flow sensor
4. Pulse multipath Doppler	13. Microwave flow sensor
5. Vibrating tube (straight flow-through)	14. Ultrasonic/Coriolis meter combined
6. Ultrasonic velocity profiling/ differential pressure meter combined	15. Sonar/Microwave meter combined
7. Continuous wave ultrasound Doppler	16. Float level meter
8. Cross correlation ultrasonic meter	17. Ultrasonic/Acoustic level meter
9. Sonar based meters	18. Manifolds for outflow

## 1.6 Discussion on Meters Reviewed

Typical flow conditions encountered at the inlet consist of a fully filled pipe and a homogeneously mixed aerated mud. At the outlet, typically the pipe is partially filled with a non-homogeneously mixed, multiphase, aerated, and cuttings-laden mud. These differences in flow conditions place very different demands on meters and result in

differences in meter performance. This section summarizes the best options available for making density and flow rate measurements at the well inlet and outlet, and highlights the gaps and needs that need to be addressed by further research and development.

### **1.6.1 OUTLET MASS FLOW RATE MEASUREMENT**

At the well outlet, the most suitable metering technologies provide density, VFR and mass flow rate measurements. For a customer, for whom the upfront capital costs are the primary driver, the flow paddle is a usable technology for measuring mass flow rate. For customers that demand the highest level of accuracy and repeatability, however, the Coriolis meter is the best choice. Constant advancements are being made to improve accuracy of the Coriolis meter for aerated, batch and slug flows. It has been shown that the demands on the meter are reduced and its accuracy improves when the aerated flow is homogeneous. Experiments were conducted to reduce the mass flow into the Coriolis meter by using a flow splitting mechanism. However, the results from these experiments were disappointing because of the inhomogeneity of the aerated outlet flow. It would be worthwhile focusing research efforts on developing and testing a slurry mixing device that makes the aerated fluid homogenous before it enters the Coriolis meter. Multiphase meters with multiple sensing technologies have long been used in downstream applications, and are finally making their way into upstream flow measurement with meter offerings. However, the performance of these meters still remains to be validated in the field and properly documented in peer-reviewed literature.

### **1.6.2 VFR MEASUREMENT WHILE TRIPPING**

The trip tank is the currently recommended metering technology for VFR measurement out of the well during pipe tripping operations. The primary limitations of the trip tanks are measurement inaccuracies that result from heave on floaters and the difficulty in making manual measurements while pulling the pipe and simultaneously filling the trip tank. The measurement inaccuracy due to heave can partially be mitigated by increasing the number of level detection sensors. Machine vision tools can also be used to correct for heave and to make automated high frequency real-time measurements of the trip tank level while pulling the pipe and simultaneously filling the trip tank.

### **1.6.3 INLET DENSITY MEASUREMENT**

At the inlet, the only meter that can currently provide real-time density measurements is the gamma ray densitometer. This meter has a radioactive source and provides delayed measurements that are averaged over a long time interval. Its long measurement times are a result of the low intensity (number of photons available per second) of the gamma ray source and the high density steel pipe in its path. The steel pipe is responsible for the majority of the attenuation experienced by the gamma rays, and is a major contributor to measurement noise. Long measurement times are therefore required in order to increase the signal-to-noise ratio (SNR). An alternative to increasing the SNR would be to increase the photon intensity and/or to use a pipe material that has a lower density but the same pressure-rating as steel. Such replacement materials for steel now exist and are recommended for significantly improving gamma ray densitometer

performance. The photon intensity can be increased by using a larger gamma ray source. Using such a larger source, however, could further complicate logistics and compromise safety. Another alternative would be to use high energy X-rays that are generated using a non-radioactive source. Such a meter would work on similar principles as the gamma rays. The intensity of these X-rays can easily be regulated by altering system voltage and current (Singhal et al., 2018).

The Coriolis meter has two major limitations that need to be addressed in order to make it compatible for the inlet flow conditions. Firstly, research is needed to improve the errors caused due to the flow pulsations from the positive displacement mud pumps. The areas of focus for research would include advancements in hardware design, better control algorithms, and the implementation of machine learning algorithms. The data for these machine learning algorithms would be generated from tests conducted under controlled settings using a variety of process fluid and flow conditions. Secondly, research is needed towards the development of meter tubes that can handle the high stand pipe pressures.

#### **1.6.4 INLET VFR MEASUREMENT OF NON-AERATED DRILLING FLUIDS**

For inlet volumetric flow measurements of non-aerated fluids, the pump stroke counter, rotary speed counter, or frequency output from a scalar variable frequency drive (VFD) are all good options for non-aerated muds when used with mud pumps that are relatively new and their accuracy is well-known. As pump components begin to wear, pumps need to be re-serviced and performance tests need to be repeated to restore the measurement accuracy of these meters. Continuously excited clamp-on TTUFs are in this

case a good option for flow measurement. Their performance is not affected by wear in pump components. With proper installation and calibration, the meters should be able to provide accuracy between 95% to 99% or larger at nominal flow rates. This accuracy however, deteriorates towards the lower end of the TTUF's flow range. A suggested remedy is to use two or more flow meters. The multiple meters can be selected such that their nominal flow is rated at the higher and lower end of the VFR expected through the stand pipe.

Magnetic meters would be an excellent choice for measuring flow rate of water based muds, if they can be designed to handle the high stand pipe pressures. Based on limited published data, the meters may suffer from loss in accuracy for flow at Reynolds numbers less than 20,000. If this happens, then a low flow TTUF in tandem with the magnetic meter can be used to maintain accuracy across the entire flow range. The Coriolis meter would be another good choice for measuring inlet VFR, provided it can be designed to handle the high pressures and flow pulsations produced by the mud pumps.

#### **1.6.5 INLET VFR MEASUREMENT OF AERATED DRILLING FLUIDS**

There are currently no meters that show excellent performance in measuring the flow rate of aerated drilling fluids at the well inlet. Performance of meters such as the pump stroke counter, the rotary speed counter, magnetic meters, and the continuously excited clamp-on TTUFs deteriorates significantly in the presence of air in the drilling fluid. An X-ray based sensor can achieve a higher measurement accuracy for aerated drilling fluids compared to that provided by current measurement technologies.

## **1.7 Conclusion**

A vast number of metering options are available for measuring density and flow rate of drilling and completions fluid and have been reviewed in this section. It is acknowledged that even when the right metering technology has been selected, the measured values often have low accuracy and low measurement frequency compared to that required during drilling of complex wells. These concerns exist both at the high pressure well-inlet and the low pressure well-outlet. Using an X-ray based meter, the technology for measuring density and flow rate at the high pressure inlet can be advanced such that these measurements can be made with an accuracy of 99% or greater at a measurement frequency of 1 Hz.

## 2 DENSITY MEASUREMENT USING X-RAYS

### 2.1 Introduction

It is highly desirable to monitor changes in mud density in a timely fashion, preferably in real-time, in order to maintain well control and optimum drilling conditions. The changes in drilling mud density occur due to entrainment of unwanted contaminants (1.5 SG – 2.6 SG) from the formation due to poor solids control or other factors. Mud density also changes during weighting-up operation where a high gravity solid (HGS) such as barite (4.2 SG) or hematite (5.26 SG) added intentionally to increase the density of the mud. Another scenario where the mud density changes is during a weighting-down operation where a solvent, which can be water-based (creating a water-based mud - WBM) or oil-/synthetic based (creating an oil-/synthetic based mud - OBM/SBM) with an emulsified invert brine phase, is added to the mud to reduce its density. The solvent along with the HGS and contaminants constitutes about 98% of the mud by volume concentration. The solids content of the contaminants in the mud is typically not allowed to exceed a maximum volume concentration (e.g. < 6%) due to negative effects on fluid viscosity, gel strength, and fluid loss control (Mitchell et al., 2017).

The density measurements are generally preferred on the high pressure side, since the density of the mud (which can be heavily aerated) under pressure is more representative of the downhole mud density than density measured at atmospheric pressures. Currently, gamma ray densitometers are the only meters that are suited for high pressure measurements of drilling mud density in real-time. Typical flow conditions encountered at

the inlet, such as a fully filled pipe and a homogeneously mixed mud, are very conducive to their use. However, in spite of their high measurement accuracy and relatively fast response times these meters have seen limited adoption in field. This is because the meters come with safety concerns due to the radioactive source required for gamma ray generation. Additionally, the source has to be tracked through its life and properly handled during storage, transportation, installation and disposal. Given these concerns and challenges, a majority of oil and gas operating and service companies use manual density measurements at the mud pits using a pressurized mud balance. To help change this rather antiquated and infrequent practice that relies on manual labor, research has been conducted in developing a non-radioactive, X-ray based densitometer as an alternative to the gamma ray meter. X-ray densitometry works on the same proven principles as gamma ray densitometry, without the latter's drawbacks. Furthermore, X-ray densitometry is not novel in itself and is fairly well established in the medical field, where it is routinely used to measure the density of bones.

There is also some evidence of past efforts by companies such as Schlumberger and Emerson to develop x-ray based sensors for real time density measurement. In 1996, a patent for an x-ray based meter capable of measuring fluid densities and water ratios in an oil/water/gas mixture flowing through a steel pipe was filed by Schlumberger (Stephenson et al., 1997). Tjugum et al., (2010) describes a prototype densitometer for a 73mm diameter pipe which developed by Emerson. The meter was designed to make density and gas volume fraction measurements and was designed to be incorporated into the Emerson

production stage low pressure multiphase meter. However, the reasons why none of these technologies failed to make it to the market are not clear.

This paper revisits the idea of a real-time densitometer based on X-ray measurements, showing that such an instrument is quite feasible and offers considerable merit for making measurements at high pressure conditions. We begin our discussion by providing an overview of X-ray attenuation basics required to make density measurements. A test setup used to conduct the experiments is then described. An implementation of a calibration system, necessary to make repeatable density measurements by accounting for time variability in the output of the X-ray system, is discussed. Since all experiments are conducted under static conditions, it also shown that density measurements for incompressible fluids are unaffected by flow-rate. Finally, the experimental results from three density estimation methods, an empirical method, and two different model-based methods, are presented and discussed.

## **2.2 Principles of X-ray Attenuation for Density Measurement**

For a homogeneous material such as single-phase drilling mud (or other well construction fluid) flowing through the high pressure standpipe of a drilling rig (where the sensor is to be located as shown in Figure 6) with a known inner diameter, attenuation for monochromatic X-rays is a function of the material density and mass attenuation coefficient ( $\mu_m$ ).

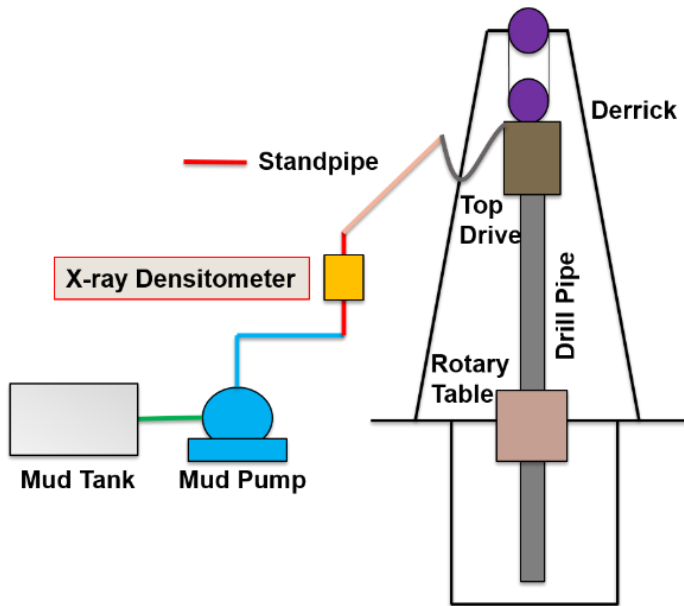


Figure 6: X-ray densitometer location on the rig.

A monochromatic energy source generates X-rays of a single energy, as opposed to a polychromatic energy source which generates X-rays ranging from 0 eV to the maximum source energy. X-ray attenuation is the process during which the X-ray beam loses energy as it propagates through a given medium. The mass attenuation coefficient is a constant that characterizes this rate of energy loss for the medium, independent of the density of that medium. For X-ray energies lower than 500 KeV, attenuation is primarily due to photoelectric absorption (which is a function of material atomic number and radiation energy (Heismann et al., 2003) and Compton scattering (function of material electron density and radiation energy (Nelson et al., 1991))). The photoelectric effect results in absorption of the X-ray photons by the medium, whereas Compton scattering results in the scattering of the X-ray photons with a simultaneous reduction in their energy. This

attenuation of monochromatic energy X-rays can be approximated by the Beer Lambert's law (see e.g. Roels et al., 2006).

$$I = I_0 e^{-\mu_m \rho t} \quad 4$$

where 'I', expressed in Gray Level Value (GLV), is the X-ray intensity incident on the detector after attenuation by medium in its path,  $I_0$ , also expressed in GLV, is the X-ray intensity incident on the detector after attenuation by air,  $\mu_m$  is the mass attenuation coefficient of the homogeneous medium ( $\text{cm}^2/\text{g}$ ),  $\rho$  is the density of the homogeneous medium ( $\text{g}/\text{cm}^3$ ), and  $t$  is the medium thickness (cm). The intensity values which can be represented by GLV, are calculated by averaging all the gray pixel values on X-ray radiographs. The estimation procedure for GLV is described in Chapter 2.3. If  $I$ ,  $I_0$ ,  $t$ , and  $\mu_m$  are known, Equation 4 can be used to estimate the density value  $\rho$ .

The value of  $\mu_m$  in Equation 4 is inversely proportional to the incident X-ray energy. As the energy of the incident X-ray increases, the value of  $\mu_m$  decreases (Limkitjaroenporn et al., 2012). As a consequence, higher X-ray energies have greater penetrating power through a medium than lower energy X-rays. In this work, we will consider a polychromatic X-ray energy source given its lower cost, size and complexity compared with the monochromatic energy source. The attenuation of the polychromatic X-rays is also commonly approximated by the Beer Lambert's law (Li et al., 2016; Hoag, 2007).

For a monochromatic X-ray traversing a medium, the value of  $\mu_m$  is constant. However, as polychromatic X-rays travel through the medium, they undergo greater attenuation during their initial interactions with the medium as compared to the interaction

in later medium sections (Salmon et al., 2014), resulting in a variation of  $\mu_m$  with depth (Blake et al., 1992). This is because the lower energy photons in the X-ray beam are preferentially removed compared to the higher energy photons (Blake et al., 1993, Hsieh et al., 2000). This process is known as beam hardening and leads to a shift in the spectral distribution of the incident X-ray beam towards higher effective energies (Blake et al., 1992). As a result of beam hardening, the instantaneous  $\mu_m$  for a polychromatic X-ray spectrum is a decreasing function of the medium depth. Therefore, the effective  $\mu_m$  for a given medium is also a decreasing function of medium depth.

In order to better estimate the values of  $\mu_m$ , for a given material, it is important to minimize the effect of beam hardening. One way to achieve this is to pre-harden the beam as it leaves the X-ray source by using a filter (Salmon et al., 2014). Pre-hardening or filtering helps to suppress the low energy photons from the X-ray beam before it interacts with the medium. The use of copper or aluminum as filter materials is a common practice (Accardo et al., 2005).

### **2.3 Experimental Test Setup**

The test setup used to measure density is shown schematically in Figure 7.

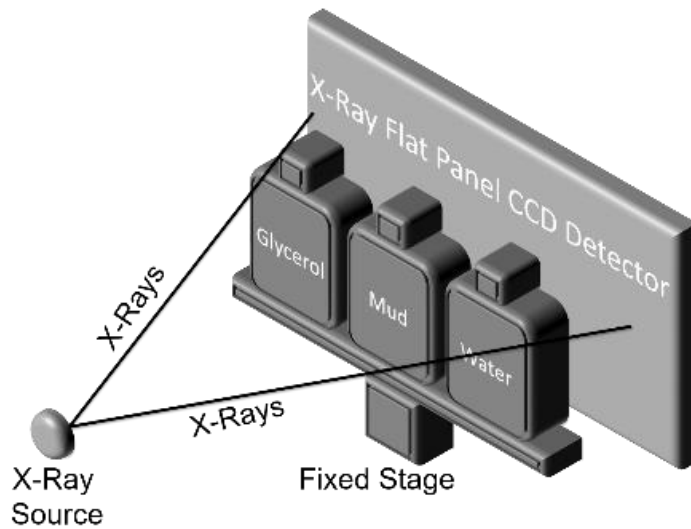


Figure 7- Experimental setup.

It consisted of an industrial X-ray tube source, a charge coupled device (CCD) flat panel detector, and the drilling mud sample mounted on a stage along with glycerol and water in plastic bottles. Glycerol and water samples were used for calibration purposes. The stage was fitted with grooves to enable exact alignment over various experimental runs. The distance of the test samples was thereby fixed relative to the source and the detector for each X-ray exposure. The depth of the sample bottle was 2.2 cm and its width and height were approximately 6.4 cm. The X-ray tube current and voltage were set to 100 kV and 44  $\mu$ A respectively. The exposure time was set to 1 second (i.e. 1 Hz frequency), and a 1 mm copper filter was used to filter the X-ray beam. A sample radiograph obtained from the experimental setup is shown in Figure 8. Quantities  $I_{\text{water}}$ ,  $I_{\text{mud}}$ , and  $I_{\text{glycerol}}$  were measured by averaging all the gray pixel values to a single GLV across windows 1, 2, and 3 respectively. Units of intensity 'I' are therefore expressed in GLV.

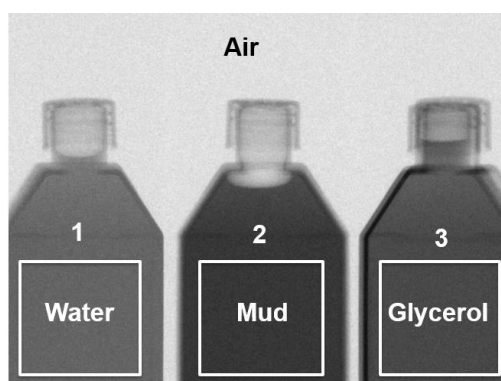


Figure 8- Sample radiograph.

## 2.4 X-ray System Calibration

The X-ray system exhibits minor drifts and fluctuations over time, which affect the repeatability of density measurements (Blake et al., 2004, Faulkner et al., 1995, Whitehouse et al., 1992). For this reason, the detectors need to be calibrated frequently. The fluctuations result from the loss of signal in the X-ray detectors (Haugh et al., 2012). Thus the solid state X-ray detector output fails to give the full measure of the X-ray intensity (Haugh et al., 2012). Another reason for the fluctuations is the degradation of system electronics over time (Faulkner et al., 1995). In conducting experiments using the test setup (Figure 7), fluctuations in system output were observed and are demonstrated using GLVs of water and glycerol samples (Figure 10).

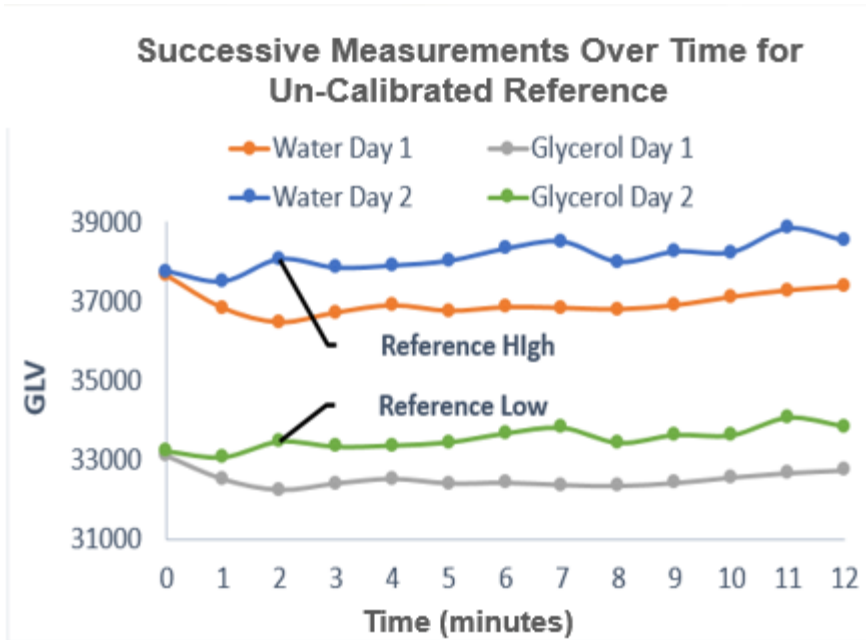


Figure 9- Variation in GL with time.

Figure 10 shows GLVs of the exact same water and glycerol samples radiographed at different time intervals. A maximum observed variation in GLV on day 2 was 6.5% higher than that on day 1. A maximum variation of 3.5 % in GLV was also observed during the minute intervals over which the radiographs were collected. To correct for the impact of system fluctuations on GLVs, a two-point calibration was implemented in real-time to ensure repeatability of measurement data. Such a calibration, which provides slope and offset correction, was selected in favor of a one-point calibration (which provides offset correction only) because the observed impact of system fluctuations on the GLV was both additive and multiplicative. A two-point calibration system was observed to provide good detector calibration provided the drilling mud GLVs fell inside the range of the GLVs of the reference materials. For mud GLVs outside this range, the calibration results were

unsatisfactory due to the significant scaling of uncalibrated values, which occurs as a result of extrapolation. It was also found that by making the reference GLV range narrower, the calibration results could be improved. To achieve the desired range of GLVs the reference materials can be of the same type and different thickness, different type and same thickness, or any combination of the two.

The reference calibration was achieved by setting  $I_{\text{water}}$  and  $I_{\text{glycerol}}$  values, from a radiograph of the test setup, as the reference high and reference low respectively as shown in Figure 10.  $I_{\text{water}}$  and  $I_{\text{glycerol}}$  values from all other radiographs were adjusted to correlate to these reference values as shown in Figure 10.

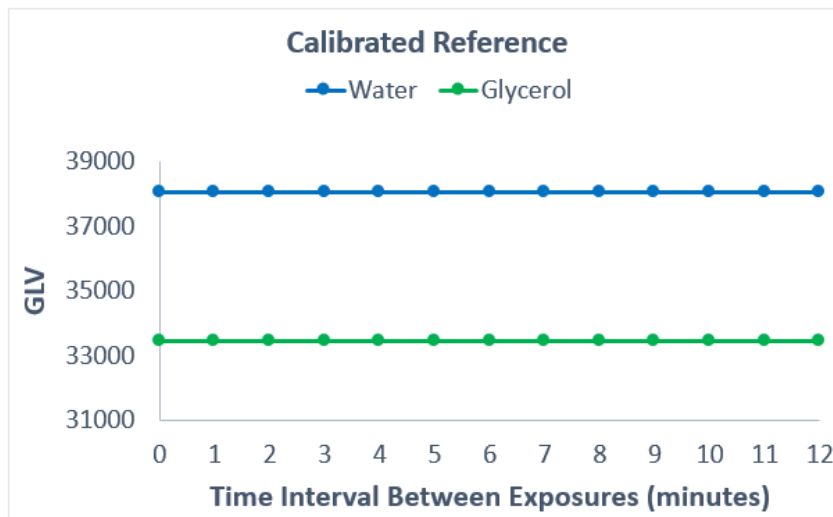


Figure 10- Implementing two-point calibration.

The calibrated value of any mud sample can be calculated as follows:

$$Cal. GLV = \frac{(Uncal. GLV - Ref. Low) * (Ref. Range)}{Raw Range} + Ref. Low \quad 5$$

Water (8.34 ppg) stored in a 2.2 cm deep plastic bottle, and a 5 cm thick aluminum (21.7 ppg) block, were used as the reference materials to test the effectiveness of the two-point calibration method. The GLVs for these calibration materials fluctuated around 39000 and 26500 respectively. The calibration was performed on GLVs of drilling muds with densities between 9 and 10 ppg. The errors associated with the calibration process, between day 1 and day 2, for different density muds, are shown in Figure 11.

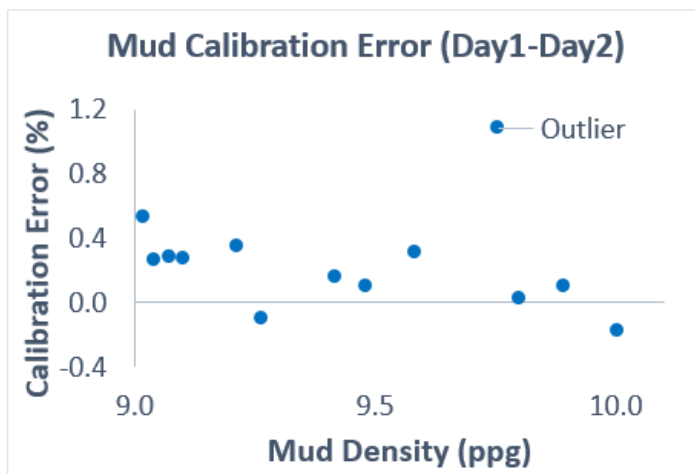


Figure 11- Errors after two-point calibration for muds of density in the 9–10 ppg range.

The calibration of the 8 mud samples, resulted in a mean error of 0.17% and had a standard deviation of 0.2%. The error bound was between -0.18% and 0.53% with a median value of 0.21%. The 1.09% error value was not considered for statistical analysis and was ignored as an outlier based on the very conservative version of the median absolute deviation (MAD) criteria proposed by Leys et al., (2013), for detecting outliers in sample data.

## 2.5 Experimental Verification that X-ray Attenuation is Unaffected by Flow-Rate for Incompressible Fluids

The test setup described in Figure 7 only permits experiments under static conditions. In the field, however, density measurements are also required when the drilling mud is flowing. It thus becomes necessary to show that GLVs collected under the static test conditions will also translate to field conditions, where the mud could be flowing. Based on the Beer Lambert's law (Equation 4) flow should not affect X-ray attenuation, provided the pressure that causes the flow does not alter the density of the fluid. At low pressures this hypothesis can be tested using water (assumed incompressible at low pressures). For the hypothesis test, non-aerated water was circulated through a 2.54 cm diameter and 1.5 m long acrylic pipe. Its velocity was varied between 0-64 gpm at a maximum pressure of 30 psi. A source voltage of 200 kV and a source current of 1.1 mA were used. The flow loop that was used to conduct the tests is shown in Figure 12.

Thirty radiographs each, were collected at the no-flow and flow conditions. The distribution of the GLVs from the no-flow and flow conditions is shown in Figure 13. A null hypothesis ( $H_0$ ) that X-ray attenuation is not affected by flow rate, i.e.  $\mu_{\text{Flow}} = \mu_{\text{No-Flow}}$ , was used, where  $\mu$  signifies the sample mean. The alternate hypothesis ( $H_A$ ) was therefore that X-ray attenuation is affected by flow rate, i.e.  $\mu_{\text{Flow}} \neq \mu_{\text{No-Flow}}$ .



Figure 12- Schematic of flow loop that was used for testing X-ray attenuation dependence on flow rate.

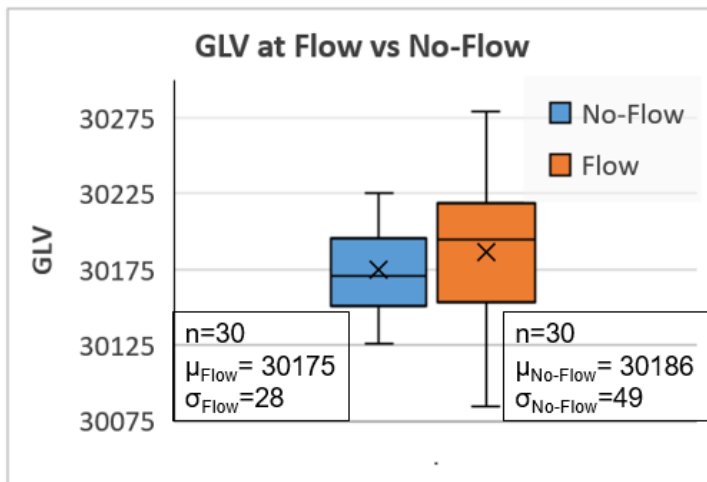


Figure 13- Descriptive statistical values for the sampling distribution.

An unpooled, independent sample, two-tailed t-test ( $t(46) = 1.07$ ) results in a P-value of 0.29. The P-value is far greater than the typical 0.05 threshold required to reject

$H_0$  (Lehman et al., 2013). Since, the hypothesis test was not significant, it was concluded that X-ray attenuation, for a fluid is unaffected by flow rate. The hypothesis was conducted under the assumption that the fluid is incompressible. Field drilling muds flowing through the rig stand pipe, however, are compressible in nature. At high pumping pressures such as those in the stand pipe, even water exhibits compressible behavior.

## **2.6 Density Estimation Methods**

Three approaches were developed to estimate mud density from GLVs. The first is an empirical approach, where look-up tables are created by mapping sensor GLVs onto mud density values through in-lab experiments. These look-up tables can then be used in the field to linearly interpolate mud density based on real-time GLV data. The goal of the experiments, which were conducted to develop the empirical method, was to determine the minimum density interval, at which to collect GLVs in the lab to ensure a greater than 99% in-field estimation accuracy using the look-up table approach.

The second method is a model-based approach where experiments are conducted in-lab to determine the  $\mu_m$ 's of the expected mud constituents. Beer Lamberts law is then used to measure the density of field muds using their real-time GLVs and these  $\mu_m$  values. For both of these methods, density measurement results are shown for two cases. The first case is when the change in mud density is only due to fluctuations in the concentration of HGS, for example during weighting up a clean mud. In the second case the change in mud density is due to the fluctuations in concentration of contaminants, that get entrained in the mud as a result of drilling.

The third method uses an exponential model to estimate mud densities and can be used to quantify changes in mud density due to fluctuation HGS concentrations. The number of lab measurements required to implement this method is significantly less than the other two methods. Work is underway to develop this method to model changes in mud density due to fluctuating contaminant concentrations as well.

All experiments to validate the density methods were conducted using the test setup described in Figure 7. Water stored in a plastic bottle was used as one of the calibration materials and an aluminum block was used as the second calibration material. All tested mud samples were free of entrained air and their density was measured using a standard API density cup.

## **2.6.1 EMPIRICAL METHOD**

### **2.6.1.1 Fluctuating HGS Concentrations**

Experimental results, using a WBM viscosified with Xanthan Gum (XC) and weighted with hematite, showed that the minimum density interval required to generate the look-up tables and ensure greater than 99% field accuracy was 1 ppg. The effect on GLVs as hematite/HGS content in the mud is changed is shown in Figure 14.

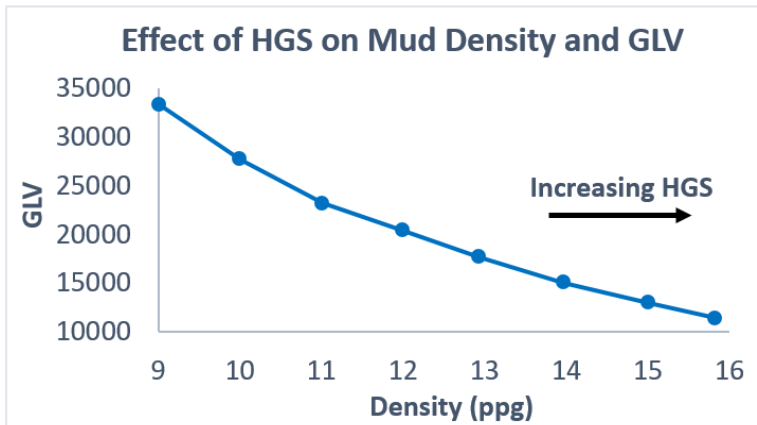


Figure 14- Effect of HGS on mud density and GLV.

To test the empirical method, 13 unknown muds with densities between 9 and 10 ppg and 9 unknown muds with densities between 12 and 13 ppg were radiographed 5 times each. The GLVs from these radiographs were used to linearly interpolate mud densities using the data in Figure 14. The resulting density estimation errors for low and medium density muds are shown in Figure 15 and Figure 16 respectively.

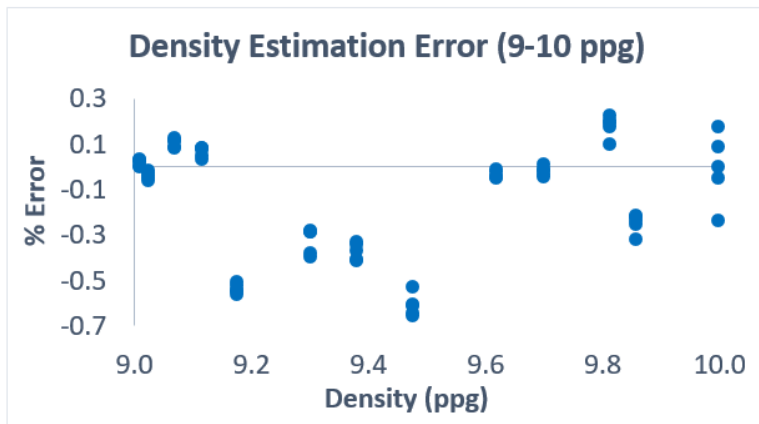


Figure 15- Error distribution for low density muds.



### 2.6.1.2 Fluctuating Contaminant Concentrations

For the contaminant experiment, the mud was composed of water viscosified with XC polymer, and weighted with hematite. Contaminant (OM#4 ball clay, SG ~2.6) volumetric concentration in the mud was varied between 0 and 8%. The effect on base mud density due to addition of contaminants is shown in Table 4.

Table 4: Drilling mud density and composition used for experimental evaluation of the density estimation methods.

Test Muds with Contaminants												
Sample #	1	2	3	4	5	6	7	8	9	10	11	12
Base Mud Density (ppg)	9.03	9.03	9.03	9.03	9.51	9.51	9.51	9.51	9.95	9.95	9.95	9.95
% Contaminants by Volume	0	1	4	8	0	1	3	6	0	1	4	8
Final Measured Density (ppg)	9.03	9.15	9.50	9.92	9.51	9.65	9.86	10.19	9.95	10.11	10.46	10.85

Experimental data showed that data points collected at 1 ppg density intervals along tracks of increasing HGS and 8% volume concentration along tracks of increasing contaminants, represented by the four corners of the plot in in Figure 19 were adequate for mapping and thereby estimating the density of unknown mud samples with an accuracy of 99% or greater. These data points are represented by sample numbers 1, 4, 9 and 12 in Table 4.

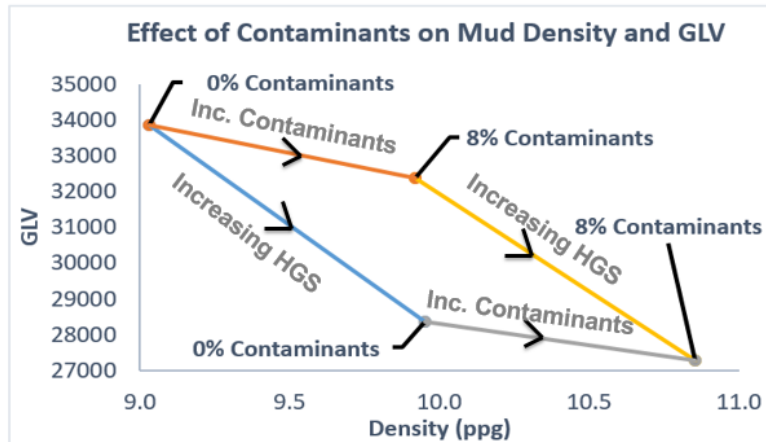


Figure 18- Effect of contaminants on mud density and GLV

The mappings were used to create a lookup table, which was generated by dividing the plot in Figure 19 into 50x50 bins along the tracks of increasing HGS and contaminants respectively. In order to implement the empirical method, the initial density of the mud needs to be measured using a standard API density cup and either the percentage of HGS or the percentage of contaminants already entrained in the mud needs to be measured. These measurements, along with the corresponding GLV reading from the X-ray detector, can then be used to find the position of the mud in the lookup table. The density of the mud will then continue to change in the direction of increasing HGS during weighting-up operations and will change in the direction of increasing contaminants during drilling. The new density can be determined in real-time by searching for any subsequent change in GLV and its corresponding density value in the lookup table.

To validate this approach, twelve non-aerated mud samples, denoted by ‘final measured density’ in Table 4 were radiographed 5 times each, for a total of 60 radiographs. The resulting GLV from the 60 radiographs were then used to linearly interpolate mud

densities, using the look-up table that was created from data in Figure 19. The density estimation errors that resulted from using the look-up table are shown in Figure 19. The estimation errors resulted in a ME of -0.09% with a SD of 0.30%. The error bound was between +0.82% and -0.87% with a median value of 0.08%

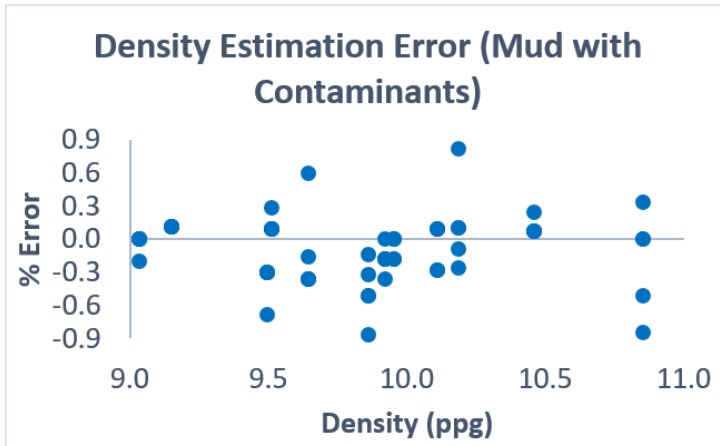


Figure 19- Error distribution for mud with contaminants.

### 2.6.2 MODEL BASED METHOD #1

Unlike the empirical method, the model based method does not rely on look-up tables to estimate density. Instead, it uses the Beer Lamberts law (Equation 4) and the knowledge that the depth of the sample is known to estimate density.

For a given homogeneous mud sample, its mass attenuation coefficient ( $\mu_{m\_mud}$ ) can be determined using Equation 6.

$$\mu_{m\_mud} = -\ln\left(\frac{I}{I_0}\right) / \rho_{mud} t \quad 6$$

where  $\mu_{m\_mud}$  is the mass attenuation coefficient of the homogeneous mud sample ( $\text{cm}^2/\text{g}$ ) and  $\rho_{mud}$  is the density of the mud sample as measured by the standard API density cup, or by the pressurized mud balance when in the field ( $\text{g}/\text{cm}^3$ ).

When an unknown amount of materials (with a pre-determined mass attenuation coefficient ( $\mu_{m\_suspension}$ ) and density ( $\rho_{suspension}$ ) get entrained in the mud, the proportion of the original mud in the sample bottle changes. The unknown proportions of the original mud and the additionally suspended materials in the sample bottle are indicated by Equation 7.

$$t = t_{mud} + t_{suspension} \quad 7$$

where  $t_{mud}$  is the unknown proportion of the original mud in the sample bottle (cm) and  $t_{suspension}$  is the unknown proportion of suspended materials in the sample bottle (cm).

The new value of the x-ray intensity ( $I_{new}$ ) after an influx of unknown amount of materials can be determined by using Equation 8.

$$I_{new} = I_0 \exp -(\mu_{m\_mud}\rho_{mud}t_{mud} + \mu_{m\_suspension}\rho_{suspension}t_{suspension}) \quad 8$$

Equation 8 states that the total x-ray attenuation by the modified mud sample is equal to the x-ray attenuation by its individual constituents (i.e., the unknown proportions of the original mud and suspensions). Values of  $t_{mud}$  and  $t_{suspensions}$  can be calculated using Equations 7 and 8, and Equation 9 is then used to calculate the density of the modified mud.

$$\rho_{modified\_mud} = (\rho_{mud}t_{mud} + \rho_{suspensions}t_{suspension})/t \quad 9$$

Finally:

$$\rho_{mud} = \rho_{modified\_mud} \quad 10$$

Equations 6 through 10 can be used recursively to determine the density of the drilling mud in real-time.

Experimental density measurement results using the model-based method are presented for two cases. The first case is when the change in mud density is due to changes in HGS concentration. In the second case the change in mud density is due to the fluctuations in contaminants concentration.

#### **2.6.2.1 Fluctuating HGS Concentrations**

To test the model-based method for changing HGS concentrations, 13 unknown WBMs (viscosified with XC polymer) with densities between 9 and 10 ppg, and 9 unknown WBMs with densities between 12 and 13 ppg were radiographed 5 times each. For the 9-10 ppg unknown mud samples the 9 ppg mud was treated as the original mud and for the 12-13 ppg unknown mud samples the 12 ppg mud was treated as the original mud. Hematite was considered to be the additionally suspended material in this experiment. The procedure used to determine the  $\mu_m$  values of the original mud and hematite is described in Section 2.6.2.5 and Section 2.6.2.6 respectively. The density estimation errors that resulted from using the model-based method are shown for the low and medium density muds in Figure 20 and Figure 21 respectively. The estimation errors resulted in a ME of 0.04% with a SD of 0.23%. The error bound was between +0.53% and -0.58% with a median value of -0.01%. The error distribution for the model based method had a narrower spread and a

smaller absolute ME as compared to the empirical method. Therefore, the model-based method appears to be more precise and a better estimator of density than the empirical method when no contaminants are present.

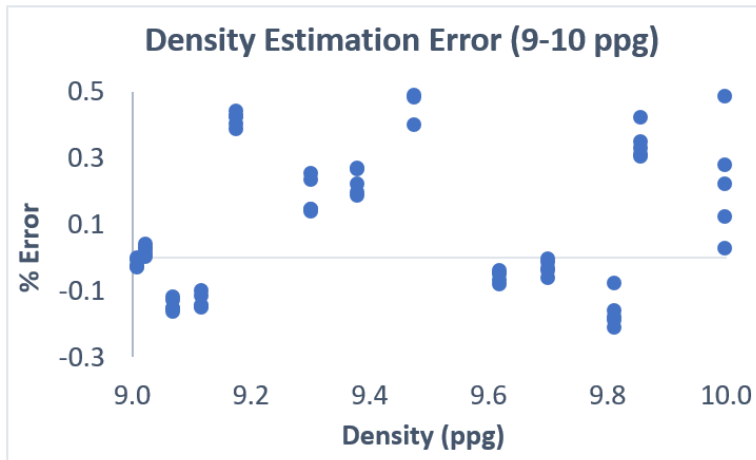


Figure 20- Error distribution for low density muds.

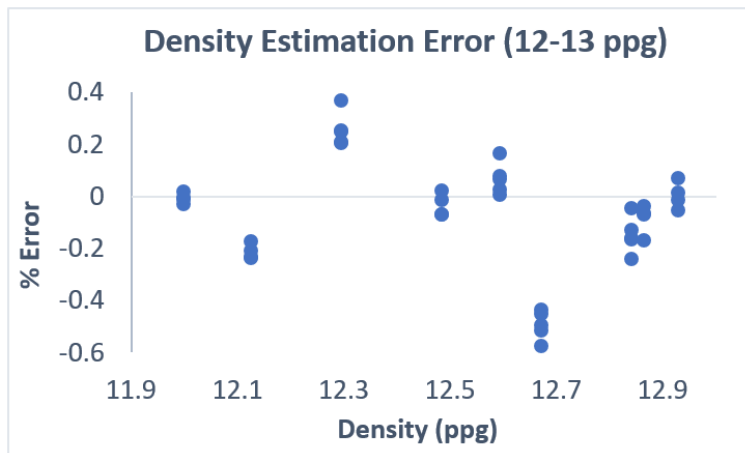


Figure 21- Error distribution for medium density muds.

### 2.6.2.2 Fluctuating Contaminants Concentrations

For the contaminant experiment a 9 ppg WBM (viscosified with XC polymer) weighted with hematite was used as the original mud. The original mud was further weighted with hematite to create three base muds with densities of 9.03, 9.51 and 9.95 ppg respectively. Contaminant (OM#4 ball clay, SG ~2.6) volumetric concentration in the base muds was varied between 0 and 8%. The effect on base mud density due to addition of contaminants is shown in Table 4. The  $\mu_m$  value of hematite from Section 2.6.2.6 was used to estimate the densities of the base muds and the  $\mu_m$  value of OM#4 ball clay from Section 2.6.2.7 was used to estimate the densities of the final muds. Each of the 12 non-aerated final muds in were radiographed 5 times each. The density estimation errors of the 12 final muds that resulted from using the model-based method are shown in Figure 22.

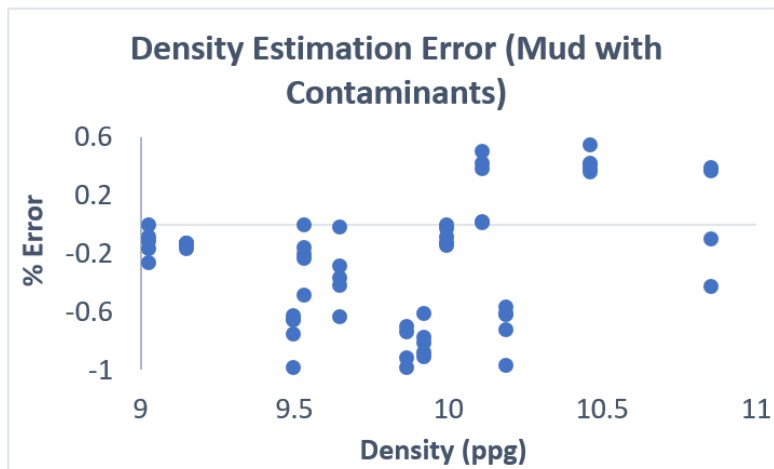


Figure 22: Error distribution for mud with contaminants.

The estimation errors resulted in a ME of -0.26% with a SD of 0.43%. The error bound was between +0.54% and -0.99% with a median value of -0.17%. The error distribution for the model based method had a similar spread and a larger absolute ME compared to the empirical method. Therefore, the empirical method appears to be a better estimator of density when contaminants are present.

### 2.6.2.3 Determining $I_0$

$I_0$  is the X-ray intensity, measured in GLV, incident upon the detectors in the absence of any attenuating material. However, it is often not possible to measure  $I_0$  directly from the detectors, as the detectors reach saturation unless an attenuating medium is present. If the X-ray spectrum is monochromatic, implying no beam hardening and constant mass attenuation coefficients, Equation 11 (derived using Beer Lamberts law) may be used to calculate  $I_0$ . Where,  $I_1$  and  $I_2$  are GLVs of an attenuating medium with density ' $\rho$ ' and width  $t_1$  and  $t_2$  respectively. The calculated  $I_0$  value is independent of material density ' $\rho$ ' and widths  $t_1$  and  $t_2$ .

$$I_0 = \exp\left(\frac{d_2 \ln(I_1) - d_1 \ln(I_2)}{t_2 - t_1}\right) \quad 11$$

For a polychromatic X-ray spectrum, however, beam hardening does occur, which causes the mass attenuation coefficients to vary with medium depth. As a result, the  $I_0$  values calculated using Equation 11 are affected by the choice and width of the material. The calculated  $I_0$  values for various  $t_1$  and  $t_2$  combinations of water samples, at an X-ray source voltage and current of 200 kV and 300  $\mu$ A respectively are shown in Figure 23.

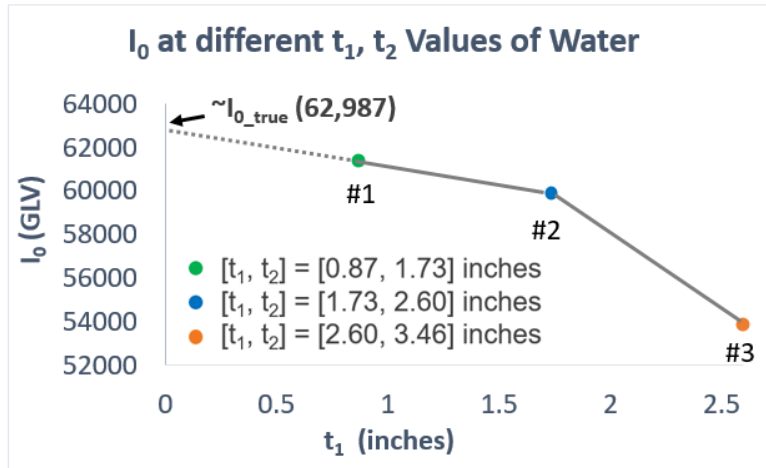


Figure 23-  $I_0$  values calculated using Equation 11 for water samples.

Figure 23 shows that the rate of increase of calculated  $I_0$  decreases with decreasing sample depth combinations ( $t_1, t_2$ ). The Y-intercept of the line connecting points #1 and #2 in Figure 23 was used to estimate the true  $I_0$  ( $I_{0\_true}$ ) value, which was determined to be 62,987. If necessary, even better estimates for  $I_{0\_true}$  can be obtained by further reducing the sample widths.  $I_{0\_true}$  values which ranged from 61,759 to 57,951 were also calculated for acrylic, aluminum, and steel samples at source voltages and currents of 60 kV/1900  $\mu$ A, 100 kV/44  $\mu$ A and 125 kV/100  $\mu$ A.

Figure 24 shows that in accordance with theory, the mass attenuation coefficient of water is a continuously decreasing function of sample depth for  $I_{0\_true}$  values of 62,987 or greater. However, at smaller  $I_{0\_true}$  values of 61,000 and 58,000 for example, this is no longer true. Figure 24 also shows that at  $I_{0\_true}$  values close to 62,987 the change in mass attenuation coefficient with sample depth is more linear in comparison to the change at  $I_{0\_true}$  values that are much larger (68000 for example).

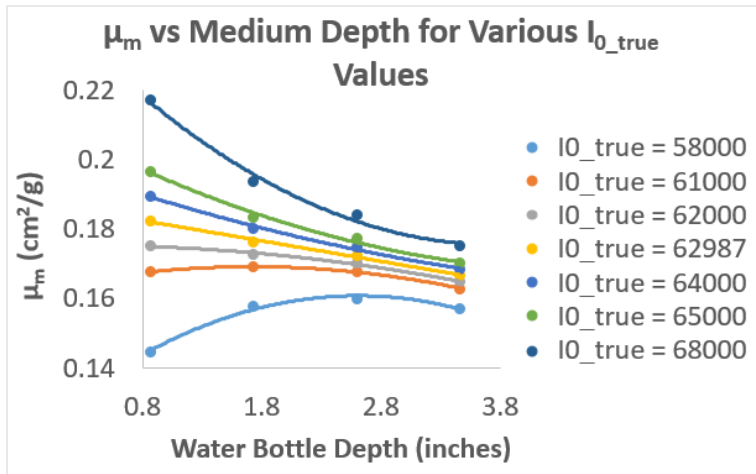


Figure 24-  $\mu_m$  distribution at different  $I_{0\_true}$  values.

The larger  $I_{0\_true}$  values are undesirable as they make it more difficult to estimate the values of mass attenuation coefficients during experiments. In practice, the  $I_{0\_true}$  value is either recorded from the region of the radiograph where no attenuation medium is present or otherwise ascribed the maximum GLV that can be output by the detector. Since a 16-bit CCD flat panel detector was utilized for the experiments described in this paper, an  $I_{0\_true}$  value of 65,536 was used.

#### 2.6.2.4 Determining ' $\mu_m$ ' of the Original Mud, HGS and Contaminants

The mass attenuation coefficients for the original mud, HGS and contaminants need to be calculated at 1 ppg mud density intervals to ensure 99% measurement accuracy using the model-based method. For illustration purposes a 9 ppg original mud is used.

#### 2.6.2.5 Calculating ' $\mu_m$ ' of the Original Mud

The 9 ppg original mud was formulated by using water as the solvent, XC polymer as the viscosifier, and hematite as the weighting agent. The mud was then placed in a 2.2 cm wide sample bottle and radiographed at a source voltage and current of 100 kV and 44  $\mu$ A respectively. The  $\mu_m$  value for the 9 ppg mud, denoted by  $\mu_{m_9}$ , was calculated to be 0.28  $\text{cm}^2/\text{g}$  by using Equation 12. A similar process was used to calculate the  $\mu_m$  value for the 12 ppg mud, which was calculated to be 0.366  $\text{cm}^2/\text{g}$ .

$$\mu_{m_9} = -\ln\left(\frac{I_9}{I_0}\right) / \rho_9 t \quad 12$$

where  $I_9$  is the measured GLV of the 9 ppg mud and  $\rho_9$  is its measured density ( $\text{g}/\text{cm}^3$ )

#### 2.6.2.6 Calculating ‘ $\mu_m$ ’ of the HGS

Hematite was added to the 9 ppg original mud to increase its density to 9.1 ppg (denoted by  $\rho_{9.1}$  ( $\text{g}/\text{cm}^3$ )) and 10 ppg (denoted by  $\rho_{10}$  ( $\text{g}/\text{cm}^3$ )). The 9.1 ppg and 10 ppg mud samples were placed in 2.2 cm wide sample bottles and radiographed. Their GLVs were measured and are denoted by  $I_{9.1}$  and  $I_{10}$  respectively. The estimated proportion of hematite, denoted by  $t_{e\_HGS\_9.1}$  (cm) and  $t_{e\_HGS\_10}$  (cm), added to increase the density of the 9 ppg mud to 9.1 ppg and 10 ppg respectively was calculated by substituting a guess value for  $\mu_{m\_hgs\_9}$  ( $\text{cm}^2/\text{g}$ ) in Equations 13 and 14.

$$I_{9.1} = I_0 * \exp -(\mu_{m_9} \rho_9 (t - t_{e\_HGS\_9.1}) + \mu_{m\_hgs\_9} \rho_{HGS} t_{e\_HGS\_9.1}) \quad 13$$

$$I_{10} = I_0 * \exp -(\mu_{m\_9} \rho_9 (t - t_{e\_HGS\_10}) + \mu_{m\_hgs\_9} \rho_{HGS} t_{e\_HGS\_10}) \quad 14$$

The  $t_{e\_HGS\_9.1}$  and  $t_{e\_HGS\_10}$  values were then used to calculate the estimated density of the 9.1 ppg (denoted by  $\rho_{e\_9.1}$  (g/cm<sup>3</sup>)) and 10 ppg (denoted by  $\rho_{e\_10}$  (g/cm<sup>3</sup>)) muds respectively using Equations 15 and 16.

$$\rho_{e\_9.1} = (\rho_9 (t - t_{e\_HGS\_9.1}) + \rho_{HGS} t_{e\_HGS\_9.1}) / t \quad 15$$

$$\rho_{e\_10} = (\rho_9 (t - t_{e\_HGS\_10}) + \rho_{HGS} t_{e\_HGS\_10}) / t \quad 16$$

Finally, an estimated density error denoted by  $E_{e\_HGS}$  (%) was calculated using Equation 17.

$$E_{e\_HGS} = \left| \frac{\rho_{e\_9.1} - \rho_{9.1}}{\rho_{9.1}} \right| + \left| \frac{\rho_{e\_10} - \rho_{10}}{\rho_{10}} \right| \quad 17$$

A  $\mu_{m\_hgs\_9}$  value that minimized  $E_{e\_HGS}$  was used as mass attenuation coefficient of hematite for muds in the 9-10 ppg range, and was determined to be 0.61 cm<sup>2</sup>/g. A similar process was also used to calculate the mass attenuation coefficient for muds in the 12-13 ppg range, and was determined to be 0.50 cm<sup>2</sup>/g.

### 2.6.2.7 Calculating ‘ $\mu_m$ ’ of the Contaminants

To determine the mass attenuation coefficient of contaminants, 1% and 8% by volume concentration of OM#4 ball clay were added to 9 and 10 ppg muds respectively, resulting in measured density values of 9.13 ((denoted by  $\rho_{9.13}$  (g/cm<sup>3</sup>)) and 10.93 (denoted

by  $\rho_{10.93}$  (g/cm<sup>3</sup>) ppg respectively. The 9.13 ppg and 10.93 ppg mud samples were placed in 2.2 cm wide sample bottles and radiographed. Their GLVs were measured and are denoted by  $I_{9.13}$  and  $I_{10.93}$  respectively. The estimated proportion of OM#4 ball clay, denoted by  $t_{e\_Clay\_9.13}$  (cm) and  $t_{e\_Clay\_10.93}$  (cm), added to increase the density of the 9 ppg and 10 ppg muds to 9.13 ppg and 10.93 ppg respectively was calculated by substituting a guess value for  $\mu_{m\_Clay\_9}$  (cm<sup>2</sup>/g) in Equations 18 and 19.

$$I_{9.13} = I_0 * \exp -(\mu_{m\_9} \rho_9 (t - t_{e\_Clay\_9.13}) + \mu_{m\_Clay\_9} \rho_{Clay} t_{e\_Clay\_9.13}) \quad 18$$

$$I_{10.93} = I_0 * \exp -(\mu_{m\_10} \rho_{10} (t - t_{e\_Clay\_10.93}) + \mu_{m\_Clay\_9} \rho_{Clay} t_{e\_Clay\_10.93}) \quad 19$$

The  $t_{e\_Clay\_9.13}$  and  $t_{e\_Clay\_10.93}$  values were then used to calculate the estimated density of the 9.13 ppg (denoted by  $\rho_{e\_9.13}$  (g/cm<sup>3</sup>)) and 10.93 ppg (denoted by  $\rho_{e\_10.93}$  (g/cm<sup>3</sup>)) muds respectively using Equations 20 and 21.

$$\rho_{e\_9.13} = (\rho_9 (t - t_{e\_Clay\_9.13}) + \rho_{Clay} t_{e\_Clay\_9.13}) / t \quad 20$$

$$\rho_{e\_10.93} = (\rho_{10} (t - t_{e\_Clay\_10.93}) + \rho_{Clay} t_{e\_Clay\_10.93}) / t \quad 21$$

Finally, an estimated density error denoted by  $E_{e\_Clay}$  (%) was calculated using Equation 22.

$$E_{e\_Clay} = \left| \frac{\rho_{e\_9.13} - \rho_{9.13}}{\rho_{9.13}} \right| + \left| \frac{\rho_{e\_10.93} - \rho_{10.93}}{\rho_{10.93}} \right| \quad 22$$

A  $\mu_{m\_Clay\_9}$  value that minimized  $E_{e\_Clay}$  was used as mass attenuation coefficient of OM#4 for original muds in the 9-10 ppg range, and was determined to be 0.236 cm<sup>2</sup>/g.

### 2.6.3 MODEL BASED METHOD #2

To account for changing HGS concentrations in drilling fluids in the 8-20 ppg range 10 lab measurements, at 1 ppg intervals, are required for the empirical method. For model based method #1 the number of required lab measurements is 20. Preparing 10 or 20 different samples of mud for purposes of data collection can be a cumbersome process. The model based method #2 reduces this upfront work as it only requires 6 lab measurements. The model is described by a the following relationship

$$\mu^* = -\ln\left(\frac{I}{I^*}\right)/t^*, 0 < t^* < t \quad 23$$

where 't' is pipe inner diameter (mm), 'I', expressed in Gray Level Value (GLV), is the X-ray intensity incident on the detector after attenuation by medium in its path,  $I^*$  which is calculated using the Beer Lambert's law, is the X-ray intensity incident on the detector after attenuation by the solvent contained in a pipe with an inner diameter of t (GLV),  $\mu^*$  is an attenuation coefficient of the homogeneous medium (mm<sup>2</sup>/g), and  $t^*$  is the unknown proportion of the HGS in the drilling fluid (mm).

Experiments have shown that  $\mu^*$  varies directly as the 4<sup>th</sup> power of  $t - t^*$ . To determine this 4<sup>th</sup> order relationship between  $\mu^*$  and  $t - t^*$  a minimum of 5 data points, at equidistant intervals from each other and spanning the entire t range, are needed. This

relationship can be used to determine the value of  $\mu^*$  and the corresponding value  $t^*$  such that:

$$\mu^* t^* = -\ln\left(\frac{I}{I^*}\right) \quad 24$$

The  $t^*$  value can then be used to calculate the density of mud in real-time, with an accuracy of greater than 99%, using Equation 25.

$$\rho_{mud} = (\rho_{solvent}(t - t^*) + \rho_{HGS}t^*)/t \quad 25$$

To validate this method three different solvent and HGS combinations are used. In the first case the solvent is represented by acrylic sheets (1.18 g/cm<sup>3</sup>) and the HGS by aluminum sheets (2.6 g/cm<sup>3</sup>). In the second case the solvent is represented by aluminum sheets and the HGS by titanium sheets (4.506 g/cm<sup>3</sup>). In the third case the solvent is represented by acrylic sheets and the HGS by titanium sheets. A source voltage of 175 kV and a source current of 85  $\mu$ A was used for all experiments. The  $t$  values of 63.5 mm, 25.4 mm, and 25.4 mm were used for the acrylic/aluminum, aluminum/titanium, and acrylic/titanium combinations respectively. The  $t$  value of 63.5 mm and 24.5 mm represent the maximum thickness of aluminum and titanium that can be radiographed at the source voltage of 175 kV and source current of 85  $\mu$ A. The  $\mu^*$  vs  $t - t^*$  curves for cases 1, 2, and 3 are shown in Figure 25, Figure 26, and Figure 27 respectively. Errors of less than 1% were observed when the interpolated value of  $\mu^*$  was used to estimate density. The points (i.e. values of  $t - t^*$ ) at which the  $\mu^*$  were interpolated and the corresponding error in measuring density at those points are shown in Table 5.

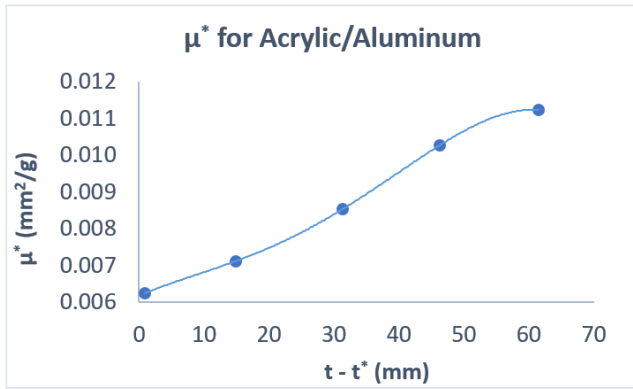


Figure 25-  $\mu^*$  vs  $t - t^*$  curve for acrylic and aluminum combination

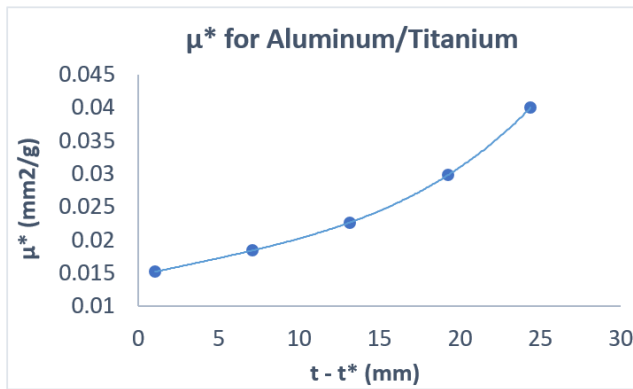


Figure 26-  $\mu^*$  vs  $t - t^*$  curve for aluminum and titanium combination

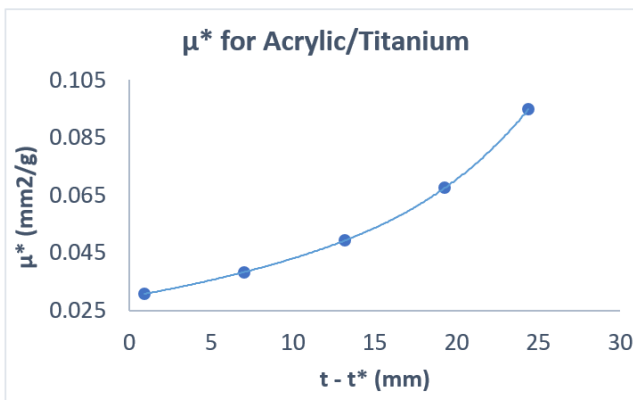


Figure 27-  $\mu^*$  vs  $t - t^*$  curve for acrylic and titanium combination

Table 5- Density estimation errors using Method #2

Acrylic/Aluminum		Aluminum/Titanium		Acrylic/Titanium	
t-t* (mm)	% Error	t-t* (mm)	% Error	t-t* (mm)	% Error
7.2	0.98	4.0	-0.77	4.0	-0.42
22.3	0.65	10.2	0.02	10.1	-0.07
38.9	0.84	16.3	0.16	16.2	0.30
55.7	0.89	22.4	0.02	22.3	0.81

#### 2.6.4 ACCOUNTING FOR EFFECTS OF TEMPERATURE, PRESSURE AND AERATION

In the field environment of actual drilling rigs, temperatures can vary by as much as 122 °F, and pressures by 7500 psig as compared to laboratory settings. Furthermore, mud aeration in the mud pits can be as high as 14% (Nickles et al, 1972). Effects of these variations on mud density and the relevant techniques to account for the effects using X-rays are addressed in the following sub-sections.

##### 2.6.4.1 Effect of Temperature and Pressure on $\mu_m$

The mass attenuation coefficient is not a function of material density and is therefore not affected by pressure. Temperature on the other hand has been shown to have an effect on  $\mu_m$  (Meibohm et al., 2017). Read et al., (1926) observed that  $\mu_m$  increased by about 0.2% for every 100 °C increase in temperature. Since field temperature variations from STP are not expected to exceed  $\pm 50$  °C,  $\mu_m$  dependence on temperature is expected to be less than 0.2% and can be ignored.

#### 2.6.4.2 Accounting for Temperature and Pressure Variations

In Equation 4, changes in pressure and temperature affect the material density and thus the overall attenuation by a given material. The density of water at 32 °F decreases by 2.7% when pressure is increased from 0 psi to 8000 psi. Similarly, density of water at 0 psi decreases by 1.2% when temperature is reduced from 122 °F to 32 °F (Kell et al., 1965). The density of a 11 ppg diesel based mud at 78 °F can decrease by 2.8% when pressure is increased from 0 psi to 9000 psi. Similarly, the density of a 11 ppg diesel based mud at 0 psi can decrease by 4.6% when temperature is reduced from 200 °F to 78 °F (Peters et al., 1990). To account for the pressure and temperature changes in the empirical method, the density and corresponding GLV values in the lookup tables can be updated based on real time data from the pressure and temperature transducers in the rig standpipe. A similar adjustment in the model-based method #1 and #2 can be made to the density and corresponding GLV values of the original muds. The updated density value ( $\rho_{final}$ ) is calculated by applying the relevant coefficients of compressibility and thermal expansion to the initial density value ( $\rho_{initial}$ ). The updated GLV ( $I_{final}$ ) is calculated from the initial GLV ( $I_{initial}$ ) by using Equation 26, which is derived using the Beer Lambert's law.

$$I_{final} = \exp\left(\left(\frac{\rho_{final}}{\rho_{initial}}\right) \ln\left(\frac{I_{initial}}{I_0}\right) + \ln(I_0)\right) \quad 26$$

### 2.6.4.3 Accounting for Mud Aeration

The volume of entrained air in the mud pits can be determined by measuring the difference in density values collected by using a pressurized mud balance (which has a standard operating pressure of 250 psig) and a non-pressurized mud balance. Two worst case scenarios for air entrainment are considered. In the first scenario, 14% air entrainment is already present in the mud pits when the manual density measurements are made. In the second scenario, 14% air entrainment is encountered at a future point in time during the drilling process. At SPP greater than 120 psi for the first scenario and at SPP greater than 220 psi for the second scenario, 14% air entrainment can cause the true density in the standpipe to vary by 1% (based on ideal gas law calculations) than that measured by the x-ray sensor. If it is known that the mud is heavily aerated, this 1% error can be minimized by measuring the air content and factoring in the effects of air compressibility. To account for the effects of air entrainment the internal pipe diameter ( $t$ ) is updated to  $t_{\text{new}}$  (cm) using Equation 27.

$$t_{\text{new}} = t - t_{\text{air}} \quad 27$$

where  $t_{\text{air}}$  (cm) is the real-time proportion of air in the standpipe and  $t_{\text{new}}$  is the updated pipe diameter.

The reference GLV values in the empirical method, model based method #2, and the GLV values of the original muds in the model-based method #1 are then updated using Equation 28, which is derived using the Beer Lambert's law.

$$I_{final} = \exp\left(\left(\frac{t_{new}}{t}\right) \ln\left(\frac{I_{initial}}{I_0}\right) + \ln(I_0)\right) \quad 28$$

It is noted that the drilling fluid mass attenuation coefficient at  $t_{new}$  is different from that at  $t$ . This change in the mass attenuation coefficient value is denoted by  $\Delta\mu_m$ . In formulating Equation 28, it was assumed that  $\Delta\mu_m \ll \mu_{air}$ .

## 2.7 Conclusion

It has been shown that it is possible to measure drilling mud density with an accuracy of 99% or better using polychromatic x-rays. This work provides a completely new method for density measurement of well construction fluids used in drilling and other industries. The method can provide real-time high frequency density measurements in high pressure lines (>7500 psi) and normal lines without using a radioactive source and with significantly improved performance. It is meant as a substitute for gamma ray meters, for conditions that preclude their use. Three approaches for density measurement are discussed, with each offering application specific benefits. The x-ray measurement method enables a step-change improvement in the safe drilling of complex wells with narrow drilling windows, by facilitating better estimation of the density and pressure profile of the primary barrier in the well bore.

## 3 VFR MEASUREMENT USING X-RAYS

### 3.1 Introduction

In regards to flow measurement, we are not familiar with any studies that have employed X-rays to measure fluid velocities in high speed industrial applications. An example of such an application is drilling mud flowing through a rig standpipe with pressure and velocities reaching 7500psig and 30 ft/s respectively. Most X-ray velocity measurement studies to date have focused on estimating flow rates at near atmospheric pressures, for low fluid velocities (less than 75 mm/s, Kertzsch et al., 2004, Heindel et al., 2008, Santiago et al., 1998, Lee et al., 2003, Im et al., 2007). The velocity measurements in these studies were made using high speed imaging techniques such as X-ray particle induced velocimetry (XPIV) which is used for highly seeded fluids or X-ray particle tracking velocimetry (XPTV) which is used for lightly seeded fluids. It is noted that the equipment required for XPIV and XPTV such as a high speed camera, an image intensifier, synchronization equipment, and circuitry can be expensive and complex (Lee et al., 2003).

Work was conducted to develop an algorithm which can use images collected by the XPTV method to measure velocity of drilling fluids. The algorithm measures VFR by measuring the displacement of tracer particles, using images collected at different time intervals. The drilling fluids are either intentionally seeded with tracer particles for purposes of flow measurement or contain moving features which can be captured using XPTV. The algorithm was used to calculate the velocity of an aerated fluid flowing through

a pipe, by using the air bubbles as the tracer particles. The flow was imaged at 30 fps using a digital camera. Performance results of the algorithm are shared.

In addition to of high speed imaging of tracer particles, two additional methods to measure VFR are also explored and are currently under development. The methods use standard X-ray equipment unlike the expensive and complex setup required for the high speed imaging method. The first method estimates VFR by measuring the lengths of paths traced by the seeded particles on a ‘single radiograph’, as opposed to using multiple images required in high speed imaging method. The second method estimates VFR by using X-rays to measure the change in the displacement of spring loaded pistons which deflect due to the fluid flowing through the pipe. The piston deflection which is directly proportional to the mass flow rate of the fluid can then be used to infer the velocity of a fluid with known density.

### **3.2 Measuring VFR using High Speed X-ray Imaging Equipment and Tracer Particles**

An algorithm was developed to estimate fluid velocity from the captured 2D images of tracer particles. The algorithm uses block matching to determine the motion (defined using motion vectors) of tracer particles between two images of fluid flow. If the time difference between the images is known, then this relative motion information can be used to compute the velocity of tracer particles. Block matching was performed using an Advanced Rood Pattern Search (ARPS) described in detail by Barjatya et al., (2004). In comparison to other motion vector extraction techniques such as diamond search, 4-step

search, etc., ARPS performs faster as it requires a smaller number of calculations (Barjatya et al., 2004).

To implement block matching, the reference frame was divided into blocks (4x4 pixels in size) as shown schematically in Figure 28. The best match for each block was then located in the current frame using ARPS with an initial search area size of 7 pixels.

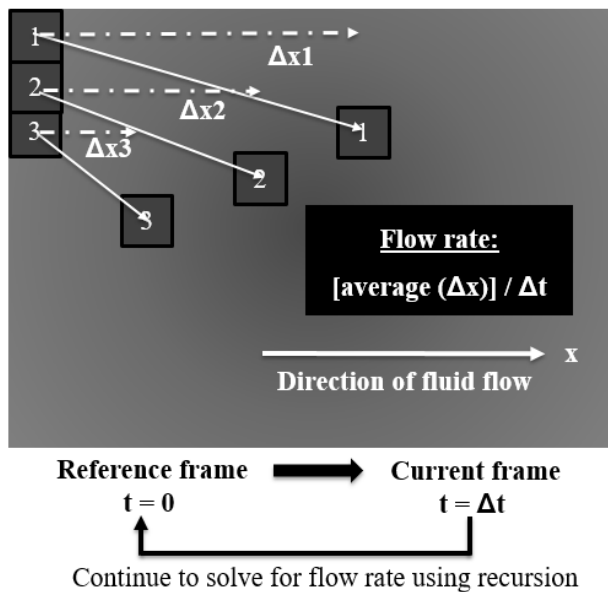


Figure 28- Schematic representation of the block matching technique (Note: Figure is used for explanation purposes only and is not to scale).

Displacement/Motion vectors were then computed between the matching elements. Motion vectors with non-zero values represent areas where motion was detected. The components of these vectors, parallel to the pipe wall, were averaged over each frame in order to compute the average displacement (denoted by pixels per frame) in the direction of fluid flow. This average displacement was then divided by the frame rate to compute

the average fluid velocity in pixels per second. To compute the velocity in m/sec the velocity in pixels per second was multiplied by the length of pipe contained in the image.

Preliminary validation of the algorithm was conducted using a video, at 30 frames per second, of a fluid flowing through a transparent pipe and containing entrained air bubbles as tracers. A single representative frame of fluid flow through this pipe is shown in Figure 29.

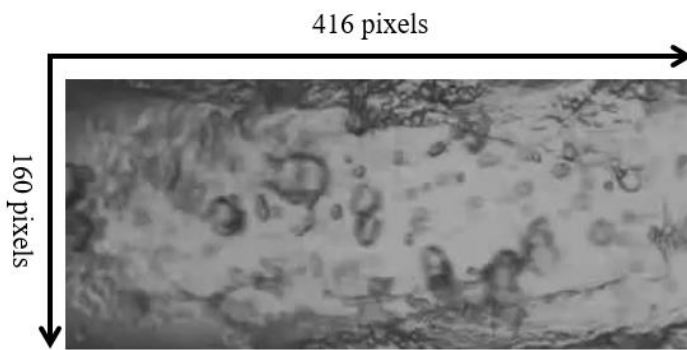


Figure 29- Image of fluid-flow used for preliminary testing.

An example of motion vectors calculated for an image section are shown in Figure 30, where the size of the arrow is proportional to the quantity of motion detected.

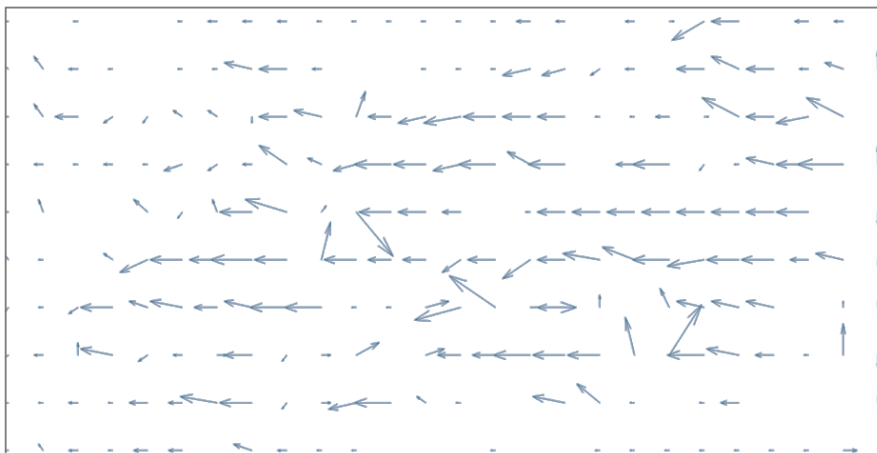


Figure 30- Example of calculated motion vectors for an image section (Note: not for the same image as used in Figure 29).

Displacement for the aerated flow was calculated to be 7 pixels/frame or 210 pixels/second. For a 1 ft pipe section with 2-inch inner diameter, this would equate to 5 gpm. Visual inspection and a timer were used to confirm the velocity measurements calculated with the algorithm, and were found to be in good agreement with each other.

### **Data Filtering using Gaussian Filters**

The motion vectors generated using ARPS detect all types of motion. The algorithm can be further refined to eliminate motion from unwanted artifacts, based on their contrast, size and shape. One way to achieve size and shape based filtering using the Hough transform. The Hough transform is very effective in locating objects with a predetermined parametric model, for example spherical tracers. Object shapes that do not follow such a model can also be detected by introducing a variance in the model. It is noted that Hough transforms are however computationally expensive and similar to Canny edge maps are not good at detected faint edges. A relatively faster method for artefact detection is using a Gaussian filter. These filters allow for contrast and size based filtering that can be achieved by convolving each image with a properly designed Laplacian of Gaussian (LoG) or a Difference of Gaussian (DoG) filter as shown in Figure 31. The Log/DoG filters are derivative filters that are used to find areas of rapid change such as edges or luminance change in images. Since the Laplacian and Derivative filters when used by themselves are very sensitive to noise, a Gaussian filter is typically used to smooth the image prior to their implementation. This two-step process is called a LoG/DoG operation.

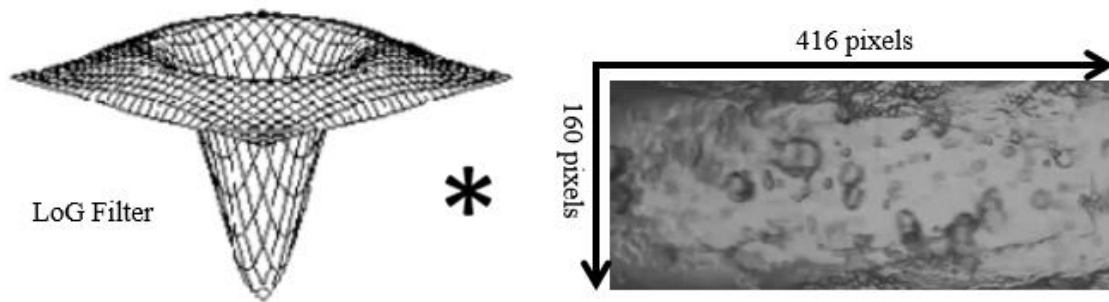


Figure 31- Convolution of an image with a LoG filter.

The surface plot that results from the convolution of an image frame with a LoG filter is shown in Figure 32.

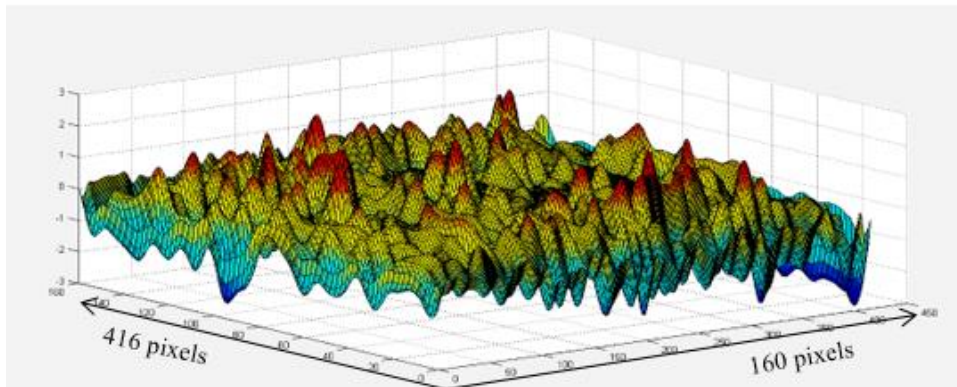


Figure 32- Surface plot of an image convolved with a LoG filter (Note: not for the same image as used in Figure 31).

The peaks in Figure 32 represent the coordinates of the detected artifacts. The higher peaks represent areas of greater contrast (in this case more distinct bubbles) as compared to their surroundings. The detected artifacts are circled in red as shown in Figure 33.

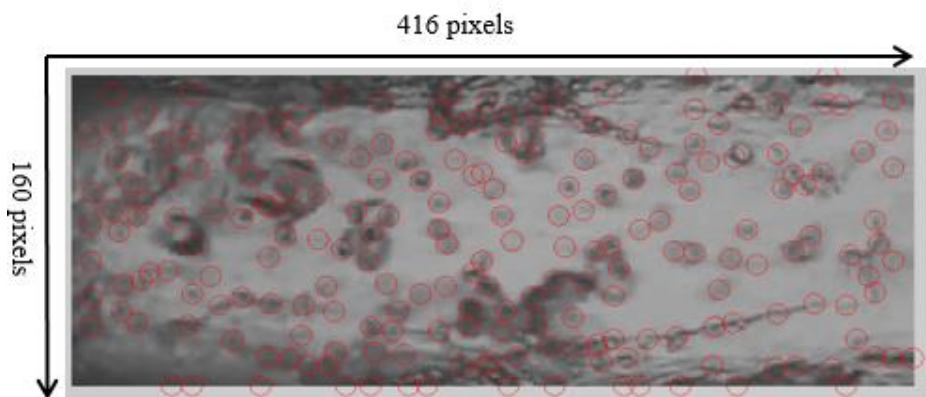


Figure 33- Artifacts detected by the LoG filter.

Further filtering can be performed by applying a threshold to the surface plot in Figure 32 such that artifacts below a certain luminance value can be eliminated. Results from such filtering are shown in Figure 34.

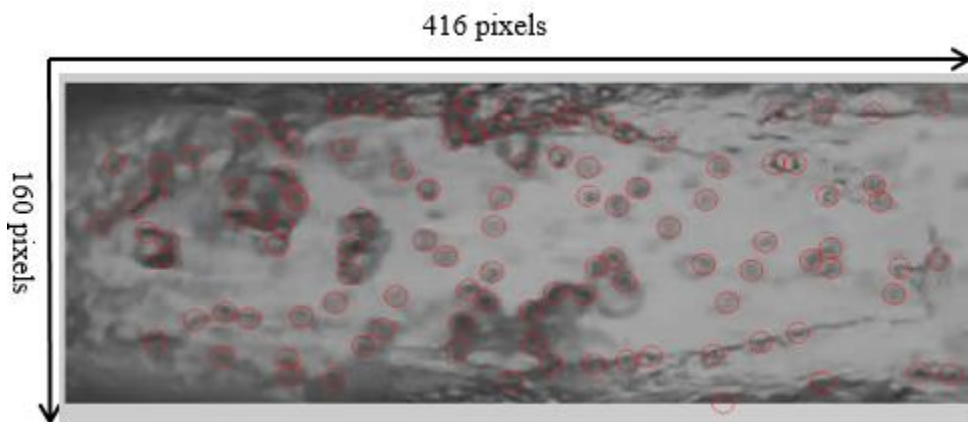


Figure 34- Filtered artifacts after applying a luminance threshold

Once the desired artifacts have been isolated, motion vector information at the coordinates of these artifacts can be used to calculate fluid velocity.

To improve visualization, the artifacts of interest can also be colored or binarized.

The colored and binarized artifacts from two dissimilar images are shown in Figure 35.

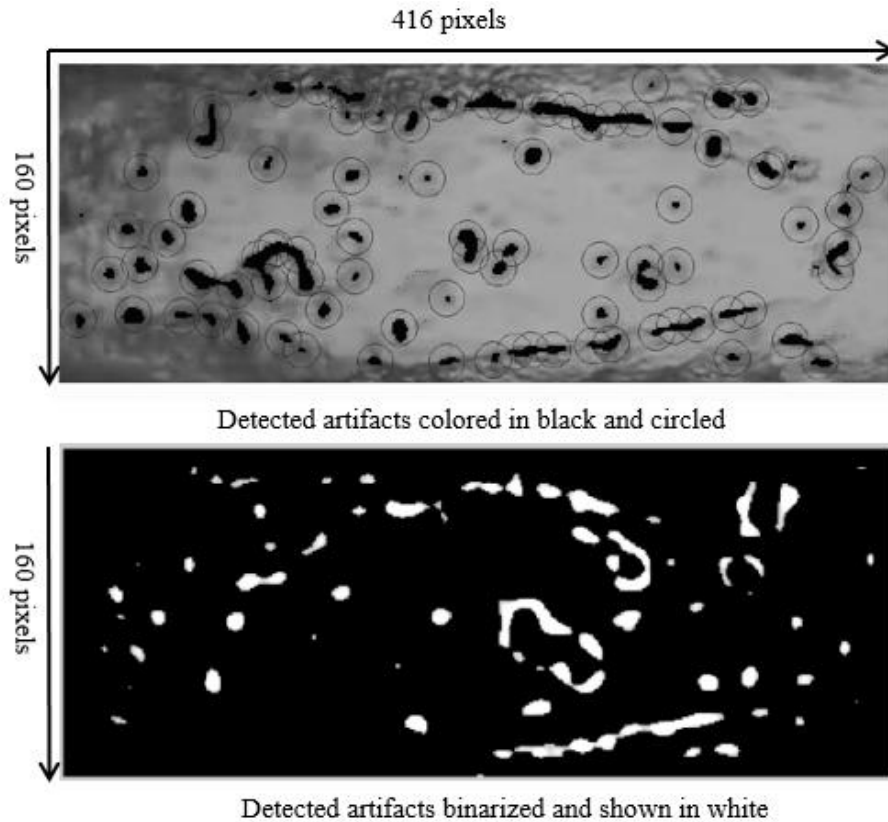


Figure 35- Colored and Binarized artifacts extracted from two random images in the video sequence.

Future experiments at flow rates between 0-40 gpm in a 2-inch diameter pipe are planned for a more robust evaluation of this technique. The experiments will be conducted with different tracer particles and flow velocity will be verified using a Coriolis meter. A flow-loop has been constructed to carry out these experiments and is shown in Figure 36.

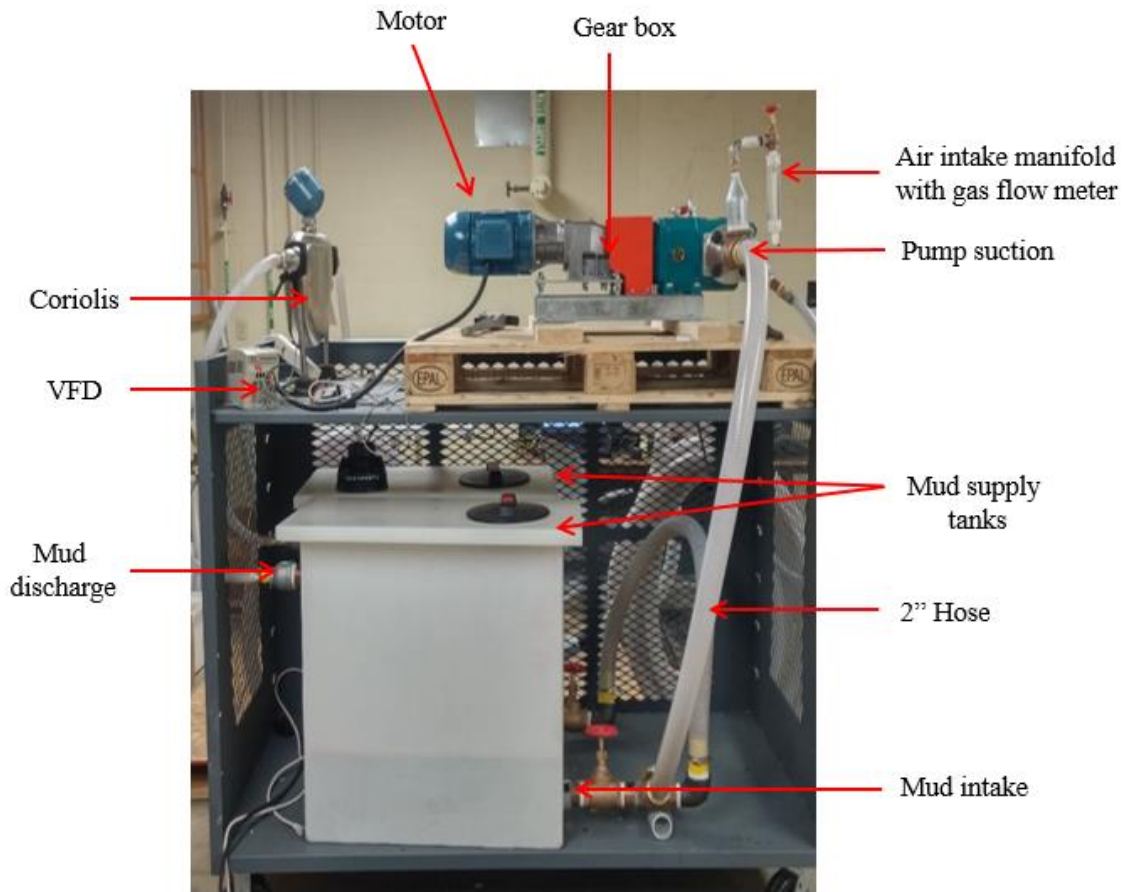


Figure 36- Test flow loop for high speed imaging experiments.

### 3.3 Measuring VFR using a Flat Panel Detector and Tracer Particles

In this method fluid velocity is estimated by multiplying the mean displacement (parallel to the pipe wall) of tracer particles in an X-ray radiograph by its capture rate (fps). The radiograph of tracer particles collected at 60 fps is schematically shown in Figure 37. The velocity of the fluid can be estimated by averaging  $\Delta x_1$  thru  $\Delta x_4$  and subsequently multiplying by the frame rate of 60.

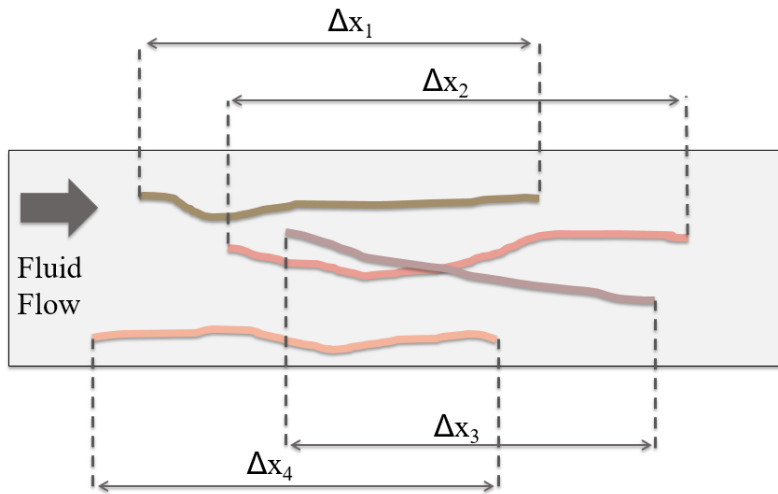


Figure 37- Schematic of tracer tracks captured in radiographs.

To test the capability of standard industrial X-ray systems to image the high speed tracers, tungsten carbide ( $15.3 \text{ g/cm}^3$ ) beads as shown in Figure 38b were embedded in an acrylic rod spinning at 550 rpm.

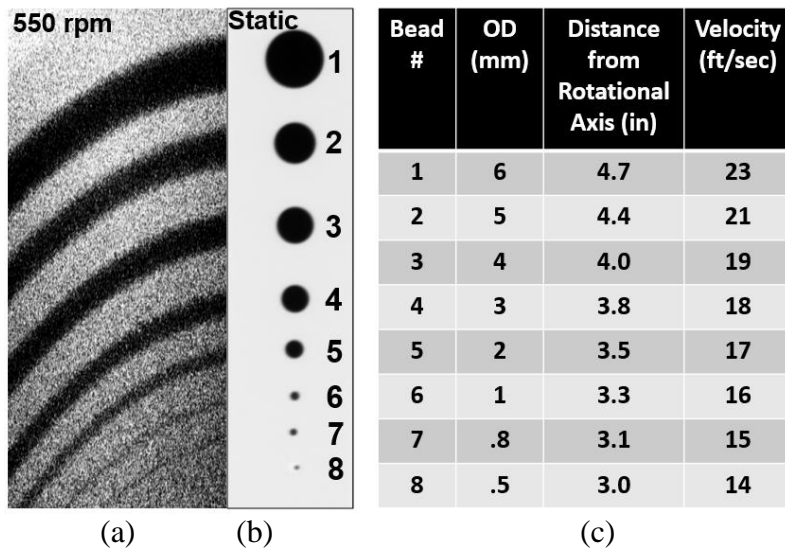


Figure 38- (a) Radiograph of moving tracers (b) Radiograph of static tracers (c) Tracer test matrix.

The beads were embedded in increasing diameters away from the center of rotation of the rod. The bead sizes used for this experiment and their respective velocities are shown in Figure 38c. Radiographs of the moving beads were collected using a flat panel detector at a source voltage of 200 kV and a source power of 460 W. Figure 38a shows the images were obtained with good contrast for bead numbers 1 through 5. The experiment demonstrates that the X-ray detectors are capable of detecting tracer particles, 6 mm (0.23 inch) in size, travelling at pipe velocities of 7 m/s (23 ft/sec).

Work is underway to characterize suitable tracer particles that can be radiographed with good contrast, when entrained in drilling fluids in the 8-20 ppg range. To conduct this experiment the same basic setup as shown in Figure 38 can be used. The seeded drilling fluid in this experiment can be simulated by placing a 4-inch wide plastic bottle, filled with the drilling fluid, in between the rotating rod and the source. Work is also underway to identify suitable object tracking techniques that can be used to measure the mean displacement of the tracer particles from their radiographs.

### **3.4 Measuring Volumetric Flow Rate using the Piston Mechanism**

This method uses X-rays to measure the change in displacement of spring loaded pistons that deflect under the influence of the fluid flowing through the pipe. The change in piston displacement is directly proportional to the area of piston perpendicular to fluid flow, the drag coefficient between the piston and the fluid, the spring constant, the fluid density, and the unknown fluid velocity. This relationship can be used to solve for the unknown fluid velocity based on the piston displacement information provided by the X-

ray sensor. To determine the amount of piston displacement, the pistons are placed in the path of X-rays, i.e. between the X-ray source and the X-ray detector. Upon deflection, the pistons cause the intensity of the X-rays incident on the detector to change. This change in intensity along with the known physical and geometric properties of sensor components can be used to calculate the piston displacement, which can then be used to calculate fluid velocity. A schematic of the flow rate measurement system is shown in Figure 39

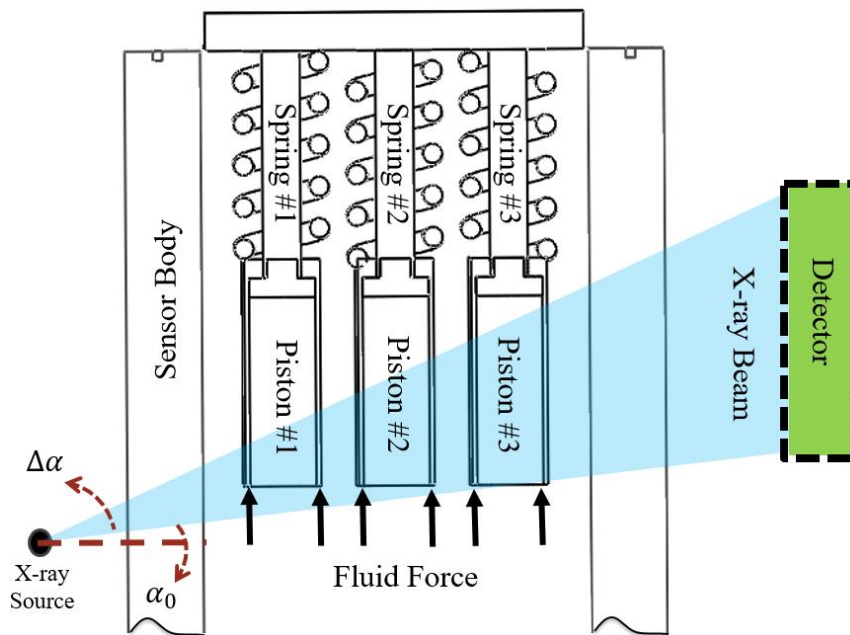


Figure 39: Schematic of piston mechanism.

Based on sensor and piston geometry, it is determined that the piston closest to the source only attenuates X-rays for the first 1.5 inches of total deflection, the piston in the middle attenuates X-rays for the first 2.5 inches of total deflection, and the piston closest to the detector attenuates X-rays for the first 3.5 inches of total deflection. Experiments have shown that piston deflections of 1 mm can be detected by the X-ray detectors when

the working fluid is water and piston material is acrylic (1.18 SG). However, if the density contrast between the working fluid and piston material is increased, as in water and aluminum (2.6 SG) for example, deflections smaller than 0.5 mm can be detected. Using this information and by selecting the appropriate spring constants for the 3 springs, a flow resolution of 6.5 gpm can be achieved using the flowrate mechanism, for a maximum rated flow of 1200 gpm. This allows flows to be measured with greater than 99% accuracy for flow rates above 650 gpm, 98% accuracy for flow rates between 325 and 650 gpm, 97% accuracy for flow rates between 217 and 325 gpm, 96% accuracy for flow rates between 166 and 217 gpm, and 95% accuracy for flow rates between 130 and 166 gpm.

The piston deflection can be modeled by:

$$x_i = \frac{1}{k_i} \left( -W_p + \frac{c_d * A * \rho_{fluid} * v^2}{2} \right), i = \{1,2,3\} \quad 29$$

where:

k = Spring constant (N/cm)

x = Deflection of piston (cm)

W<sub>p</sub> = Weight of piston (N)

c<sub>d</sub> = Drag coefficient for the piston (unitless)

A = Area of piston perpendicular to the direction of fluid flow (cm<sup>2</sup>)

v = Fluid velocity (cm/sec)

ρ<sub>fluid</sub> = Fluid density (g/cm<sup>3</sup>)

If the drag coefficient, which is function of Reynolds number, is known, there are two remaining unknowns in Equation 29, i.e. the piston deflection and the fluid velocity. A second equation where the GLV at the detector is proportional to piston deflection can be written using the Beer Lambert's law. This equation along with Equation 29 can be used to solve for fluid velocity, provided  $\mu_m$  values of the fluid-piston matrix (upon deflection) are known at the various pixels along the detector.

Work is underway to characterize the drag coefficient values for different types of drilling fluids, and to determine the  $\mu_m$  values of two-component mixtures (representative of the piston-drilling fluid matrix) irrespective of the depth of the mixture or the relative proportions of the two components in the mixture. Flow tests using the test flow loop shown in Figure 40 are also being planned to further develop and test the accuracy of the piston deflection technique to measure VFR.

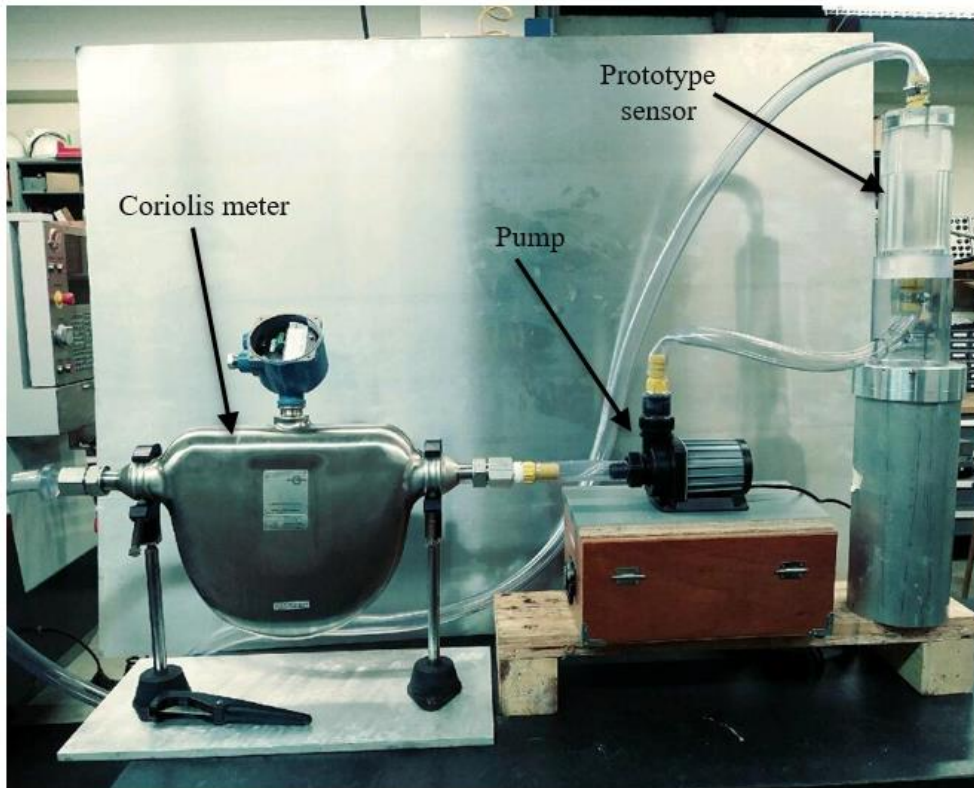


Figure 40- Test flow loop for conducting experiments using the piston mechanism.

### 3.5 Conclusion

Real-time VFR measurement of industrial fluids using X-rays is a relatively novel area of research. Most X-ray velocity measurement studies to date have focused on estimating flow rates for low fluid velocities (less than 75 mm/s) using the XPIV and XPTV high speed imaging techniques. Here, three methods for measuring VFR of high velocity (up to 9000 mm/sec) industrial fluids using X-rays have been proposed. The first method builds upon the existing XPIV and XPTV high speed imaging techniques and the other two methods utilize standard industrial X-ray equipment to make the measurements.

For the first method, an algorithm was developed in order to extract velocity information from high speed images of a flowing fluid containing tracer particles. It showed good performance when it was used to estimate the VFR of aerated fluid flowing through a transparent pipe. For the second method, experiments showed that standard industrial flat panel detectors could be used to radiograph the paths traced by particles entrained in a fluid and traveling at velocities of up to 23 ft./sec. Software can now be written to extract velocity information from these radiographs by employing common image processing algorithms used for object tracking. For the third method, which uses X-ray images of a piston mechanism to estimate VFR, designs of the piston mechanism along with requisite materials needed for construction have been completed. A prototype sensor has been built and assembled into a flow loop which will be used for further research and development of this technique.

Preliminary research work presented in this dissertation shows that X-ray velocimetry shows considerable promise in measuring VFR of drilling fluids flowing through high pressure lines.

## 4 SENSOR DESIGN

### 4.1 Introduction

The X-ray sensor is designed to be inserted as a spool piece between a section of the 4" standpipe. It is designed to measure the density of drilling fluids in the 8 ppg to 20 ppg range and with flow rates of up to 1200 gpm. These measurements are made using a polychromatic X-ray source, with a source voltage and current that is well within the range of readily available industrial X-ray tubes. In the past such measurements would require X-ray voltages that could only be achieved with linear accelerators thereby making the cost and size of equipment non-conducive to the drilling environment. However, recent advances in pipe manufacturing, particularly using a class of low density and high pressure materials known as carbon fiber reinforced polymers (CRPs) and, are now making it viable to re-visit relatively low cost X-rays systems for density and mass flowrate measurements. Windows constructed from CRPs allow us to bypass the high density carbon steel standpipe and make measurements at voltages that do not require a linear accelerator.

CRPs have been extensively used in the aerospace industry for quite some time (Soutis, 2005) and have recently gained interest from the oil and gas industry, specifically for use in offshore marine riser applications (Pham et al., 2016 Wang et al., 2015, Mahieux et al., 2001). CRPs contain carbon fibers that are attached to a thermosetting (epoxy, polyester, phenolic, polyimide resins) or thermoplastic (polypropylene, polyvinylidene fluoride, Nylon 6.6, PMMA, PEEK) polymer matrix (Soutis, 2005). Depending upon the choice of polymer matrix, the density of these composites can vary between 1.3–2 gm/cm<sup>3</sup>

(Windhorst et al., 1997) and temperature capabilities can be as high as 120 °C (Soutis, 2005). Some of these composites (PEEK based for example) demonstrate high wear resistance and low friction coefficients which in many cases makes them a better substitute than steel for handling abrasive fluids (Ji et al., 2015, Voss et al., 1987, Burris et al., 2008, Zhang 1998, Friedrich et al., 1995). Furthermore, the wall thickness to pressure handling capabilities of some CRP pipes is also comparable to that of steel. These characteristics of CRP pipes makes them a good substitute for steel when transporting drilling fluids.

The CRP pipes are also lined with a replaceable low density liner material to prevent damage from the abrasive drilling mud slurry. The options for low density liner materials compatible with hydrocarbon applications, include elastomers such as polyurethane and neoprene and plastics such as ultra-high molecular weight polyethylenes (Xie et al., 2015). Natural rubber is also a good option if hydrocarbons are not expected to be mixed with the drilling mud (Sare et al., 2001, Iwai et al., 1997, Hocke et al., 1978). Amongst these liner materials, polyurethane in particular stands out since it has already received a lot of attention by the oil and gas industry for its resistance to corrosion and abrasion (Ashrafizadeh et al., 2017).

This section focuses on the design and implementation of a CRP based X-ray sensor that is used to measure drilling mud density and mass flowrate at the high pressure well inlet. Details are also provided on the proper selection and sizing of the associated X-ray components.

## 4.2 Sensor Mechanical Design

The x-ray sensor consists of a steel casing (6" ID x 8" OD x 12" H) with cut-out windows at the source and detector mounting locations. These windows allow for the X-rays to travel through the sensor without encountering any steel (Figure 41a,b). A CRP pipe (4.5" ID x 6" OD x 12" H) and a replaceable liner (4" ID x 4.5" OD x 12" H) are assembled into the casing using a clearance-fit (Figure 41b).

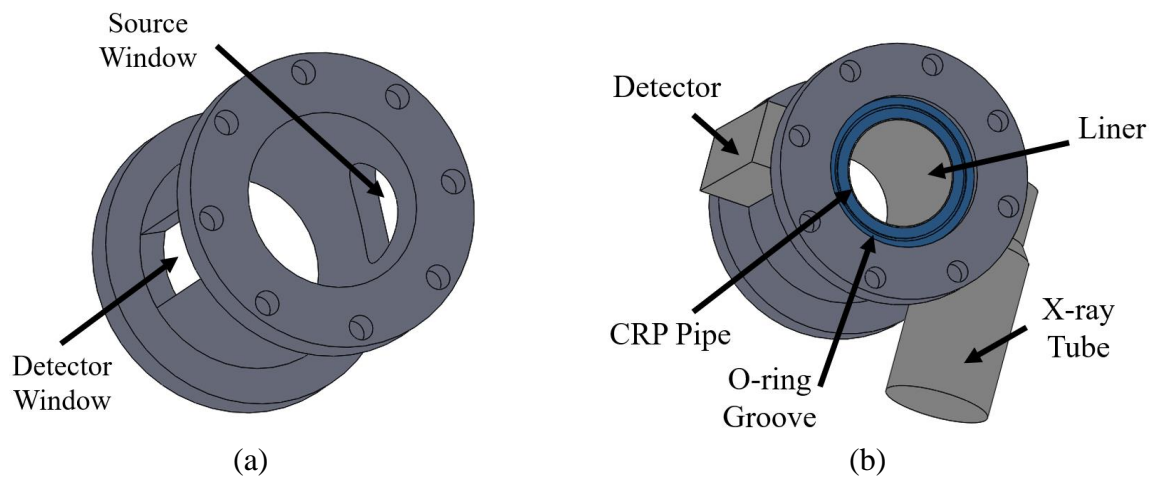


Figure 41- (a) API rated steel casing. (b) Source, detector and polymer pipe assembled onto casing

A flanged steel endcap (4" ID x 8" OD x 6" H) is then connected to both ends of the casing. The endcaps help to connect the sensor to the standpipe and are also used to provide a pressure tight connection between the casing and the CRP pipe, by using an O-ring seal (Figure 42a). An alternative option to the endcap and O-ring seal design is to use

end fittings that are offered by some manufacturers specifically for their CRP pipe designs. The complete sensor assembly is shown in (Figure 42b). Not shown in the sensor assembly is the 0.6-inch thick lead shielding (Singer et al., 1947) that is necessary to protect rig personnel from the undesirable effects of X-ray radiation.

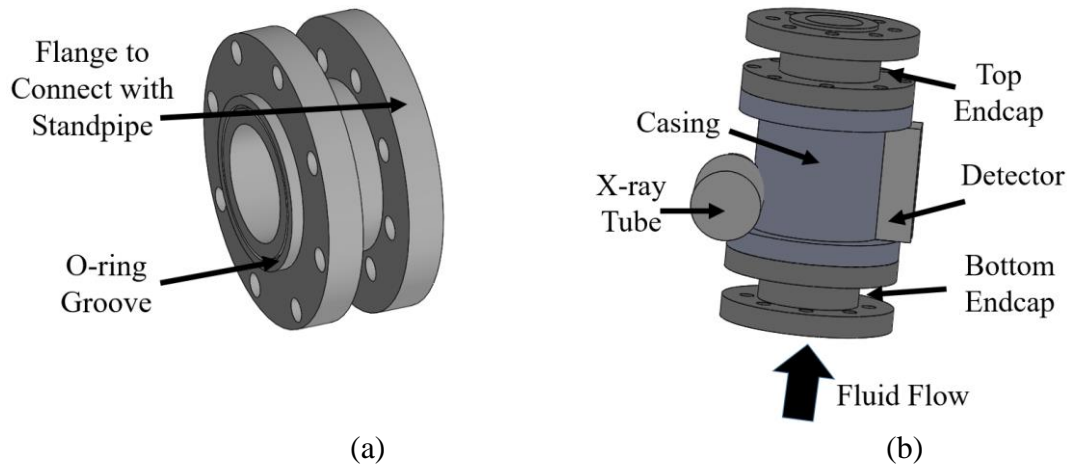


Figure 42- (a) Endcap design. (b) Complete sensor assembly.

The internal components of the sensor contain a mechanism to implement real-time calibration of the x-ray detectors and a piston mechanism to measure fluid velocity. It is noted that the sensor should be used without the piston mechanism when using tracer particles to measure VFR. Both these mechanisms are welded to the bottom and top endcaps respectively. The calibration mechanism (Figure 43a,b) consists of a one-piece polyurethane (1.2 gm/cm<sup>3</sup>) conical calibration rod and a support post. At the end of the polyurethane rod a second calibration material made from tungsten carbide (15.63 gm/cm<sup>3</sup>) is assembled using a clearance fit. A hardened steel bracket, which can be welded to the end cap, is then connected to the support post. The calibration rods are concentric

with the X-ray source and are 4-inches long such that their ends form a tight seal with the liner.

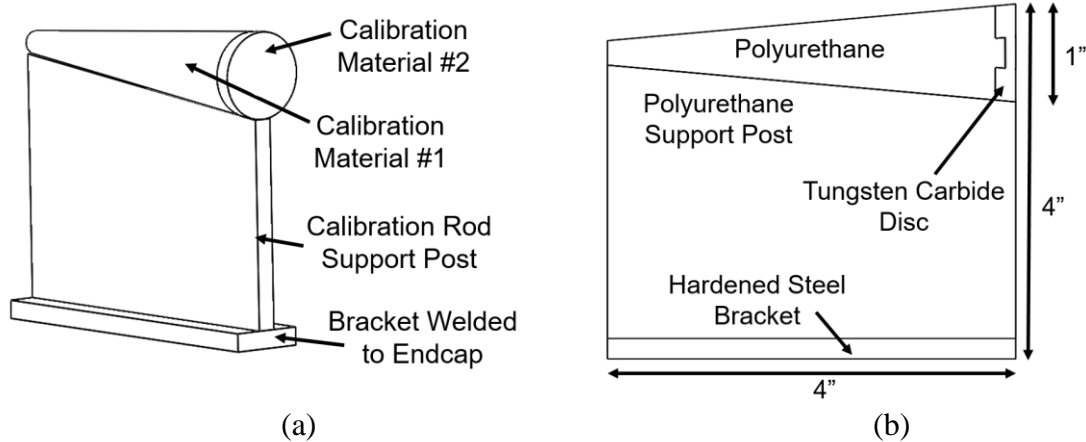


Figure 43: (a) X-ray calibration mechanism isometric view (b) X-ray calibration mechanism cross-sectional view.

The flow rate mechanism (Figure 44) consists of 3 identical pistons connected to tungsten carbide springs of different spring constants. The pistons are constructed from polyurethane and are embedded with a 0.2” steel plate (8 gm/cm<sup>3</sup>) that provides the X-ray attenuation. The equivalent density of the polyurethane/steel piston matrix is 2.6 gm/cm<sup>3</sup>. The allowable deflection for each piston is 3.5-inches. The pistons deflect along the 0.25” diameter tungsten carbide guide posts due to the force exerted by the fluid flow. The guide posts are mounted to a hardened steel bracket, which is welded to the end cap. The amount of piston deflection is measured using X-rays which is then used to infer fluid velocity.

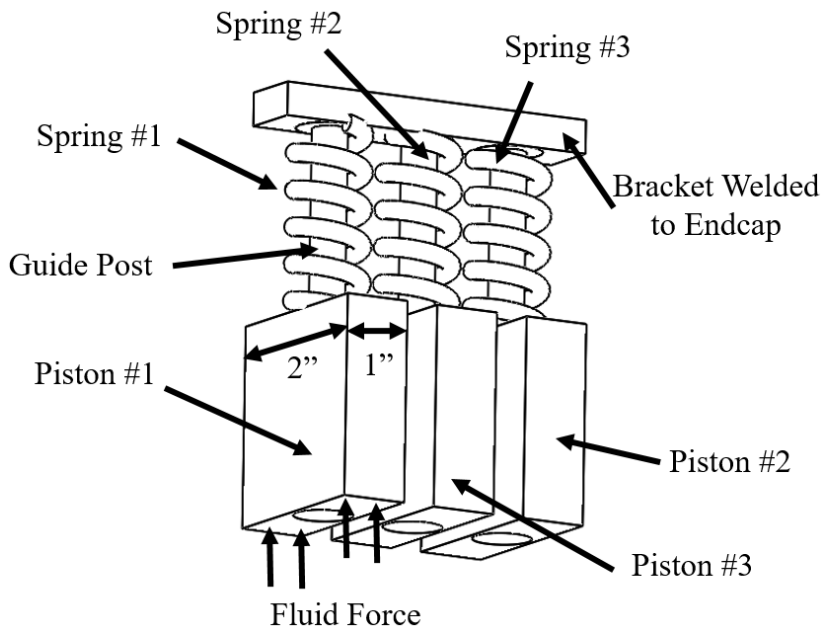


Figure 44: Flow rate mechanism isometric view

A front cross-sectional view of the complete sensor assembly when viewed from the detector side is shown in Figure 45. Also shown enclosed in dotted lines is the region of the sensor that is radiographed by the detector to make the appropriate calibrations and the density and flow rate measurements.

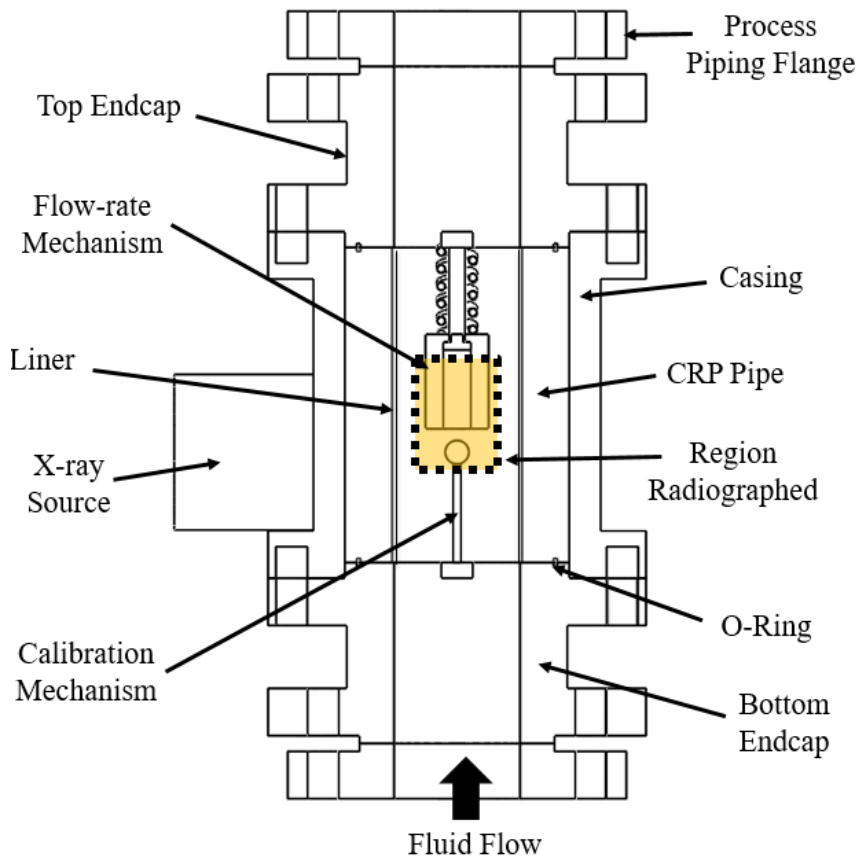


Figure 45- Sensor cross-sectional view from detector side (front view)

A side cross-sectional view of the complete sensor assembly with the radiographed region enclosed in dotted lines is shown in Figure 46.

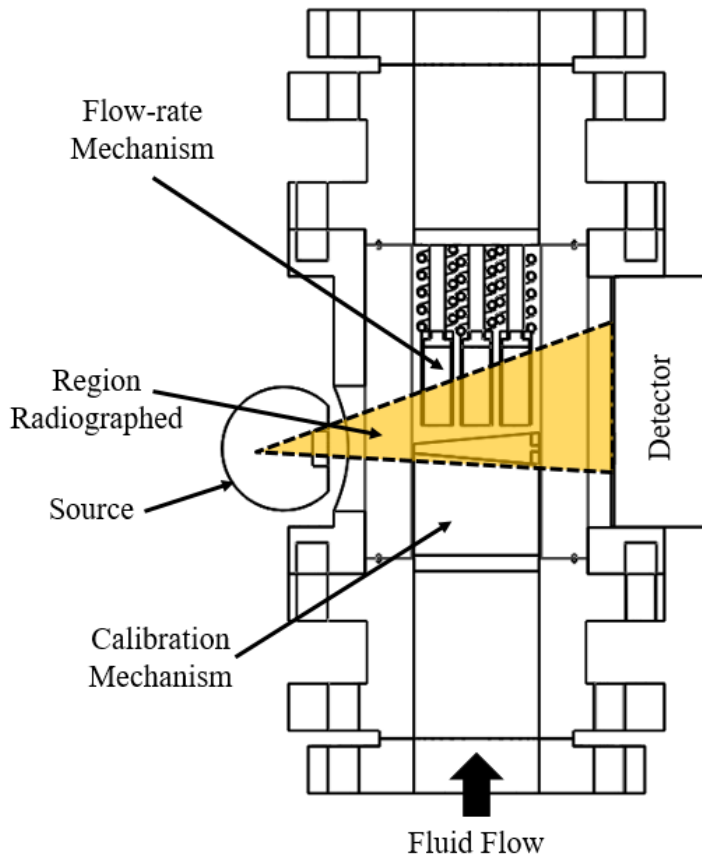


Figure 46- Side cross-sectional view.

A close-up of the front cross-sectional view of the radiographed region is shown in Figure 47. The radiographs are collected at 1 Hz frequency. Different areas on the radiograph/detector referred to as the area for velocity measurements (AVM), area of calibration measurements (ACM), and area for density measurements (ADM) are used to make the respective velocity, calibration and density measurements. These areas are also shown in Figure 47.

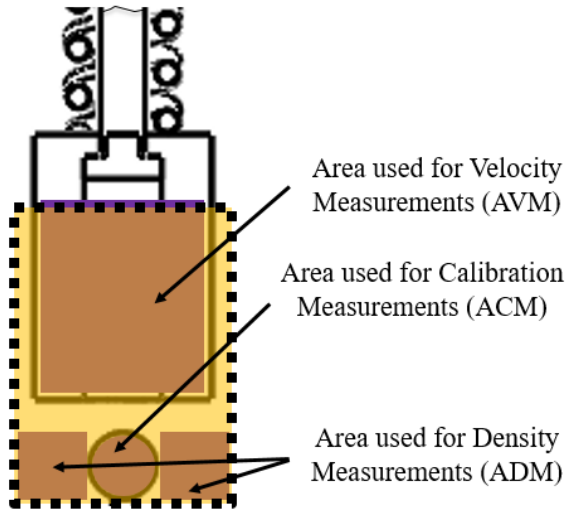


Figure 47- Measurement classification of radiographed region (front view).

A close-up of the side cross-sectional view of the radiographed region along with areas for velocity, calibration and density measurements are shown in Figure 48.

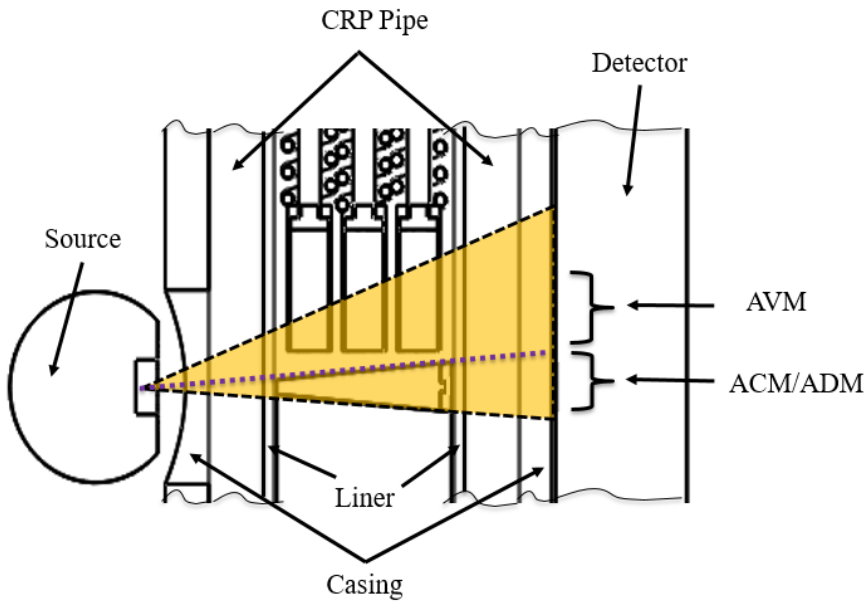


Figure 48- Measurement classification of radiographed region (side view).

A tabulated summary of sensor component dimensions and materials of construction is provided in Table 6 for quick reference.

Table 6: Summary of sensor component dimensions and materials of construction

Chassis	Piston	Spring
<ul style="list-style-type: none"> <li>• Steel</li> <li>• 8"OD/ 6"ID/ 12"H</li> </ul>	<ul style="list-style-type: none"> <li>• Polyurethane lined steel</li> <li>• 2"L x 1"W x 3"H</li> </ul>	<ul style="list-style-type: none"> <li>• Tungsten carbide</li> <li>• 1"OD / 0.5 ID / 3"H</li> </ul>
Liner	Calibration Mechanism	Guide Post
<ul style="list-style-type: none"> <li>• Polyurethane</li> <li>• 4.5"OD / 4"ID</li> </ul>	<ul style="list-style-type: none"> <li>• Polyurethane rod with tungsten carbide insert</li> </ul>	<ul style="list-style-type: none"> <li>• Tungsten carbide</li> <li>• 0.25"OD / 3"H</li> </ul>
Flanged End Fittings	Calibration Mechanism Mount	Internal Welded Components
<ul style="list-style-type: none"> <li>• Hardened steel</li> </ul>	<ul style="list-style-type: none"> <li>• Polyurethane</li> </ul>	<ul style="list-style-type: none"> <li>• Hardened steel</li> </ul>
CRP Pipe	X-ray Detector	X-ray Source
<ul style="list-style-type: none"> <li>• Victrex® PEEK or Kynar® PVDF polymer matrix with Toray® carbon fibers</li> <li>• 6"OD / 4.5"ID</li> </ul>	<ul style="list-style-type: none"> <li>• 16-bit CCD/CMOS flat panel</li> <li>• 8"L x 2"W</li> </ul>	<ul style="list-style-type: none"> <li>• 320 kV @ 1500 Watts</li> <li>• Continuous duty</li> <li>• Polychromatic fan beam</li> <li>• Coverage area 90° x 30°</li> </ul>

A prototype sensor for laboratory validation was built as shown in Figure 49. It was constructed from a 4-inch acrylic pipe with a 2.5-inch internal diameter. The piston material was constructed from aluminum with a steel spring and a steel guide post. The prototype sensor has been integrated into a test flow loop and is shown in Figure 40.



Figure 49: Prototype sensor.

### 4.3 X-ray Source Power Requirements

The maximum distance X-ray photons must travel between the source and detector in the proposed X-ray sensor is approximately 8.5 inches. For the detectors used in this experiment, the gray value for a given pixel with proper calibration can fluctuate by approximately 200 due to loss of signal at the detector. Thus, for a gray value change of greater than 200 at every pixel, it can be stated with a high level of confidence that the resulting change is brought about by the penetrating X-rays. To estimate the minimum X-ray voltage and power required to penetrate the CRP pipe, polyurethane liner, and the 20

ppg mud flowing through the X-ray sensor the following setup was used. The 20 ppg drilling mud along with the sensor components was simulated by an 8.5-inch long plastic pipe filled with a 22 ppg WBM. The WBM was weighted with hematite and 10% by volume concentration of contaminants in the form of OM#4 ball clay. The 22 ppg drilling mud was an appropriate substitute for the CRP pipe, polyurethane liner and the 20 ppg drilling mud because of its relatively higher density and effective atomic number values.

The experiments were conducted by placing the 8.5-inch WBM filled plastic pipe between a CCD flat panel detector and an X-ray source which had a maximum power rating of 1500 W and maximum voltage rating of 450 kV. Based on results from radiographs it was determined that the minimum voltage and power required to achieve X-ray penetration through the X-ray sensor was 320 kV and 1500 W respectively. Experiments also showed that the source power requirement for X-rays to penetrate a fixed sample size increases with decreasing source voltage.

For demonstration, the power verses voltage relationship is shown for a 5-inch plastic pipe filled with a 22 ppg WBM in Figure 50. It can be observed that voltage and power follow an almost linear relationship above a threshold voltage level (125 kV in this case). Below this threshold level the power requirement increases exponentially.

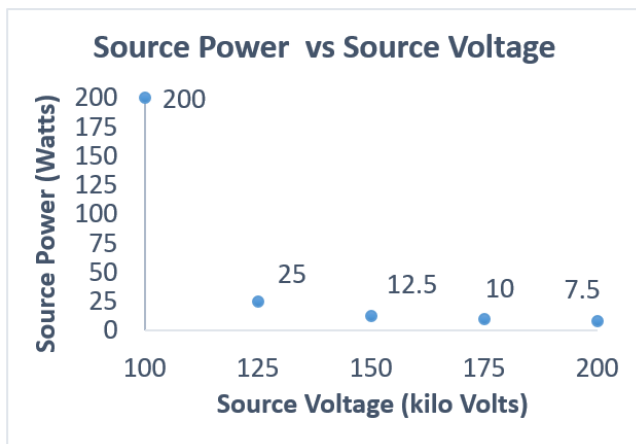


Figure 50- X-ray power required to penetrate a 22 ppg drilling mud in a 5-inch plastic pipe.

The power versus voltage relationship is also shown for a 8-inch plastic pipe filled with a 11.5 ppg WBM in Figure 51. An almost linear relationship between voltage and power was observed for the test range.

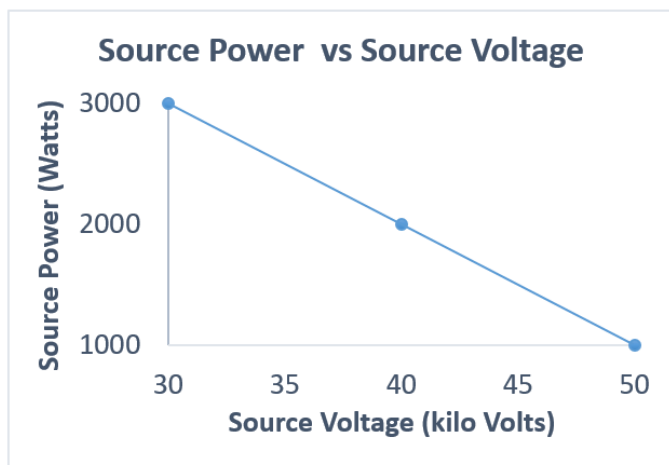


Figure 51- X-ray power required to penetrate a 11.5 ppg drilling mud in a 8-inch plastic pipe.

Knowing the relationship between source voltage and power is helpful because these two parameters directly impact the cost, size, weight and complexity of X-ray equipment. X-ray tube weight and price increases with an increase in the voltage rating. For example, budget pricing by an X-ray tube supplier shows that X-ray tube pricing doubles from \$8,000 to \$16,000 when going from 225 kV to 350 kV (pricing as per the time this dissertation was written). The price again doubles to \$32,000 when selecting a 450 kV tube. It is desirable that the tube power be maximized and tube voltage be minimized to reduce the cost and weight of the X-ray tube. The maximum power rating available for the 225/350/450 kV tubes is 3000/4200/4500 W respectively. Source voltage requirements greater than 450 kV fall outside the scope of standard industrial X-ray systems and are better served by linear accelerators.

It is noted that the 320 kV source voltage is best suited for drilling muds between 15 ppg and 20 ppg. For lighter muds a lower source voltage should be used. This is because the sensor uses a 16-bit flat panel CCD detector with 65,536 gray values to make measurements, and it is not uncommon for the pixels on this detector to saturate at pixel intensities 80-90% of the total dynamic range. Therefore, for all measurements the detector upper gray value threshold is around 55,000 and the lower gray value threshold is around 4,000. In order to remain within the threshold values when making X-ray measurements with 8-15 ppg and 15-20 ppg drilling muds, it becomes necessary to switch the source voltage between a low and a high voltage setting respectively.

## **4.4 X-ray Equipment Selection**

The X-ray system on the sensor consists of two major sub-systems: An X-ray source and an X-ray detector. The X-ray source comprises of an X-ray tube, a generator, a cooler and a controller. Each of these components are now described in greater detail.

### **4.4.1 X-RAY TUBE**

X-ray applications can be classified under five broad categories: applications that require X-ray synchrotrons, applications that require flash X-rays, applications that require linear accelerators, X-ray systems used in medical diagnostics and X-ray systems used in industrial applications. Synchrotrons are typically used to generate monochromatic X-rays at high intensities. They are extremely large, expensive and typically found in large research laboratories. Flash x-ray sources are also relatively expensive. They are typically used in high speed imaging applications. They produce a burst of high intensity x-rays (several 1000 amps) over a short period of time, typically a few nano-seconds. They can take several seconds to recharge and have a short tube life. Linear accelerators are used for to generate tube voltages that are larger than 450 kV. They are large, heavy, expensive, and complex and are not suited for drilling applications.

Most medical and industrial applications can be satisfied with tube voltages that are equal to or less than 450 kV. X-ray tubes used in these applications are either intermittent duty or continuous duty. Intermittent duty tubes have to be powered off after regular intervals to avoid damaging the source as opposed to Continuous duty tubes which are designed for continuous (24/7) use. Most intermittent duty tubes find their way into

medical applications which typically require higher output currents and lower voltages compared to industrial applications. It is noted that 99% of the input power to the target material (typically tungsten) for all X-ray tubes is converted to heat with only 1% power contributing towards X-ray production. The heat generated by the high output currents in intermittent duty tubes is dissipated at the anode by using a rotating anode design. These tubes are also characterized by a much shorter lifetime as compared to continuous duty industrial tubes which utilize a stationary anode design. The shorter lifetime can be attributed to wear and tear on the rotating anode bearings or degradation of target and filament because of the high current requirement and heat generation. Furthermore, intermittent duty tubes are typically only rated for indoor use whereas continuous duty tubes are enclosed in a metal ceramic casing and are suitable for outdoor use. Table 7 shows a quick comparison between an intermittent duty tubes used in medical applications and continuous duty X-ray tubes used in industrial applications.

Table 7- Intermittent duty medical grade vs continuous duty industrial grade X-ray tubes.

Source : Varian Medical and Industrial	150 kV Intermittent duty X-ray tube for medical application	225 kV Continuous duty X-ray tube for industrial application
<b>Life</b>	> 800 hrs	> 4000 -8000 hrs
<b>Exposure Time</b>	30 seconds	Continuous Duty (24/7)
<b>Time between Exposure</b>	2 mins	N/A
<b>Cost</b>	~\$8,000	~\$8,000
<b>Environment</b>	Indoor	Outdoor
<b>Power Output</b>	72KW	3KW
<b>Anode Type</b>	Rotating (3000-10000 rpm)	Stationary

The continuous duty X-ray tube is most suitable for the X-ray sensor, since the sensor will be used in an outdoor setting and needs to provide a continuous stream of data. Furthermore, the high X-ray voltage required to penetrate the drilling mud is far greater than that can be provided by a medical grade intermittent duty tube. Other features that need to be considered in selecting an X-ray tube are the size of the focal spot, beam geometry and the choice of tube manufacturer.

The focal spot is the area on the anode which receives the electrons generated by the cathode. The larger the area, the greater the size of the focal spot. Small focal spot result in greater imaging resolution and are typically used in Micro CT applications. Large focal spot sizes on the other hand sacrifice imaging resolution for higher currents and typically provide a longer tube life. In the case of the X-ray sensor imaging resolution is not important and a large focal spot size of 7.3 mm is used.

The beam geometry can be fan-shaped, cone-shaped or toroid shaped. Fan-shaped and cone-shaped beam geometries are most common. Tubes that produce toroid shaped are special purpose and relatively more expensive. They also require expensive deionizing and deoxygenated water coolers. X-ray tubes that produce a fan beam or a cone beam have the exact same mounting locations and only differ in the shape of the X-ray beam that is produced and the beams area of radiation coverage. A fan shaped source has been used on the X-ray sensor with a radiation coverage of  $90^{\circ} \times 30^{\circ}$ .

X-ray tubes up to 225 kV have the same form factor and mounting locations irrespective of their rated voltage and are interchangeable across manufacturers. Most manufacturers produce tubes with similar voltage and power ratings, even though their

prices may vary greatly depending on overall tube quality and adherence to tolerances. Therefore, the reputation of the manufacturer needs to be considered when sourcing an X-ray tube and other X-ray system components to ensure the highest level of quality.

#### **4.4.2 X-RAY GENERATOR, CONTROLLER & COOLER**

The controller is used to regulate the voltage and current supply to the X-ray tube based on user requirements. The controller can be a software based controller that resides on your PC away from the X-ray components or a separate physical unit which is placed or mounted on the X-ray generator. It is recommended that both controllers be sourced with the X-ray sensor to ensure redundancy in the field. A hardware controller for a 3 kW unit starts at about \$4,000 (pricing as per the time this dissertation was written). A software based controller is about \$2,000.

The generator is a high voltage supply which is used to power the X-ray tube. A compatible generator can have a lower power rating than the maximum tube power; however, it needs to have a voltage rating equal to the tube voltage. Thus, a 225 kV 2 kW generator can drive a 225 kV 3 kW tube to a maximum power of 2 kW. However, a 200 kV 3 kW generator would be incompatible with this tube. The cost of the generator along with a PC based controller for a 320 kV 1.5 kW unit starts at approximately \$30,000 (pricing as per the time this dissertation was written). Price varies based on brand name. The high power cables can add another \$2,000 to the assembly. The generator and hardware controller have a mean time between failure (MTBF) of about 5 years. The cost for repair varies with damage incurred. Some companies also offer a generator option whose

components are sealed in an oil bath. These units are typically cheaper and are not recommended as they cannot be serviced in the field and therefore lead to longer repair times. The X-ray tube also requires a cooler to draw the heat away from its body. For a 320 kV 1.5 kW tube a flow of about 4 lpm is recommended. The cost for such a cooler is about \$3,000. The cost of X-ray system components drops with the drop in power and voltage rating of the specified equipment.

The X-ray tube, cooler, and generator/controller are cross compatible between manufacturers. However, they are generally purchased together from a single supplier for ease of system integration. The supplier can be a large OEM or a specialty system integrator. It is recommended that the X-ray components for the X-ray sensor be sourced from a system integrator as they are more cost competitive. Furthermore, unlike the large OEMs they have greater flexibility in assembly of highly customized systems per user specifications. Customization ensures that the equipment is well suited for the application, (i.e. is not over designed) and money is only spent on features that are necessary. Furthermore, the customer can decide how their budget is distributed between different components based on risk tolerance. Calibration of the customized source by the supplier is also highly recommended and can cost anywhere between \$10,000 and \$20,000. This cost can be avoided with in-house calibration knowledge and capabilities.

#### **4.4.3 INTEGRATED BLOCKS**

Integrated blocks are pre-calibrated and mass produced off the shelf X-ray systems. They are compact, lightweight units which have all their electronics and the glass x-ray

tube submerged in an oil bath. The oil is cooled via forced air or circulating the oil via a radiator also built into the unit. They are available in both fan and cone beam options. The control box is not submerged in the oil bath and can be stored separately. The MTBF of the electronics is about 4 years and of the X-ray tube is about 3000 hours. Most integrated blocks come with a 1 year limited warranty. The cost of repair per incident is upwards of 40% of the integrated block price and can vary with the type of repair, i.e., failed electronics, tube replacement or oil leakage. All service is carried out in the shop and can take three weeks provided the tube is available in stock. Even though the upfront cost of sourcing the integrated block may be less as compared to a customized X-ray source, in the long run they prove to more expensive. This is because they are less reliable and have a shorter operating life than customized X-ray sources. The long lead time for repair would require the operator to carry back-up blocks, thus increasing upfront capital investment. Furthermore, the shielding and relevant API certification cost for the entire unit will be more expensive as compared to a customized source which only requires shielding and certification of the X-ray tube.

## **4.5 Conclusion**

The X-ray sensor design shared in this section shows that is quite practical to build a compact X-ray based meter that can be used to make high accuracy density and VFR measurements of drilling fluids in pressurized and non-pressurized lines. The design is compatible with all the density and VFR methods that have been discussed in this dissertation and would allow for easy integration of the sensor into the rig standpipe.

Furthermore, if tracer particles were to be used for VFR measurement, majority of the sensor could be assembled using off-the-shelf components and would require little customization. A prototype sensor has been built and is being used for further validation of the density and VFR measurement methods shared in this dissertation.

## 5 CONCLUSIONS

The primary objective of this dissertation was to develop a sensor that can measure the density and mass flow rate of drilling fluids with greater than 99% accuracy and at a measurement frequency of 1 Hz. These measurements are required in real-time at the well inlet, specifically on the high pressure standpipe.

Based on an extensive literature review of current measurement technologies in Chapter 1, it was determined that achieving the desired performance levels could prove challenging for most of these sensors, in spite of consistent technological advancements. The only real-time sensor that met the 99% accuracy criteria was the gamma ray densitometer. However, it had a radioactive source and was rarely used because of the associated safety concerns.

It was envisioned that X-rays which can be generated without a radioactive source, and work on the same proven principles as gamma rays, could be used to make the density and mass flow rate measurements. It was expected that end users would be more receptive to a sensor technology which is a safer derivative of existing and field established science. The idea to pursue development of an X-ray based sensor was also inspired by the widespread use of X-rays in healthcare industry to make bone density measurements. Furthermore, past patents by Schlumberger and Emerson to develop X-ray based density and GVF meters provided sufficient merit to pursue an X-ray based sensor for measuring the density and mass flow rate of drilling fluids.

## 5.1 Contributions

Each individual chapter in this dissertation made the following contributions to the existing drilling engineering literature:

Chapter 1 provides a concise and up-to-date reference that allows one to narrow down options for a density and flow rate metering solution for oil and gas drilling and completions operations. Due to the vast number of metering options available, it can be daunting and difficult to decide on the right technology that suits both application and cost requirements. Information related to application based meter performance is dispersed across published literature and can be time consuming to collect. Operational specifications listed in product brochures can be misleading as they typically apply to tests done under highly controlled conditions and generally fail to account for the extreme variability in flow conditions in the real world. Due to lack of good reference material, it is not uncommon for oil and gas companies to scramble and waste resources on validation of non-relevant metering solutions. Chapter 1 will serve as a good starting point for anyone tasked with the selection of density and flow measurement solution for a drilling application. It will provide the reader with an overview of the working principles of the mainstream density and flow metering solutions, identify applications they are well suited for and clarify their limitations. The paper covers the major technical aspects associated with meter operation and performance and provides great references for an in-depth investigation into these technical aspects. A comprehensive list of other non-predominant density and flow measurement technologies that could be encountered in the drilling and

completions landscape is also included. A summary table and discussion section provide a criterion for meter selection based on the location where the measurements need to be made. Finally, Chapter 1 helps identify the gaps and shortcomings for the various metering techniques and instruments, which can be used to help guide R&D into density/flow rate measurement improvement.

Chapter 2 describes three different methods which can be used to measure the density of drilling fluids in the high pressure standpipe using X-rays. Work in this chapter demonstrates the feasibility of using X-ray densitometry as a viable substitute to gamma ray densitometry. Not only does this technique provide accuracy levels of greater than 99%, which are typically associated with gamma ray densitometers, but also provides measurements at a 1 Hz measurement frequency, which is 50 times faster than state-of-the-art gamma ray meters. This technique is not limited by the current or future standpipe pressure demands, as these can easily be accommodated for by adjusting the CRP pipe thickness without sacrificing much of the incident X-ray photons. This method also allows to account for changes in drilling fluid temperature, pressure and aeration levels, which can be a challenge for most measurement technologies. The first two methods for density measurement shared in this chapter use the more traditional techniques of X-ray densitometry, i.e. interpolating between pre-measured density values and using the Beer Lambert's law. The third technique however introduces a completely novel way of making density measurements and significantly reduces the number of pre-measured data points that are otherwise required prior to field implementation of the X-ray sensor. It is expected that the on-going work to further develop this method will have implications in other areas

of X-ray based measurements as well. Finally, a simple procedure that can be used to calibrate the X-ray detectors in real-time with greater than 99% reliability is also introduced.

Chapter 3 describes three different methods which could potentially be used to measure the VFR of drilling fluids with an accuracy of 99% or greater. An algorithm which could be used to extract velocity information from high speed images of tracer particles was developed and showed good performance during preliminary tests. Tests also showed that simpler and cheaper alternatives to high speed imaging, such as radiographs of tracer particles captured using an industrial flat panel detector, could also be used to measure VFR. It is hoped that the successful implementation of this technique would provide a new and powerful tool for characterization of fluid flows. Finally, for scenarios where it is not possible to introduce tracers into the fluid stream, a novel method that uses X-rays and a piston mechanism to measure VFR was introduced. Results from simulations showed that a flow resolution of 6.5 gpm could be achieved using this technique when implemented on the 4-inch standpipe.

Chapter 4 is dedicated to the mechanical design of the X-ray sensor. The sensor design benefits from recent advances in pipe manufacturing, particularly a class of low density and high pressure materials known as carbon fiber reinforced polymers (CRPs). The CRP pipe, is the enabling technology that makes it viable to use relatively low cost X-rays systems for density and mass flowrate measurements. In this chapter, suitable types of CRP pipe materials along with the appropriate liner materials which can protect the CRP pipe from the abrasive drilling fluid have been identified. A compact sensor design which

uses the CRP pipe and which can be easily integrated into the high pressure standpipe is then presented. Finally, this chapter also serves as a good reference for anyone tasked with the sizing and selection of appropriate X-ray equipment for a pipe size other than that presented in this dissertation.

## **5.2 Recommendations and Future Work**

In Chapter 2, the density methods have been developed using a 1-inch test pipe and require further validation in a pipe that is 4-inches in diameter. Research is also needed to test the effects of contaminants in model-based method #2, as this method requires the least number of lab measurements prior to field implementation. In Chapter 3, research is needed to validate the block matching algorithm with another flow measurement meter, such as the Coriolis meter, as a reference. Software that uses object tracking techniques (typically available through OpenCV) needs to be written to extract velocity information from radiographs of tracer particles that are obtained using a flat panel detector. Using a flat panel detector is the cheaper and recommended approach for measuring VFR using tracer particles. If tracer particles not a viable option, research efforts can be devoted to further develop the piston mechanism technique. Finally, research is needed in finalizing the design of the lead shielding and obtaining the API certification for the X-ray equipment.

## GLOSSARY

<b>Abbreviations</b>	<b>Meaning</b>
ACM	area used for calibration measurements
ADM	area used for density measurements
ANN	artificial neural network
API	American petroleum institute
AVM	area used for velocity measurements
BBL	barrels
CBHP	constant bottom hole pressure
CCD	charge coupled device
CRP	carbon reinforced polymer
eV	electron volt
GLV	gray level value
GPM	gallons per minute
GVF	gas volume fraction
HGS	high gravity solid
ID	inner diameter
IDM	intelligent drilling motor
KeV	kilo electron volt
KSI	kilo pounds per square inch
KV	kilo volt
LGS	low gravity solid
mA	milli amperes
MAD	median absolute deviation
ME	mean error
MPD	managed pressure drilling
MPFM	multi-phase flow meter
OBM	oil based mud
OD	outer diameter
PPG	pounds per gallon
PSI	pounds per square inch
PVT	pit volume totalizer
RFM	rolling float meter
RPM	revolutions per minute
SBM	synthetic based mud
SD	standard deviation
SG	specific gravity
SNR	signal to noise ratio
SPP	stand pipe pressure
STP	standard temperature and pressure
TTUF	transit time ultrasonic flowmeter

VE	volumetric efficiency
VFD	variable frequency drive
VFR	volumetric flow rate
W	watt
WBM	water based mud
XC	xanthan gum

<b>Symbols</b>	<b>Meaning</b>
$I_0$	X-ray intensity through air
$\bar{Y}$	sample mean
$\mu$	population mean
$\mu_m$	mass attenuation coefficient
A	area
$c_d$	drag coefficient
$E_e$	estimated error
$H_0$	null hypothesis
$H_a$	alternate hypothesis
I	X-ray intensity post-attenuation by medium
k	spring constant
L	stroke length
n	number of samples
P	differential pressure between pump suction and discharge
r	pumping chamber clearance to displacement ratio
S	slip
t	sample depth
$t_e$	estimated depth
v	fluid velocity
$W_p$	weight of piston
x	deflection of piston
$\beta$	liquid's compressibility factor at pumping temperature
$\Delta t$	time interval
$\rho_e$	estimated density
$\rho$	density

## BIBLIOGRAPHY

- Åbro, E., & Johansen, G. A. (1999, April). Void fraction and flow regime determination by low-energy multi-beam gamma-ray densitometry. In Proc. 1st World Congress on Industrial Process Tomography.
- Accardo, A. P., Strolka, I., Toffanin, R., & Vittur, F. (2005). Medical Imaging Systems Technology: Methods in General Anatomy.
- Al-Adwani, T. F., Singh, S. K., Khan, B., Dashti, J. M., Ferroni, G., Martocchia, A., & Estarabadi, J. (2012, January 1). Real time advanced surface flow analysis for detection of open fractures. Society of Petroleum Engineers. doi:10.2118/154927-MS
- Armanini, A., Dalrì, C., Fraccarollo, L., Larcher, M., & Zorzin, E. (2003, September). Experimental analysis of the general features of uniform mud-flow. In 3rd Int. Conf. Debris-Flow Hazard Mitigation (Vol. 1, pp. 423-434).
- Arubi, T. I. M., & Yeung, H. C. (2011, January). Comparative performance assessment study of a high-speed gamma-densitometer in horizontal and vertical multiphase flows. In OTC Brasil. Offshore Technology Conference.
- Ashrafizadeh, H., McDonald, A., & Mertiny, P. (2017). Erosive and Abrasive Wear Resistance of Polyurethane Liners. In Aspects of Polyurethanes. InTech.
- B Blake, G. M., & Fogelman, I. (1993). Recent advances in bone densitometry. *European Journal of Nuclear Medicine and Molecular Imaging*, 20(9), 735-737.
- Babelli, I. M. (1997, December). Development of the multiphase meter using gamma densitometer concept. In Proc. Int. Nucl. Conf (pp. 371-389).
- Baker, R., & Fitzpatrick, J. (1998). Practical well control. Petroleum Extension Service, University of Texas at Austin.
- Barjatya, A. (2004). Block matching algorithms for motion estimation. *IEEE Transactions Evolution Computation*, 8(3), 225-239.
- Barrett, J. F., & Keat, N. (2004). Artifacts in CT: recognition and avoidance. *Radiographics*, 24(6), 1679-1691.
- Blake, G. M., Harrison, E. J., & Adams, J. E. (2004). Dual X-ray absorptiometry: cross-calibration of a new fan-beam system. *Calcified tissue international*, 75(1), 7-14.
- Blake, G. M., McKeeney, D. B., Chhaya, S. C., Ryan, P. J., & Fogelman, I. (1992). Dual energy x-ray absorptiometry: The effects of beam hardening on bone density measurements. *Medical physics*, 19(2), 459-465.

- Brakel, J. D., Tarr, B. A., Cox, W., Jørgensen, F., & Straume, H. V. (2015, March 17). SMART kick detection; First step on the well control automation journey. Society of Petroleum Engineers. doi:10.2118/173052-MS
- Bruton, J., Patel, H. N., Mohammed, S., & Lin, J. (2016, May). Lessons learned during manufacture, installation, deployment and operation of a managed pressure drilling system on classed drilling units in Gulf of Mexico. In Offshore Technology Conference. Offshore Technology Conference.
- Bryant, T. M. (2016, March 1). An instrumented topdrive sub system: Enabling greater drilling efficiencies via innovative sensing capabilities. In IADC/SPE Drilling Conference and Exhibition. Society of Petroleum Engineers. doi:10.2118/178864-MS
- Burris, D. L., & Sawyer, W. G. (2006). A low friction and ultra low wear rate PEEK/PTFE composite. *Wear*, 261(3-4), 410-418.
- Caldwell, R., & Scott, T. J. (2010, January 1). Plug indicator system prevents calculated volume errors during subsea casing primary cementing operations. Society of Petroleum Engineers. doi:10.2118/133687-MS
- Cayeux, E., Daireaux, B., Dvergsnes, E. W., & Florence, F. (2013, March 5). Toward drilling automation: On the necessity of using sensors that relate to physical models. Society of Petroleum Engineers. doi:10.2118/163440-MS
- Chen, Y., Huang, Y., & Chen, X. (2013). Acoustic propagation in viscous fluid with uniform flow and a novel design methodology for ultrasonic flow meter. *Ultrasonics*, 53(2), 595-606.
- Chopty, J., & Sardo, A. (2011, January 1). Managed pressure drilling as a tool to reduce risks and non-productive time: An update on field experience. Offshore Mediterranean Conference.
- Cockburn, A. (1987). The driller's problems with gas solution in oil based muds. Conference and Exhibition, Dallas, SPE
- Corser, G. P., Harmse, J. E., Corser, B. A., Weiss, M. W., & Whitflow, G. L. (2000, January 1). Field test results for a real-time intelligent drilling monitor. Society of Petroleum Engineers. doi:10.2118/59227-MS
- Daireaux, B., & Cayeux, E. (2013, October 7). Precise gain and loss detection using a transient hydraulic model of the return flow to the pit. Society of Petroleum Engineers. doi:10.2118/166801-MS
- Darley, H. C., & Gray, G. R. (1988). Composition and properties of drilling and completion fluids. Gulf Professional Publishing.
- Driedger, D. J., Kelly, S. P., Leggett, C., Thain, J., & Silva, M. (2013, March 10). Managed pressure drilling technique applied in a Kurdistan exploration well. In SPE Middle

- East Oil and Gas Show and Conference. Society of Petroleum Engineers. doi:10.2118/164403-MS
- Eren, H. (1998, May). Accuracy in real time ultrasonic applications and transit-time flow meters. In *Instrumentation and Measurement Technology Conference, 1998. IMTC/98. Conference Proceedings. IEEE (Vol. 1, pp. 568-572). IEEE.*
- Faulkner, K. G., & McClung, M. R. (1995). Quality control of DXA instruments in multicenter trials. *Osteoporosis international, 5(4), 218-227.*
- Fraser, D., Lindley, R., Moore, D. D., & Vander Staak, M. (2014, October 27). Early kick detection methods and technologies. In *SPE Annual Technical Conference and Exhibition. Society of Petroleum Engineers. doi:10.2118/170756-MS*
- Friedrich, K., Lu, Z., & Hager, A. M. (1995). Recent advances in polymer composites' tribology. *Wear, 190(2), 139-144*
- Geothermal Today, 1999 Geothermal energy program highlights, US Department of Energy.
- Gregory, D., West, M., Paton, R., Casimiro, R., Boo, S., Low, Y. K., & Zamora, M. E. (2008). Two-phase flow metering using a large Coriolis mass flow meter applied to ship fuel bunkering. *Measurement and Control, 41(7), 208-212.*
- Guest, R. J., & Zimmerman, C. W. (1973). Compensated gamma ray densimeter measures slurry densities in flow. *Pet. Eng.:(United States),45(10).*
- Han, J., Liu, H., Zhou, Y., Zhang, R., & Li, C. (2014, April). Studies on the transducers of clamp-on transit-time ultrasonic flow meter. In *Information Science and Technology (ICIST), 2014 4th IEEE International Conference on (pp. 180-183). IEEE.*
- Hannegan, D., & Mahmood, A. (2015, May 4). Offshore well integrity management with MPD tools and technology. *Offshore Technology Conference. doi:10.4043/25723-MS*
- Haugh, M. J., Charest, M. R., Ross, P. W., Lee, J. J., Schneider, M. B., Palmer, N. E., & Teruya, A. T. (2012). Calibration of X-ray imaging devices for accurate intensity measurement. *Powder Diffraction, 27(2), 79-86.*
- Hauptmann, P., Hoppe, N., & Püttmer, A. (2002). Application of ultrasonic sensors in the process industry. *Measurement Science and Technology,13(8), R73.*
- Heindel, T. J., Gray, J. N., & Jensen, T. C. (2008). An X-ray system for visualizing fluid flows. *Flow Measurement and Instrumentation, 19(2), 67-78.*
- Heismann, B. J., Leppert, J., & Stierstorfer, K. (2003). Density and atomic number measurements with spectral X-ray attenuation method. *Journal of applied physics, 94(3), 2073-2079.*

- Henry, M., Duta, M., Tombs, M. J., Yeung, H., & Mattar, W. (2004). How a Coriolis mass flow meter can operate in two-phase (gas/liquid) flow. ISA, Houston, TX.
- Henry, M., Tombs, M., Duta, M., Zhou, F., Mercado, R., Kenyery, F., & Langansan, R. (2006). Two-phase flow metering of heavy oil using a Coriolis mass flow meter: A case study. *Flow Measurement and Instrumentation*, 17(6), 399-413.
- Henry, M., Yeung, H., & Mattar, W. (2005). The two phases of Coriolis flow. *InTech*, 52(1), 32-34.
- Hoag, M. L., & Krahmer, R. L. (2007). Polychromatic X-ray attenuation characteristics and wood densitometry applications. *Wood and fiber science*, 23(1), 23-31.
- Hocke, H., & Wilkinson, H. N. (1978). Testing abrasion resistance of slurry pipeline materials. *TRIBOLOGY international*, 11(5), 289-294.
- Hoeppner, C., Liptak, B., & Livingston, A. (2003). 6.6 Radiation Densitometers.
- Horner, B. (1998). A novel profile-insensitive multi-electrode induction flowmeter suitable for industrial use. *Measurement*, 24(3), 131-137.
- Hossain, M. E., & Al-Majed, A. A. (2015). *Fundamentals of sustainable drilling engineering*. John Wiley & Sons.
- Hsieh, J., Molthen, R. C., Dawson, C. A., & Johnson, R. H. (2000). An iterative approach to the beam hardening correction in cone beam CT. *Medical physics*, 27(1), 23-29.
- Im, K. S., Fezzaa, K., Wang, Y. J., Liu, X., Wang, J., & Lai, M. C. (2007). Particle tracking velocimetry using fast x-ray phase-contrast imaging. *Applied physics letters*, 90(9), 091919.
- Iwai, Y., & Nambu, K. (1997). Slurry wear properties of pump lining materials. *Wear*, 210(1-2), 211-219.
- Ji, S., Sun, C., Zhao, J., & Liang, F. (2015). Comparison and analysis on mechanical property and machinability about polyetheretherketone and carbon-fibers reinforced polyetheretherketone. *Materials*, 8(7), 4118-4130.A
- Joe Evans. Positive displacement pumps Part I – Reciprocating Pumps. <http://www.pumped101.com>
- Johnson, A., Leuchtenberg, C., Petrie, S., & Cunningham, D. (2014, March 4). Advancing deepwater kick detection. Society of Petroleum Engineers. doi:10.2118/167990-MS
- Kelkar, S., Boushey, C. J., & Okos, M. (2015). A method to determine the density of foods using X-ray imaging. *Journal of food engineering*, 159, 36-41.
- Kell, G. S., & Whalley, E. (1965). The PVT properties of water. *Phil. Trans. R. Soc. Lond. A*, 258(1094), 565-614.

- Kertzscher, U., Seeger, A., Affeld, K., Goubergrits, L., & Wellnhofer, E. (2004). X-ray based particle tracking velocimetry—a measurement technique for multi-phase flows and flows without optical access. *Flow Measurement and Instrumentation*, 15(4), 199-206.
- Khabaz, R., & Yaghobi, F. (2015). Design and employment of a non-intrusive  $\gamma$ -ray densitometer for salt solutions. *Radiation Physics and Chemistry*, 108, 18-23.
- Khlifa, I., Coutier-Delgosha, O., Fuzier, S., Vabre, A., & Fezzaa, K. (2013). Velocity measurement in cavitating flows using fast X-ray imaging. In *Congrès Français de Mécanique (21; 2013; Bordeaux)*.
- Khorsandi, M., & Fegghi, S. A. H. (2011). Design and construction of a prototype gamma-ray densitometer for petroleum products monitoring applications. *Measurement*, 44(9), 1512-1515.
- Khorsandi, M., Fegghi, S. A. H., Salehizadeh, A., & Roshani, G. H. (2013). Developing a gamma ray fluid densitometer in petroleum products monitoring applications using Artificial Neural Network. *Radiation Measurements*, 59, 183-187.
- Kotzé, R., Ricci, S., Birkhofer, B., & Wiklund, J. (2015). Performance tests of a new non-invasive sensor unit and ultrasound electronics. *Flow Measurement and Instrumentation*.
- Kumara, W. A. S., Halvorsen, B. M., & Melaaen, M. C. (2010). Single-beam gamma densitometry measurements of oil–water flow in horizontal and slightly inclined pipes. *International Journal of Multiphase Flow*, 36(6), 467-480.
- Lassahn, G. D., Stephens, A. G., Taylor, D. J., & Wood, D. B. (1979). X-ray and gamma ray transmission densitometry. *Int. Coll. on Two Phase Flow Instr., Idaho*.
- Lee, S. J., & Kim, G. B. (2003). X-ray particle image velocimetry for measuring quantitative flow information inside opaque objects. *Journal of Applied Physics*, 94(5), 3620-3623.
- Leeungculsatien, T., & Lucas, G. P. (2013). Measurement of velocity profiles in multiphase flow using a multi-electrode electromagnetic flow meter. *Flow Measurement and Instrumentation*, 31, 86-95.
- Lehman, A., O'Rourke, N., Hatcher, L., & Stepanski, E. (2013). *JMP for basic univariate and multivariate statistics: Methods for researchers and social scientists*. Sas Institute.
- Leys, C., Ley, C., Klein, O., Bernard, P., & Licata, L. (2013). Detecting outliers: Do not use standard deviation around the mean, use absolute deviation around the median. *Journal of Experimental Social Psychology*, 49(4), 764-766.
- Li, L., Li, R., Zhang, S., Zhao, T., & Chen, Z. (2016). A dynamic material discrimination algorithm for dual MV energy X-ray digital radiography. *Applied Radiation and Isotopes*, 114, 188-195.

- Limkitjaroenporn, P., Kaewkhao, J., Chewpraditkul, W., & Limsuwan, P. (2012). Mass attenuation coefficient and effective atomic number of Ag/Cu/Zn alloy at different photon energy by Compton scattering technique. *Procedia Engineering*, 32, 847-854.
- Liu, R. P., Fuent, M. J., Henry, M. P., & Duta, M. D. (2001). A neural network to correct mass flow errors caused by two-phase flow in a digital Coriolis mass flowmeter. *Flow Measurement and Instrumentation*, 12(1), 53-63.
- Luca, A., Marchiano, R., & Chassaing, J. C. (2016). Numerical simulation of transit-time ultrasonic flowmeters by a direct approach. *IEEE transactions on ultrasonics, ferroelectrics, and frequency control*, 63(6), 886-897.
- Mahadeva, D. V., Baker, R. C., & Woodhouse, J. (2009). Further studies of the accuracy of clamp-on transit-time ultrasonic flowmeters for liquids. *Instrumentation and Measurement, IEEE Transactions on*, 58(5), 1602-1609.
- Mahieux, C. A. (2001). Cost effective manufacturing process of thermoplastic matrix composites for the traditional industry: the example of a carbon-fiber reinforced thermoplastic flywheel. *Composite structures*, 52(3-4), 517-521.
- Malloy, K. P., Stone, R., Medley, G. H., Hannegan, D. M., Coker, O. D., Reitsma, D., ... Sonnemann, P. (2009, January 1). Managed-pressure drilling: What it is and what it is not. Society of Petroleum Engineers. doi:10.2118/122281-MS
- Mammadov, E., Kinik, K., Ameen Rostami, S., & Sephton, S. (2015, April 27). Case study of managed pressure tripping operation through abnormal formations in west Canadian sedimentary basin. Society of Petroleum Engineers. doi:10.2118/174073-MS
- Mansure, A. J., Whitlow, G. L., Corser, G. P., Harmse, J., & Wallace, R. D. (1999, January 1). A probabilistic reasoning tool for circulation monitoring based on flow measurements. Society of Petroleum Engineers. doi:10.2118/56634-MS
- Meibohm, J., Schreck, S., & Wernet, P. (2014). Temperature dependent soft X-ray absorption spectroscopy of liquids. *Review of Scientific Instruments*, 85(10), 103102.
- Mishima, K., Hibiki, T., & Nishihara, H. (1997). Visualization and measurement of two-phase flow by using neutron radiography. *Nuclear Engineering and design*, 175(1), 25-35.
- Mitchell, R. F., & Miska, S. Z. (2017). *Fundamentals of drilling engineering*. Society of Petroleum Engineers.
- Morgan, T. B., Halls, B. R., Meyer, T. R., & Heindel, T. J. (2013, July). A high-speed X-ray detector system for noninvasive fluid flow measurements. In *ASME 2013 Fluids Engineering Division Summer Meeting* (pp. V01CT24A004-V01CT24A004). American Society of Mechanical Engineers.

- Nelson, G., & Reilly, D. (1991). Gamma-ray interactions with matter. *Passive Nondestructive Analysis of Nuclear Materials*, 27-42.
- Nickles, S. K. (1972, January 1). An instrument for measuring the density of air entrained fluids. In *Fall Meeting of the Society of Petroleum Engineers of AIME*. Society of Petroleum Engineers. doi:10.2118/4092-MS
- O'Banion, T. (2013). Coriolis: the direct approach to mass flow measurement. *Chemical Engineering Progress*, 109(3), 41-46.
- Park, H. S., & Chung, C. H. (2007). Design and application of a single-beam gamma densitometer for void fraction measurement in a small diameter stainless steel pipe in a critical flow condition. *Nuclear Engineering and Technology*, 39(4), 349-358.
- Peters, E. J., Chenevert, M. E., & Zhang, C. (1990). A model for predicting the density of oil-base muds at high pressures and temperatures. *SPE drilling engineering*, 5(02), 141-148.
- Pham, D. C., Sridhar, N., Qian, X., Sobey, A. J., Achintha, M., & Shenoi, A. (2016). A review on design, manufacture and mechanics of composite risers. *Ocean Engineering*, 112, 82-96.
- Piccolo, B., & Leuchtenberg, C. (2015, April 13). Physical concept validation testing performed for a pore and fracture pressure margin prediction system during offshore MPD operations. In *SPE/IADC Managed Pressure Drilling and Underbalanced Operations Conference & Exhibition*. Society of Petroleum Engineers. doi:10.2118/173809-MS
- Prettyman, Johnny B. (2014), Comparison of selected differential producing, ultrasonic, and magnetic flow meters" (2014). Unpublished master's thesis, Utah State University, Logan, Utah.
- Prettyman, R., Wiklund, J., & Haldenwang, R. (2013). Optimisation of pulsed ultrasonic velocimetry system and transducer technology for industrial applications. *Ultrasonics*, 53(2), 459-469.
- Pushnov, A. V. (2013). Measurement of the flow rate of a two-phase flow by a Coriolis flowmeter. *Measurement Techniques*, 56(4), 421-425.
- Read, H. S. (1926). Some effects of temperature on X-ray absorption. *Physical Review*, 28(5), 898.
- Reitsma, D. (2010, January 1). A simplified and highly effective method to identify influx and losses during Managed Pressure Drilling without the use of a Coriolis flow meter. Society of Petroleum Engineers. doi:10.2118/130312-MS
- Reizner, J. R. (2004). Coriolis mass flow meters in batching applications—the good, the bad and the ugly. *ISA Expo*.

- Reizner, J. R. (2004). Exposing Coriolis mass flowmeters' "dirty little secret". *Chemical Engineering Progress*, 100(3), 24-30.
- Ritchie, G. M., Hutin, R., Aldred, W. D., & Luppens, J. (2008, January 1). Development and testing of a rig-based quick event detection system to mitigate drilling risks. *Society of Petroleum Engineers*. doi:10.2118/111757-MS
- Roels, S., & Carmeliet, J. (2006). Analysis of moisture flow in porous materials using microfocus X-ray radiography. *International Journal of Heat and Mass Transfer*, 49(25-26), 4762-4772
- Roshani, G. H., Fegghi, S. A. H., Shama, F., Salehizadeh, A., & Nazemi, E. (2014). Prediction of materials density according to number of scattered gamma photons using optimum artificial neural network. *Journal of Computational Methods in Physics*, 2014.
- Russo, P., & Del Guerra, A. (2014). Solid-state detectors for small-animal imaging. in *molecular imaging of small animals* (pp. 23-82). Springer New York.
- Salmon, P. L., & Liu, X. (2014). MicroCT bone densitometry: context sensitivity, beam hardening correction and the effect of surrounding media. *The Open Access Journal of Science and Technology*, 2.
- Sanderson, M. L., & Yeung, H. (2002). Guidelines for the use of ultrasonic non-invasive metering techniques. *Flow measurement and Instrumentation*, 13(4), 125-142.
- Santhosh, K. V., & Roy, B. K. (2012). An intelligent flow measurement technique using ultrasonic flow meter with optimized neural network. *International Journal of Control and Automation*, 5(4), 185-195.
- Santiago, J. G., Wereley, S. T., Meinhart, C. D., Beebe, D. J., & Adrian, R. J. (1998). A particle image velocimetry system for microfluidics. *Experiments in fluids*, 25(4), 316-319.
- Sare, I. R., Mardel, J. I., & Hill, A. J. (2001). Wear-resistant metallic and elastomeric materials in the mining and mineral processing industries—an overview. *Wear*, 250(1-12), 1-10.
- Schafer, D. M., Loeppke, G. E., Glowka, D. A., Scott, D. D., & Wright, E. K. (1992, January 1). An Evaluation of flowmeters for the detection of kicks and lost circulation during drilling. *Society of Petroleum Engineers*. doi:10.2118/23935-MS
- Seeger, M. (2005). Coriolis flow measurement in two phase flow. *Computing & Control Engineering Journal*, 16(3), 10-16.
- Singer, G., Wyckoff, H. O., & DAY, F. (1947). Relative Thickness of Lead, Concrete, and Steel Required for Protection Against Narrow Beams of X-Rays. *Journal of research of the National Bureau of Standards*, 38(6), 665-672.

- Singhal, V., Ashok P., van Oort, E. (2018, April). Advanced X-ray technology for real-time high pressure mass flow rate measurement. In AADE National Technical Conference and Exhibition, Houston, AADE
- Singhal, V., Ashok, P., Oort, E. V., & Park, P. (2018, September). A Novel X-Ray Based High Pressure Mass Flow Rate Sensor for MPD Operations. In SPE Annual Technical Conference and Exhibition. Society of Petroleum Engineers.
- Soutis, C. (2005). Carbon fiber reinforced plastics in aircraft construction. *Materials Science and Engineering: A*, 412(1-2), 171-176.
- Speers, J. M., & Gehrig, G. F. (1987, December 1). Delta flow: An accurate, reliable system for detecting kicks and loss of circulation during drilling. Society of Petroleum Engineers. doi:10.2118/13496-PA.
- Staller, G. E., Westmoreland, J. J., Whitlow, G. L., Wright, E. K., & Glowka, D. A. (1998). Final report on the design and development of a rolling float meter for drilling-fluid outflow measurement (No. SAND--98-0481). Sandia National Labs., Albuquerque, NM (United States)
- Stephenson, K. E., & Becker, A. J. (1997). U.S. Patent No. 5,689,540. Washington, DC: U.S. Patent and Trademark Office.
- Svete, A., Kutin, J., Bobovnik, G., & Bajsić, I. (2015). Theoretical and experimental investigations of flow pulsation effects in Coriolis mass flowmeters. *Journal of Sound and Vibration*, 352, 30-45.
- Tackett, H. H., Cripe, J. A., & Dyson, G. (2008). Positive displacement reciprocating pump fundamentals-power and direct acting types. In Proceedings of the twenty-fourth international pump user symposium (pp. 45-58).
- Thiago, P. da S., Hollman, L., Puerto, G., & Brand, P. (2016, March 1). Bridging the gap between MPD and well control. Society of Petroleum Engineers. doi:10.2118/178810-MS
- Tjugum, S. A., Frieling, J., & Johansen, G. A. (2002). A compact low energy multibeam gamma-ray densitometer for pipe-flow measurements. *Nuclear Instruments and Methods in Physics Research Section B: Beam Interactions with Materials and Atoms*, 197(3), 301-309.
- Torres, F. R., Silva, A., & Caetano, E. F. (2005, May 25). Petrobras experience on offshore multiphase pumping. BHR Group
- Vieira, P., Arnone, M. A., Torres, F., & Barragan, F. (2009, January 1). Roles of managed pressure drilling technique in kick detection and wellcontrol—The beginning of the new conventional drilling way. In Middle East Drilling Technology Conference & Exhibition. Society of Petroleum Engineers. doi:10.2118/124664-MS
- Voss, H., & Friedrich, K. (1987). On the wear behaviour of short-fibre-reinforced PEEK composites. *Wear*, 116(1), 1-18.

- Vural, Ş. Z., Bayram, G., & Uludag, Y. (2014). Experimental investigation of drag reduction effects of polymer additives on turbulent pipe flow using ultrasound Doppler velocimetry. *Turkish Journal of Chemistry*, 38(1), 142-151.
- Wagner, R. R., Halal, A. S., & Goodman, M. A. (1993, January 1). Surge field tests highlight dynamic fluid response. In *SPE/IADC Drilling Conference*. Society of Petroleum Engineers. doi:10.2118/25771-MS
- Wang, C., Shankar, K., & Morozov, E. V. (2015). Tailored local design of deep sea FRP composite risers. *Advanced Composite Materials*, 24(4), 375-397.
- Wang, J. Z., Tian, G. Y., & Lucas, G. P. (2007). Relationship between velocity profile and distribution of induced potential for an electromagnetic flow meter. *Flow Measurement and Instrumentation*, 18(2), 99-105.
- Wang, L. J., Liu, J. Y., Yan, Y., Wang, X., & Wang, T. (2016). Gas-liquid two-phase flow measurement using Coriolis flowmeters incorporating neural networks.
- Wang, T., & Baker, R. (2014). Coriolis flowmeters: a review of developments over the past 20 years, and an assessment of the state of the art and likely future directions. *Flow Measurement and Instrumentation*, 40, 99-123.
- Wang, Y., Liu, X., Im, K. S., Lee, W. K., Wang, J., Fezzaa, K., ... & Winkelman, J. R. (2008). Ultrafast X-ray study of dense-liquid-jet flow dynamics using structure-tracking velocimetry. *Nature Physics*, 4(4), 305.
- Whitehouse, R. W., & Adams, J. E. (1992). Single energy quantitative computed tomography: the effects of phantom calibration material and kVp on QCT bone densitometry. *The British journal of radiology*, 65(778), 931-934.
- Whitlow, G. L., Glowka, D. A., & Staller, G. E. (1996). Development and use of rolling float meters and Doppler flow meters to monitor inflow and outflow while drilling geothermal wells (No. CONF-960913--). Geothermal Resources Council, Davis, CA (United States).
- Wiklund, J., Kotzé, R., Birkhofer, B., Ricci, S., Meacci, V., Haldenwang, R., & Stading, M. (2014, August). Flow-Viz™—A fully integrated and commercial in-line fluid characterization system for industrial applications. In *Proceedings of the 9th International Symposium on Ultrasonic Doppler Methods for Fluid Mechanics and Fluid Engineering*.
- Windhorst, T., & Blount, G. (1997). Carbon-carbon composites: a summary of recent developments and applications. *Materials & Design*, 18(1), 11-15.
- Xie, Y., Jiang, J. J., Tufa, K. Y., & Yick, S. (2015). Wear resistance of materials used for slurry transport. *Wear*, 332, 1104-1110.
- Xu, L. J., Li, X. M., Dong, F., Wang, Y., & Xu, L. A. (2001). Optimum estimation of the mean flow velocity for the multi-electrode inductance flowmeter. *Measurement Science and Technology*, 12(8), 1139.

- Zhang, S. W. (1998). State-of-the-art of polymer tribology. *Tribology International*, 31(1-3), 49-60.
- Zoellner, P., Thonhauser, G., Lueftenegger, M., & Spoerker, H. F. (2011, January 1). Automated real-time drilling hydraulics monitoring. *Society of Petroleum Engineers*. doi:10.2118/140298-MS